Advanced Catalyst Design and Reactor Configuration Upgrade in Electrochemical Carbon Dioxide Conversion

Zhitong Wang [†a, b], *Yansong Zhou* [†a], *Peng Qiu* [†c], *Chenfeng Xia* [a], *Wensheng Fang* [a], *Jian Jin* [c], *Lei Huang* [a], *Ya Qiong Su* [d], *Rachel Crespo-Otero* [e], *Xinlong Tian* [b], *Bo You* [a], *Wei Guo* [a] *, *Di Tommaso Devis* [e] *, *Yuanjie Pang* [c] *, *Shujiang Ding* [d] *, and *Bao Yu Xia* [a] *

[a] Key Laboratory of Material Chemistry for Energy Conversion and Storage (Ministry of Education), Hubei Key Laboratory of Material Chemistry and Service Failure, State Key Laboratory of Materials Processing and Die & Mould Technology, School of Chemistry and Chemical Engineering, Huazhong University of Science and Technology (HUST), 1037 Luoyu Rd, Wuhan 430074, China

Email: Wguo@hust.edu.cn (W. Guo); byxia@hust.edu.cn (B. Y. Xia)

[b] State Key Laboratory of Marine Resource Utilization in South China Sea, Hainan Provincial Key Lab of Fine Chemistry, School of Chemical Engineering and Technology, Hainan University, Haikou 570228, China

[c] School of Optical and Electronic Information, Wuhan National Laboratory for Optoelectronics, Huazhong University of Science and Technology (HUST), 1037 Luoyu Road, Wuhan 430074, China

Email: yuanjie_pang@hust.edu.cn (Y. Pang)

[d] School of Chemistry, Xi'an Jiaotong University, 28 Xianning West Rd, Xi'an 710049, China

Email: dingsj@mail.xjtu.edu.cn (S. Ding)

[e] School of Physical and Chemical Sciences, Queen Mary University of London, Mile End Road, London E1 4NS, United Kingdom

Email: d.ditommaso@qmul.ac.uk

[†] These authors contributed equally.

Abstract: Electrochemical carbon dioxide reduction reaction (CO_2RR) driven by renewable energy shows great promise in mitigating and potentially reversing the devastating effects of anthropogenic climate change and environmental degradation. The simultaneous synthesis of energy-dense chemicals can meet global energy demand while decoupling emissions from economic growth. However, the development of CO_2RR technology faces challenges in catalyst discovery and device optimization that hinder their industrial implementation. In this contribution, we provide a comprehensive overview of the current state of CO_2RR research, starting with the background and motivation for this technology, followed by the fundamentals and evaluated metrics. We then discuss the underlying design principles of electrocatalysts, emphasizing their structure–performance correlations and advanced electrochemical assembly cells that can increase CO_2RR selectivity and throughput. Finally, we look to the future and identify opportunities for innovation in mechanism discovery, material screening strategies, and device assemblies to move toward a carbon-neutral society.

Keywords: Carbon dioxide reduction; Electrocatalyst; Electrolyzer design; Cell configuration.

1. Introduction

The industrial revolution and technological progress have brought about significant benefits for human society, improving living welfare and increasing economic growth. However, this development has come at a cost to the global environment, as the consumption of petrochemical sources continue to rise. This has led to a significant increase in atmospheric CO_2 concentration, rising from approximately 280 ppm in the early 1800s to 410 ppm in 2015.[1] Excessive anthropogenic CO_2 emissions resulting from human activities pose serious threats to the global biomes, including climate change, environmental deterioration, and inevitable depletion of nonrenewable fossil fuel resources.[2] To address this issue, the Paris Agreement established a global consensus to mitigate the harmful effects of emission from economic growth, potentially reverse their adverse consequences. Proposed solutions include the introduction of renewable energy transportation and utilization sectors, as well as the implementation of decarbonized programs with high energy efficiency.[3] However, although ambitious blueprint has been announced for a promising zero-carbon network, the penetration of renewables into industrial facilities and the integration of carbon capture, utilization, and storage (CCUS) technologies continue to face severe challenges.

Over the past few decades, capturing CO_2 from ambient air has already been practiced as a pretreatment step for commercial cryogenic air separation, which is envisioned as the ideal upstream unit in CCUS projects.[4, 5] Downstream product sequestration from CO_2 utilization can be managed through mature separation technologies in modern industrial manufacturing to recover commodity feedstocks.[6] However, compared to the well-established upstream and downstream processes of CCUS, advanced methodologies for carbon utilization are still in an underexplored stage.[7] Potential candidates in this research grid, compatible with renewable energy input, can be categorized into four main aspects: photochemistry, biochemistry, thermochemistry, and electrochemistry.[8-14] Photochemical conversion of CO_2 mimics the natural photosynthetic system but suffers from intermittent harvesting of solar energy. Biochemical approaches are

seriously constrained by rate limitations. Thermochemically hydrogenated CO_2 fed by molecular hydrogen is an extensively studied topic, but the hydrogen sources in most CO_2 hydrogenation schemes are compressed and commonly come from steam reforming of methane, resulting in significant energy loss. However, particularly as renewable electricity has become available and affordable, the electrocatalytic CO_2 reduction reaction (CO_2RR) using earth-abundant water as a hydrogen donor has become an attractive method for neutralizing carbon emissions.[15-18] Additionally, CO_2 electrolysis for chemical manufacturing is also appealing for coping with the energy crisis in a fully sustainable manner. In this way, the global carbon cycle could be artificially closed by decoupling emissions from economic growth, and the value-added products from electrochemical CO_2 valorization simultaneously make this technology profitable (**Scheme 1**).

It is generally accepted that CO_2 molecules are chemically inert, which makes electrochemical CO_2RR a challenging and thermodynamically uphill process. Appropriate electrocatalysts are therefore prerequisite to overcome the CO_2 activation barrier.[19] Electrocatalysts also play a decisive role in determining the product distribution through subsequent multiple proton-coupled electron transfer (PCET) reactions.[20] According to the number of electrons consumed, CO_2RR can yield a broad spectrum of products, including carbon monoxide (CO), formic acid (HCOOH), methane (CH_4), ethylene (C_2H_4), ethanol (C_2H_5OH) and other multicarbon hydrocarbons and oxygenates.[21-25] Notably, the preferred product may vary significantly depending on the electrocatalysts employed and electrocatalytic conditions performed, which poses knotty challenges for selective generation of target chemicals. The competitive hydrogen evolution reaction (HER), with theoretically zero thermodynamics, also competes with CO_2RR in aqueous media.[26-28] Therefore, rational electrocatalyst design is critical for achieving high-efficiency, stable, and economically feasibility of CO_2RR. Another crucial component of the CO_2RR is the electrochemical device, which integrates electrodes, membranes, electrolytes, and operating environments.[29-31] Electrolyzers for CO_2RR determine the processing capacity and energy efficiency of this technology. Through optimizing device engineering, desired

performance metrics can be realized, enabling high-throughput CO_2 electrolysis for practical implementation.[32, 33] While laboratory-scale research has showcased impressive outcomes using gas diffusion electrodes (GDEs) and membrane electrode assemblies (MEAs), there is still a lack of maturity in producing high-purity and high-concentration chemicals from CO_2RR for industrialization.[34] In brief, advanced electrocatalyst design and electrolyzer engineering are important to enable the lab-to-fab journey of electrocatalytic CO_2RR technology.

In recent years, significant progress has been made in the field of CO_2RR, with exponentially increasing research efforts. However, many studies have focused only on specific aspects of this technology. An integrated approach covering scientific fundamentals, materials design, and device engineering is essential to expedite the foreseeable commercialization of CO_2RR technology.[34-42] In this contribution, we provide a thoroughly overview of significant developments in fundamental science, material chemistry, and electrolyzer engineering for electrocatalytic CO_2 refinery (**Scheme 2**). We begin by discussing a brief background and significance of the CO_2RR, followed by detailed introduction of fundamental concepts, including the reaction mechanism and evaluation metrics. We then delve into the principles for rational electrocatalyst design, with an in-depth understanding of their structure-performance correlation. We also explore the different types of electrocatalytic reactors and assembled components that have been developed to improve the throughput of the CO_2RR. Finally, we highlight the remaining challenges and emerging perspectives that must be addressed to enable practical applications of CO_2RR technology for a carbon-neutral and sustainable human society.

2. Fundamentals in CO_2RR

The design of efficient electrocatalysts critically depends on a comprehensive and detailed understanding of the fundamentals of the CO_2RR. Over the past few years, theoretical predictions, experimental validations, and technoeconomic analyses have extensively contributed to this field. In this section, we will briefly describe CO_2RR mechanism and list several critical descriptors for performance evaluation. We also discuss a rigorous

assessment of the corresponding targets required for practical feasibility.

2.1. Reaction mechanism roadmap

Electrocatalytic CO_2 reduction is a complex process involving multielectron transfer and different adsorption patterns of surface-bonded species (**Scheme 3**). Beginning with the adsorption and subsequent activation of CO_2 reactants on the catalyst surface, the key $*CO_2^{\bullet-}$ (* infers the adsorption site) radicals are formed as the prerequisite of all CO_2RR pathways.[43, 44] Then, depending on the nature of catalysts, electrolytes, and applied potentials, numerous possible intermediates could be involved. Depending on their adsorption configurations and binding strengths, the resulting products vary significantly from single-carbon (C_1) chemicals to multi-carbon (C_{2+}) hydrocarbons and oxygenates.[45, 46] For the major C_1 products concerned in CO_2RR-related research, HCOOH and CO can be generated via different adsorption configurations of $*CO_2^{\bullet-}$ and reaction intermediates.[47, 48] The carboxyl intermediate (*COOH), formed with the O atom coordinated to the catalyst surface, tends to promote the production of CO, whereas the formate intermediate (*OCHO), with the C atom coordinated to the catalyst surface, predominantly yields formic acid. Generally, formic acid generation through *OCHO is suggested as an isolated branch from hydrocarbon pathways in the CO_2RR roadmap, and the presented form of the final product is dependent on a critical electrolyte pH value of 3.75. Notably, *CO derived from *COOH is an important crossroad in the CO_2RR, which can be either desorbed or further reduced. For example, from carbon-pronated *CHO, other C_1 molecules will form, including methanol (CH_3OH), formaldehyde (HCHO), and CH_4, depending on the number of PCET processes involved.[49-51] Pathways leading to the formation of energy-dense C_{2+} products are appealing but considerably more challenging as they require the formation of C-C bonds.[52, 53] Several mechanisms regarding the C-C coupling reaction have been proposed to date corresponding to various multicarbon products. The most accepted direct *CO dimerization diagram proceeds through stepwise hydrogenation processes of the *CO dimer to form $*OCH–CH_2$, which plays a selectivity-determining role for C_2H_4 and C_2H_5OH.[54, 55] In addition,

hydrogen-assisted C-C coupling is recognized as the insertion of pristine *CO into carbon-protonated *CHO, through which trace amounts of glyoxal ($C_2H_2O_2$) and glycol ($C_2H_6O_2$) can be obtained.[56, 57] The "carbene mechanism" is another possible route toward C_2 products, stemming from the oxygen-protonated *COH and subsequent hydrogenation, leading to $*CH_2$, a key intermediate.[58, 59] Potentially, the $*CH_2$ monomer can go through a direct dimerization reaction to generate C_2H_4, be further reduced ($*CH_3$) and then dimerized to C_2H_6, or inserted by *CO, which is responsible for the formation of acetate (CH_3COOH).[60, 61] Based on these considerations, the formation of C_3 products such as *n*-propanol (C_3H_7OH) can also be rationalized by the coupling between C_2 and C_1 intermediates, which simultaneously entails catalysts with high coverage and robust binding affinity with C_2 species.[62, 63] Unfortunately, major uncertainties remain in the C_3 reaction mechanism, as the coexistence of several competitive intermediates and interlaced reaction pathways may participate. While the interaction between catalysts and reaction intermediates is manifestly directing the CO_2RR roadmap, precisely tailoring the absorbents is tricky due to the linear-scaling relationship, which suggests that the adsorption energies of these species are highly convoluted.[64] In addition to the various carbonaceous intermediates that have been extensively unveiled, the crucial role of protons is generally ignored.[65] Properly manipulated proton flux is essential for CO_2RR; otherwise, it will adversely trigger the parasitic HER, lowering the selectivity toward desired products.

2.2. Catalytic performance evaluation

To assess the electrocatalytic performance of a CO2RR catalyst, various figures of merit are employed. While the Faraday efficiency (FE) is commonly used to report the selectivity towards a specific product, caution must be exercised when comparing experimental values from different studies due to potential limitations associated with this descriptor.[66] First, the evaluation of FE needs to be more rigorous.[66] As the products quantified by both gas chromatography and nuclear magnetism spectrometry are in the unit of concentration, the volumetric flow rate should be multiplied to assess the selectivity. A prevalent rule-of-

thumb is using the inlet flow rate as a surrogate of the outlet flow rate, which simplifies the investigation but brings nonnegligible inaccuracies.[67, 68] On the one hand, the entered CO_2 feed will be substantially consumed by electrocatalytic reactions, especially under ampere-level industrial operating conditions. On the other hand, a significant portion of the CO_2 reactant will be depleted in the form of bicarbonate/carbonate due to the interaction with the alkaline electrolyte.[69] Such an approximation can lead to considerable overestimation of the calculated FE values, and severe energy costs are posed in CO_2 recycling. Therefore, the single-pass conversion efficiency (SPCE) is emerging as a nascent benchmark describing the amount of carbon that ends up as CO_2RR products versus the total carbon that enters into the electrocatalytic system, which is momentous for bypassing the obscure in fundamental evaluation and improving the economic efficiency of CO_2RR.[70, 71] The second issue in reporting FE is that a higher selectivity corresponding to a specific product may not always guarantee a higher rate of product generation. Furthermore, to fully characterize the electrocatalytic activity of the material, it is important to report the current density, particularly for the desired products. Moreover, normalizing the current density by the electrochemically active surface area (ECSA) of the catalyst can provide an effective parameter for measuring the intrinsic activity, or alternatively, be used to calculate the per-active-site turnover frequency (TOF) for the same purpose.[72] Importantly, the current density is influenced by several variables, including the configuration of the electrocatalytic cell, the properties of the current collector, the loading and deposition technique of the catalyst, and the flow rate of both the CO2 feed and electrolyte. Characterizing the stability of CO2RR is particularly challenging due to its susceptibility to multiple sources of degradation, such as issues with reactor configuration, membrane integrity, electrolyte composition, and irreversible catalyst deactivation. During stability testing, the intrinsic activity of the catalyst may be obscured, and the dominant effect of mass transfer should be considered. In summary, these experimental details should be considered to ensure reproducibility, facilitate meaningful performance comparisons across studies, and ensure reproducibility. Furthermore, establishing standardized data

acquisition and description protocols can help promote consistency and transparency in the field.

3. Catalyst design for CO_2RR

Developing efficient electrocatalysts is always a prerequisite for pursuing highly active, selective and durable CO_2RR. Ever since Teeter and Van Rysselbergh proposed electrochemical CO_2 reduction in their pioneering study back in 1950, the field has grown exponentially, with significant research efforts dedicated to both heterogeneous and homogeneous approaches.[74] Tamaru et al. introduced molecular electrocatalysts (metal complexes) for CO_2RR in 1974, which typically involve homogeneous catalysis based on modular assembly principles.[75] Electrocatalysts based on metal–organic complexes offer well-defined active sites to bind with reactants and intermediates, as well as precise tailorability to address the corresponding structure-performance relationships. However, molecular catalysts are notorious for their complex synthetic protocols, which potentially involve toxic reagents, and poor structural stability regarding aggregation, leaching and demetallation, especially under high-rate electrolysis.[76] The employment of heterogeneous metal-based electrocatalysts in the CO_2RR has been demonstrated by Hori's group, who found that the product distribution is strongly determined by the nature of the catalysts.[77-80] The main advantages of heterogeneous electrocatalysts are the facile preparation and, more importantly, universal compatibility with various modification strategies to manipulate their electrocatalytic performance.[81-87] Electrocatalyst design efforts to improve performance are discussed in the next section, mainly emphasizing aspects of heterogeneous electrocatalysis based on structure control, oxidation state regulation, defect engineering, interface interaction, and surface modification.[88-92] These factors are unlikely to be mutually exclusive but function in synergy to boost significant improvements, which makes it difficult to distinguish the strategies clearly. In particular, most advanced design strategies for optimizing catalytic performance follow the same principle and focus on modulating the binding strength between the catalyst and intermediate. In this section, we aim to provide a comprehensive overview of the latest advances in catalyst design, focusing on the underlying mechanisms

that drive their enhanced performance. Based on the different strategies for regulating intermediates, we have divided the discussion on advanced catalyst design into four areas: (1) electronic structure, (2) adsorption configuration, (3) intermediate concentration, and (4) indirect mediating effects.. The discussion of recent progress will not discriminate and enumerate different design strategies as presented in most review work but will focus on the fundamental principle of intermediate regulation to reveal their structure-performance correlation to specific products.

3.1. Electronic structure

The electronic structure of catalytic materials plays a decisive role in the adsorption strength of key intermediates during CO_2 electroreduction. Especially for metal-based catalysts, the d-band center theory can reveal the interaction between the electronic structure of metal active sites and the adsorption of intermediates.[93-95] Generally, the bonding strength of intermediates increases with the upper shift of the d-band energy level. Optimizing the adsorption of intermediates by adjusting the electronic structure to improve catalytic performance is the basic principle commonly used in current well-known design strategies. This chapter will take the space dimension as the guide, starting from the single-atom catalysts (SAC), gradually increasing the catalyst size to nanoparticles, then the crystal plane and the final interface, to outline how various design strategies steer the electronic structure of catalytic sites to deliver excellent catalytic activity.

SAC is the ultimate dispersion of metal-based catalysts, which is constructed by isolated active centers coordinated on various conductive substrates to maximize the utilization efficiency of metal loading. The unique assembly configuration of SAC combines the merits of homogeneous and heterogeneous catalysis, with well-defined active sites and precise electronic controllability, which provides a unique platform for the delving into catalytic mechanisms and has recently become densely populated in CO_2RR and beyond.[48, 96-98] For SAC, the holistic electronic structure rests with the atomically dispersed metal sites and the adjacent coordination environment, which plays a momentous role in the definition of catalytic activity, product

selectivity and stability.[99] Previous studies have revealed three types of SAC according to distinct resulting products caused by the diverse electronic structure of the metal center, namely, Ag, Au, and transition metals Fe, Co, and Ni for generating CO, In, Bi, and Sn for producing HCOOH, while Cu primarily yields hydrocarbons.[100-102] It can be seen that these SACs share a similar CO_2RR direction but higher activity than their corresponding bulk metal due to the peculiar electronic configuration within the M-N_4 moieties, where the metal center atom is saturated with four coordinated N atoms.

Regulation of the coordinative electronic structure herein takes the extensively studied Ni SAC as an example. Although massive research efforts and desirable CO_2RR performance have been obtained on saturated Ni-N_4 moieties, rational management over the coordination microenvironment remains a focused topic.[103-105] For example, Jiang et al. reported the controlled fabrication of Ni-N_x via postionic substitution, where the coordination number could be tuned by the pyrolysis temperature to accurately dominate defect formation (i.e., 800 ℃ for Ni-N_4 and 900 ℃ for Ni-N_3-V, respectively) **(Figure 1a)**. The low-coordinate Ni-N_3-V delivers an outperformed CO_2RR performance compared to the Ni-N_4 catalyst, which is ascribed to the minimized energy barrier toward the COOH* intermediate (Figure 1b). The presence of N vacancies in Ni-N_3-V is essential to promote the desorption of *CO, as the Ni-N_4 counterpart exhibits a hindered free energy profile to release CO.[106]

Vacancy defects in the coordination unsaturated Ni-N_3-V moiety deliver atomic local space, which is propitious for heteroatom doping to further optimize the electron distribution. Yang et al. accurately controlled the P heteroatom to replace the N atom in the Ni-N_4 monomer to prepare Ni-N_3P configuration SACs for effectively electrocatalytic reduction of CO_2 toward CO.[107] The electrons donated by atom P will be localized around the Ni metal sites and spontaneously transferred to the C 2*p* orbit of CO_2, which strikingly alleviates the high energy barrier of *COOH, showing a catalytic performance far superior to that of Ni-N_4 (Figure 1c).

When the heteroatom is a metal element other than O, S, N, C, or P, it is inclined to form a secondary

metal single site at the original adjacent position of M-N_4, which constitutes a diatomic site catalyst (DASC).[108, 109] For example, in the process of preparing Ni-SAC, NiFe-N_6 DACS could be obtained by using iron metal salt as an additional additive, in which Ni-N_4 and Fe-N_4 share two N atoms to form a 2 N-bridged configuration (Figure 1d). The hybrid coupling of atomic orbitals between Ni atoms and Fe atoms redefines the electron density distribution of NiFe-N_6, enhances the adsorption of *COOH and promotes the desorption of *CO, which finally determine the CO_2RR activity and CO selectivity far exceeding those of both Ni-N_4 and Fe-N_4 SACs (Figure 1e).[110] The regulation of the metal center and coordination environment in SAC is by no means limited to the above strategies and coordination configurations, but it follows the same principle as the exemplified methods, that is, improving the interaction between electronic structures and optimizing intermediates to achieve better catalytic performance.

Without ligating coordination atoms, the metal centers of single atom sites squint toward agglomeration to form nanoparticles (NPs) impelled by high surface free energy. Generally, the electrocatalytic performance of nanoparticles principally governed by the grain size effect comes down to variations in the density of undercoordinated sites caused by surface-to-bulk atom ratio alternation, in which the binding affinity with key intermediates is partially reinforced at unsaturated sites with unique electronic structures.[111-113] Research efforts on the size modulation of particulate catalysts and the underlying correlation with CO_2RR performance have been proven on a variety of metal-based materials. Gu et al. developed a series of Ni-based catalysts from SAC scale to NPs over 100 nm in diameter.[114] Notably, the selectivity toward CO is significantly decreased upon enlarged grain size, with 97% for Ni SAC and 29% corresponding to oversized NPs (**Figure 2a-b**). Theoretical investigation verified that smaller catalysts possessed more available catalytic sites for CO_2 conversion and a minimized energy barrier to form *COOH (Figure 2c-d). In fact, smaller particles are not always promised in catalyst optimization. Li's group has reported that smaller-sized In_2O_3 nanocrystals endowed an enhanced intermediate binding ability for both CO_2RR and HER due to high atomic coordination

deficiency, which is indispensable to achieve a trade-off between uncoordinated active sites and competitive side reaction for the superlative catalytic manifestation (Figure 2e).[115]

For NPs, the introduction of heteroatoms can also endow the catalysts with an appropriate intermediate binding energy by virtue of electronic coupling with the host site, demonstrating a satisfactory CO_2RR capability.[116, 117] With the increase in guest components, alloys will be gained in the form of solid solutions among metals, in which the catalytic performances due to the properties of foreign metals are also subject to the mastery of atomic arrangement and orientation among alloys.[118, 119] Intermetallic alloys manifest ordered structures and fixed stoichiometries with well-defined crystallographic arrangements, and extraordinary geometric-electronic interactions are desirable catalysts for CO_2 electroreduction, as reflected by the optimized intermediate binding configuration in the CO_2RR. An extensively studied candidate in this scenario is Pd, which can catalyze CO_2 reduction to formate near the equilibrium potential but is inferiorly subjected to *CO poisoning from the side reaction intermediate.[120] One recent study reported the phase transformation of PdBi nanocrystals from intermetallic compounds to randomly arranged solid-solution alloys by thermal annealing, where the former delivered persistent ~100% formate selectivity, while the latter was subjected to a limited value of below 60% with poor anti-poisoning capability **(Figure 3a)**.[121] Their distinct CO_2RR performance resulted from different crystallographic structures with featured electronic states. Alloying Bi with Pd with intermetallic assembly could appropriately deactivate the Pd surface, thus preventing the overbinding of *H and *CO, and the formation of the formate intermediate also turned from endothermic to exothermic.

In the process of spontaneous growth, in view of formation energy diversity, nanocrystals can develop polyhedral shapes composed of crystal planes. The crystal planes with different indexes and arrangements possess different catalysis properties due to the distinction in the arrangement of atoms, ions, and molecules, which is a manifestation of crystal anisotropy.[122-124] Fundamental research has predicted that crystalline faces

play a pivotal role in the deep reduction of CO_2. These hypotheses were systematically elucidated by single-crystal studies as a simplified picture, and the well-defined Cu (100) single-crystal surface showed higher C_{2+} selectivity than its (111) and (110) counterparts due to the preferred *CO dimerization pathway (Figure 3b).[125] Gong et al. developed a dynamic deposition-etch-bombardment method to prepare Cu (100)-rich films. During bombard-induced recrystallization, the loosely arranged (100) facet could be stabilized to substitute for the densely packed (111) surface. The as-synthesized catalyst manifested a maximum FE of 86.6% for C_{2+} products and could be upscaled in a 25 cm^2 MEA system to record a high current of 12 A.[126]

In regard to shaped NPs with diversified exposed surfaces, the circumstances would be more complicated, and a cooperative mechanism between these catalytic regions may exist. For example, truncated-octahedral Cu_2O enclosed by both (100) and (111) planes showed a higher C_2H_4 productivity, and the discrepant Fermi level between the two facets would promote such multielectron-involved kinetics and C-C coupling processes (Figure 3c).[127] In addition, Gao et al. prepared a series of oxide-derived Cu (OD-Cu) materials composing different types of exposed crystal planes, and the Cu (100)/(111) interface was identified as more catalytically active than the individual counterpart. DFT analysis unveiled that the Cu atoms sandwiched by the two facets contained different structural arrangements, inducing local distortion and electronic state regulation, and considerably optimized the dimerization energetics (Figure 3d-f).[128] As a result, an impressive multicarbon FE of 75% at an industrially relevant current density of 300 mA cm^{-2} was obtained on the hybrid Cu catalysts.

The research consensus that the boundary between two or more crystal planes in polyhedral NPs has better catalytic activity can also be derived from interface engineering, which is mainly decided by the interface environment (heterointerface or modification interface) composed of host materials and foreign materials or organic additives. The metal-oxide interface has been generally considered an efficient catalytic site in CO_2 hydrogenation and CO oxidation reactions, which encompass oxygen-containing carbonaceous intermediates similar to those in the CO_2RR.[129, 130] Among many kinds of oxide candidates, ceria (CeO_2) has emerged as

an ideal option to activate CO_2 reactants and has been extensively investigated. For instance, Bao's group demonstrated that the Au−CeO_x interface improved the adsorption and activation of CO_2, and water dissociation also occurred herein, which generated hydroxyl groups and promoted the conversion of Ce^{4+} to Ce^{3+}, which is vital to *COOH stabilization.[130] Another relative contribution recently focused on the Au species in the Au−CeO_2 hybrid. Upon reductive electrochemical pretreatment, the reduction of Au^{3+} species could deliver excessive electrons to partially reduce the CeO_2 support, generating abundant $Au^{\partial+}$ sites and oxygen vacancies at the interface **(Figure 4a)**.[131] These features coincidently promoted CO_2 activation and *COOH formation, ensuring a high CO FE of 95% from −0.7 to −1.0 V vs. RHE. Constructing a metal-oxide interface that is catalytically active for the CO_2RR is an intriguing way to duplicate active centers and boost the electrochemical performance. Inspired by the "ship in a bottle" concept in catalyst design, Chen and coworkers fabricated ultrafine twinned ZnO/Ag nanoparticles encapsulated in carbon nanospheres (Figure 4b).[132] The formulated Zn-O-Ag interface induced collective electron migration from Zn and Ag to O, which helps to stabilize the *COOH intermediate and imposes a high energy barrier for the competing hydrogen evolution and *HCOO formation reactions, allowing a high selectivity of 94.1% toward CO. In addition, the excellent structural stability inhibited the agglomeration and detachment of nanoparticles confronting the harsh cathodic CO_2RR potentials, thus withstanding a long-term operation of 150 h with an intact original phase. It should be noted that lattice strain caused by lattice mismatch among different components at the heterointerface will also affect the d-band electronic structure of the material, reflecting diametrically different catalytic properties. For example, the overlayer thickness in the Cu/SnO_2 core-shell catalyst induced a lattice compression effect and determined the electrocatalytic CO_2RR performance.[133] There was a 10% compressive strain observed on the 0.8 nm SnO_2 shell-wrapped Cu catalyst, which could preferentially reduce CO_2 to CO with an FE of 93% at -0.7 V vs. RHE. In contrast, the loosely interacting hybrid dominantly yielded formate.

The functionalized interface obtained by modifying the material surface with organic additives also renders the ability to regulate the electronic structure.[134, 135] For instance, Liu and coworkers proposed a post-hydrothermal treatment to prepare an aminated Ni-N_4-C-NH_2 catalyst, which concurrently ensures grafted functional groups and highly exposed catalytic sites. In addition to the enhanced CO_2 adsorption capacity, electronic charge redistribution also intensified the binding energy of *COOH species, resulting in a high partial conversion rate of 440 mA cm^{-2} and selectivity of 90% for CO (Figure 4c).[136] In addition, cyano organic species decorated Ni SAC readily alleviates the d-π conjugation within Ni monatomic sites and C_3N_4 supports, and the metal Ni active centers with localized electrons can efficaciously fulfil the rapid activation and conversion of CO_2 toward CO (Figure 4d).[137]

The above discussion highlights the significant impact of optimizing the electronic structure on the CO_2RR, from single atom site to catalytic interface. However, under certain bias operating conditions, the electronic structure of metal-based materials, especially high-performance catalysts containing oxidation states, can deteriorate rapidly due to the reduction of the oxidation state, leading to significant performance degradation.[138-142] Therefore, while designing and steering the electronic structure of materials using various strategies, it is compulsory to consider the real-time evolution of active sites in the in situ reaction process and adopt oxidation state protection strategies to prevent the catalyst from undergoing reconstruction failure.

3.2. Adsorption configuration

Customizing the adsorption configuration of key intermediates on active sites represents a key aspect in the design of CO_2RR electrocatalysts. The adsorption configuration determines the affinity strength between intermediates and catalytic centers, which mainly depends on the local atomic environment, i.e., the composition and number of coordinated elements, affecting the orientation of reaction paths and the distribution of reduction products.[143-145] Furthermore, the adsorption configuration can splendidly enable the selective synthesis of multicarbon products such as ethanol or ethylene by regulating the high coordination

environment and space symmetry to surmount the high energy barrier required in C-C couplingThis section categorizes adsorption modes into single-site, multi-site, interface, and surface auxiliary configurations based on the action modes between key intermediates and adsorption sites. Furthermore, we provide a detailed explanation of how the adsorption configuration can enhance the catalytic performance of CO_2RR.

The single-site configuration is defined as the reaction intermediate species interacting and bonding only with a solitary active center, which is the most common adsorption configuration in the reaction pathway orientation. It is well known that the intermediate *COOH or *OCHO produced by CO_2 through the first PCET step is the initial point of many product branches, which is essentially controlled by the affinity between the active center and the C/O element in the intermediate.[146-148] Broadly speaking, when the binding priority of the active metal center to the C atom is prior to the O atom, a *COOH intermediate will be formed by M-C bond coordination, which is successively prone to be protonated to CO or other deep-reduction hydrocarbon products in the subsequent process.[149] Instead, the *OCHO intermediate stabilized by the M-O bond is the optimal approach of the thermodynamic dynamic process on the HCOOH reduction pathway. Admittedly, the selective preparation of reduction products can be steered by carefully tailoring the intermediate adsorption configuration of either *COOH or *OCHO, as demonstrated by prior pioneering work. Bao et al. successfully implemented the potential-dependent surface hydrogen species adsorption strategy to achieve highly efficient catalytic reduction of CO_2 over Pd nanoparticles, resulting in the formation of formate and CO with near-unity selectivity.[150] With the bias voltage gradually shifting from -0.2 V to -0.5 V vs. RHE, the hydrogen adsorption species on the surface of Pd NPs decayed from full coverage to low coverage, accompanied by the evolution of the active phase from PdH_X to metallic Pd, on which the corresponding preferential adsorption intermediates were *OCHO and *COOH, respectively **(Figure 5a)**. Overall, for Pd NPs, the FEs of formate and CO can reach 98% and 93% at -0.1 V vs. RHE and -0.7 V vs. RHE due to the voltage-orientated intermediate adsorption configuration, and the current density can achieve industrial level with the integration

of compact electrolyzers.

Despite the kinetic favorability of the *COOH-mediated *CO pathway, an alternative pathway that involves proton hydrogenation instead of dehydration can potentially generate HCOOH. In the case of Bi nanocrystals, the reduction of CO2 to formate through the *COOH pathway is accompanied by a rapid attenuation of the formate FE due to the negative potential enhancement, which is essentially hindered by the outgrowth of CO. Doping with Cu atoms improves the formate selectivity of Bi nanocrystals by promoting the adsorption configuration of Bi nanocrystals from *COOH to *OCHO, effectively suppressing the production of CO and hydrogen and delivering a satisfying catalytic performance toward formate (Figure 5b).[151]

The multisite configuration can be deconvoluted into two kinds in conformity with the types and numbers of coordination atoms, namely, single atom-multisite and multiatom-multisite. Single atom-multisite can also be termed bridge absorption, which is different from the atop absorption in a single-site configuration, in which atoms can form coordination bonds with multiple sites.[152, 153] Single atom-multisite regulation seizes a dominant region in the directional formation of eager products, especially for C_2H_5OH and C_2H_4, among which the atop absorption and bridge absorption of *CO intermediate trigger distinction in protonation activation energy barrier and coupling coordination saturation, breaking the FEs of ethylene far exceeding that of ethanol in C_{2+} product distribution over Cu-based materials.[143] Qiao et al. bore out that the subsequent protonation of *CO is more favorable on bridge adsorption *CO sites than on top adsorption sites, engendering the medley adsorption pattern of *CHO and *CO over the Cu catalyst surface, which triggers asymmetric C-C dimerization with an admissible energy barrier relative to nomothetic C-C coupling within a pair of *CO.[154] Furthermore, the asymmetric coupling between *CO and *CHO disrupted the highly coordinated environment required to stabilize *CCH, a key intermediate of the ethylene pathway. As a result, this favoured the generation, leading to a significant FE of 40.8% at a partial current density of 326.4 mA cm^{-2} (Figure 5c).

Rather than focusing on the selectivity of ethanol by constructing a single atom-multisite configuration that stabilizes the *CO intermediate, an alternative strategy involves disrupting the bridge adsorption configuration of specific intermediates following C-C coupling. This strategy can enhance the FE of C_2H_5OH. Through an in-depth understanding of reaction intermediates, the C_2H_5OH and C_2H_4 pathways are highly entangled and result in *HCCOH formation, from which the reaction branches out to *HCCHOH and *CCH via protonation and dehydration, respectively, until the final products.[155, 156] The intermediate *CCH of C_2H_4 is more unsaturated with respect to *HCCHOH for ethanol, which prefers to be stabilized by the coordination of C atoms with the surrounding three Cu atoms to form a bridge multisite adsorption configuration accompanied by a higher bonding strength with C atoms.[157, 158] Conversely, considerable reaction intermediates involved in the C_2H_5OH pathway are apt to combine with Cu atoms in a vertical manner through a single-site configuration, and the discrepancies between the C_2H_4 and C_2H_5OH pathways in coordination sites and saturation render a theoretical instruction and direction for the intended regulation of C_2H_5OH selectivity. Recently, Li and coworkers investigated a CuAg alloy catalyst based on DFT predictions and demonstrated excellent catalytic performance in ethanol production.[159] Their calculations indicate that the *CCH intermediate of the ethylene pathway is more susceptible to the introduction of Ag atoms than the *HCCHOH intermediate of the ethanol pathway. Therefore, the introduction of Ag atoms with weaker C binding capacity will destroy the high coordination environment required by the ethylene reaction pathway, realizing the enhancement of ethanol selectivity through the regulation of binding sites (Figure 5d-f). In situ surface-enhanced Raman spectroscopy also further confirmed the diversity of binding sites and configurations caused by the CuAg alloy. Electrochemical testing using a flow cell as an electrolytic reactor showed the FE of ethanol reaching 41% at a high current density of 250 mA cm^{-2}, far exceeding the 29% ethanol FE of the pure Cu comparative sample.

Interfacial configuration is widely embraced in heterostructure hybrid catalysts containing multifunctional

active sites, which have a strong affinity interaction with the oxygen-containing carbonaceous intermediate in the CO_2RR, forming an interface adsorption configuration involving multivariate components and additionally anchoring the stability of the intermediate.[160-162] Sinton et al. performed DFT calculations on the established Cu-SiO_x step surface, which suggests that the key ethylene intermediates *OCOH and *OCCOH could be stabilized at the interface via strong Si–O or Si–C bonds (Figure 5g).[163] Further increasing the SiO_2 content to 4.7% would passivate the interface due to the fully paired electrons in the Si–O–Si layer. In light of the theoretical guidance, an optimal SiO_2 loading of 2.5% in the Cu-SiO_x composite guaranteed a high C_2H_4 selectivity of 65% at 300 mA cm^{-2} in an MEA electrolyzer. Luo et al. synthesized a series of $In(OH)_3$-coupled Cu_2O hybrid catalysts with alterable In content and reduced $In(OH)_3/Cu_2O$ to a metallic state through a pretreatment process to study the promotion effect of the Cu-In metal interface on the CO_2 electroreduction process.[164] The strong binding affinity of In atoms to O atoms will change the adsorption configuration of *COOH on the Cu-In interface, in which the mutual anchoring of Cu-O bonds and In-O bonds inhibits the high formation free energy of *COOH, thereby underpinning CO production with a high selectivity of 90.4% at -0.8 V vs. RHE (Figure 5h).

The surface modification strategy, which represents one of the most common approaches in electrocatalytic design for CO_2RR, plays a critical role in altering the adsorption configuration and free energy of intermediates through a synergistic interplay between the surface microenvironment and active sites, relying on coordination and bonding.[165-167] Surface auxiliary configurations are primarily determined by the selection of surface modifiers, with hydroxyl and amino functional groups currently being the dominant choices, owing to their ability to participate in hydrogen bonding interactions.[168, 169] By employing a combination of in situ detection and DFT calculations, recent research has revealed that hydroxyl species on SnO play a crucial role in directing CO2 reduction towards formate production, as demonstrated by a marked increase in formate Faradaic efficiencies following hydroxyl modification.[170] The OH^--mediated surface auxiliary configuration

can be explained by the hydrogen bond formed between the H atom of the hydroxyl group and the O atom of the oxygen-containing carbonaceous intermediate, over which the *OCHO free energy is preferable to that of the OH^-excluded surface, which accelerates the directional and high-rate electroreduction toward formate.

3.3. Intermediate concentration

The intermediate concentration can be optimized to prevent any adverse impact on the fluctuation of the intermediate adsorption strength by tuning the electronic structure or adsorption configuration, as explained in the preceding chapters. Specifically, the focus is on manipulating the spatial distribution of specific intermediates within the local reaction environment, to enhance the catalytic activity and achieve the desired outcome. The concentration distribution of critical intermediates is closely associated with the catalytic activity of CO_2RR. This can be broadly interpreted as a positive correlation between the concentration of intermediates and reaction efficiency, without necessarily considering the finite number of catalytic active sites.[171-173] Through a systematic exploration of the reaction mechanism, it has been discovered that there is a regulatory mode for intermediate concentration that triggers C-C coupling in the C_{2+} pathway. Specifically, high *CO coverage has been found to be conducive in reducing the free energy barrier associated with dimerization.[174-178] The remainder of this section will describe in detail the catalyst design strategy that focuses on the concentration of intermediates, which includes the spillover, confinement, and enrichment of intermediates. The discussion will be organized according to the order of atomic-scale spillover, nanoscale confinement, interfacial-scale concentration, and micrometer/centimeter scale material spatial distribution. Additionally, the tandem reaction and electrochemical carbon monoxide reduction reaction (CORR) based on the analogous design understructure will be briefly introduced.

Atomic-scale spillover refers to the delivery of intermediates amidst distinct active sites. For Cu-based materials with unparalleled competence to spark C-C coupling for C_{2+} manufacture, the introduction of active centers with specific *CO selectivity in the spatial proximity position near Cu atoms can quickly convert CO_2

to produce enough *CO intermediates and then overflow to Cu sites, resulting in a drastic augmentation in the selectivity of multi-carbon products.[179] For instance, Grätzel and coworkers improved the activity and selectivity of CO_2 reduction to ethylene through the atomic-scale *CO spillover effect brought by the introduction of Ag atoms (**Figure 6a**).[180] They first prepared Cu_2O nanowires with highly dispersed Ag NPs by the galvanic replacement reaction and then obtained the metallic Cu-Ag composite catalyst through the prereduction process. Operando Raman spectroscopy indicates that the Cu-Ag bimetallic catalyst provides more *CO binding sites during the CO_2 reduction process, increases the local *CO concentration on the electrode surface, and successfully promotes the hydrogenation of *CO to the important intermediates of C_2 products such as *CHO and *C_2H_2O. The increase in the coverage of *CO on the Cu-Ag surface is attributable to 95% of the CO generated on the Ag sites overflowing to the nearby Cu sites. In general, the Cu-Ag catalyst exhibited significantly enhanced catalytic activity and selectivity for C_{2+} products, which was attributed to the effective CO overflow effect. The FE of C_{2+} reached 76%, and the selectivity of ethylene accounted for 68.4% of the C_2 product distribution.

The migration characteristics of *CO evoke an extremely low local concentration in the catalyst with an open space structure, which worsens the probability of collision and triggering within *CO intermediates and depresses the selectivity of C_2 products. In addition to the integration of difunctional site nanomaterials consisting of efficient CO-yielding catalysts with hydrocarbon-selective Cu, the construction of nanoconfined reactors also designates a unique cascade pathway for the CO_2RR.[171, 181] Zeng et al. synthesized hollow Cu nanospheres with controllable shell structures, which were used as a desirable platform model to expound the mutuality mechanism among space confinement, *CO intermediate concentration, and C_{2+} product selectivity.[182] Finite element simulations were used to probe the diffusion dynamics of *CO in confined Cu shells. It was found that as the hollow Cu nanospheres evolved from 1-shell to 3-shell, the *CO intermediates in nanocavities were enriched, which was due primarily to the outflux resistance and prolonged diffusion path

for *CO (Figure 6b-f). The inspissated *CO in 3-shell Cu nanospheres was experimentally corroborated by in situ Raman spectra, which boosted the odds of coupling into C_{2+} products, manifesting a maximum C_{2+} FE of 77.0% at a partial current density of 513.7 mA cm^{-2}, far exceeding the 40.3% C_{2+} FE of 1-shell Cu nanospheres with a 268.8 mA cm^{-2} partial current density. The confinement effect can also be utilized to enhance the Faradaic Efficiency (FE) for propanol in the CORR. Zhuang et al. conducted the efficient and selective synthesis of propanol products in Cu nanocavities by CORR with an FE content of approximately 21% and a current density of 7.8 mA cm^{-2} under -0.56 V vs. RHE, whereby the nanocavity formed by in situ electrochemical reduction availably elongated the retention time of C_2 species and showed congruous adaptability to directional C_3 production (Figure 6g).[183]

Steering the local reaction environment of the electrocatalytic interface to strengthen the availability of reactants and intermediates by surface functionalization is an efficacious route to reinforce the CO_2RR.[184] Inspired by the Lewis acid-base interaction and well-established amine-based absorbents for CO_2 capture, amino group-functionalized electrocatalysts are compelling to facilitate CO_2 adsorption and activation.[169, 185, 186] An early study also pointed out that amino-containing glycine would stabilize the key *CHO intermediate on Cu electrodes toward hydrocarbon formation.[187] Zhuang et al. reported that the modification of polyaniline (PANI) on a Cu surface could enrich the local CO_2 concentration at the Cu/PANI interface and enhance surface hydrophobicity to suppress the HER.[188] A consequent improved *CO intermediate coverage adsorbed on the Cu surface then promoted the C-C coupling process, allowing for a high C_{2+} selectivity of 80% at -1.08 V vs. RHE (**Figure 7a**).

Enrichment of reactants is also feasible by modifying the catalyst surface with mass-diffusion channels.[179] Leveraging the advantages in high porosity and adsorption capacity of porous organic cages (POCs), it is anticipated to surmount the mass transport limitation due to the poor CO_2 solubility and the competing HER caused by the hydrophilic catalyst surface by employing POCs as modifiers. As validated, by facilely mixing

the Cu nanocatalyst with POCs as the hybrid catalyst layer, an impressive C_{2+} yield of 76.1% with a current density of 1.7 A cm^{-2} was showcased. In contrast, the bare Cu nanocatalyst counterpart delivered a corresponding FE of 64.5% and conversion rate below 300 mA cm^{-2}, which could be rationalized by the insufficient local *CO intermediate and CO_2 reactant accessibility according to molecular dynamics simulation (Figure 7b-c).[189]

CORR can productively obtain the C_{2+} product via the CO route, which avoids the unfavorable path of *CO desorption in CO_2RR to produce the C_1 product and further enhances the selectivity and current density of C_{2+} by regulating the partial pressure of injected CO.[190, 191] With this inspiration, a cascade system integrating two continuous electrolysis steps of CO_2-to-CO and CO-to-C_{2+} is proposed to brace an effective indirect path for CO_2-to-C_{2+}. Tang's group quadrated Ni SAC and hollow Cu_2O as two distinct catalysts for CO_2 to CO and CO to n-propanol, respectively, whereby the inlet of the CO_2-to-n-propanol system was undertaken by the Ni active site by efficiently converting CO_2 into CO, and activation dimerization was executed on the Cu atom, which gave an unparalleled selectivity of 15.9% for *n*-propanol (Figure 7d).[192] However, the dispute still indwells in the dialectical view of in situ spillover *CO intermediate and CO inlet feed gas to ameliorate the C-C coupling function. A recent research contribution has revealed that the generation rate of multicarbon alcohols through *CO spillover means was increased by an order of magnitude compared to that of CO direct reduction. This finding establishes the cornerstone for subsequent regulation of spatial distribution on the micrometer/centimeter scale. For example, Wu and collaborator reported a stacked gas diffusion electrode design with reference to a plug-flow reactor that cements the conversion by prolonging the retention time of reactants, in which a CO-selective catalytic layer is superimposed on a C_{2+}-selective catalytic layer, and in situ generated *CO diffuses along the direction perpendicular to the electrode.[193] The intensive *CO coverage and partial pressure along the through-plane direction delivered positive feedback to the increase in C_{2+} current density, steering a conversion upgrade by approximately 1.2 times relative to the

pristine Cu counterpart. Ultimately, a segment tandem gas diffusion electrode according to the gas channel of the electrolytic device is proposed to fortify the *CO spatial distribution in the length direction of the in-plane electrode, in which the CO-selective catalytic layer is located at the top of the gas diffusion electrode corresponding to the CO_2 inlet of the device, and the rest of the gas diffusion electrode is the C_{2+}-selective catalytic layer (Figure 7e-f). Compared with stacked gas diffusion electrolysis, the *CO management of segmented tandem gas diffusion electrodes in the electrode length direction is superior to that in the plane direction, and the CO conversion segment adapted to the CO_2 inlet can reinforce the *CO partial pressure and residence time to the greatest extent, shepherding the selectivity of C_{2+} products up to 90% and the current density overtakes 1 A cm^{-2}.

3.4. Indirect mediating effect

The abovementioned regulation strategies of carbonaceous intermediates undoubtedly fall within direct medium, including the optimization of electronic structure and adsorption configuration to realize the management of adsorption affinity, as well as tailoring activation energy barrier by intensive intermediates. The intermediates and products involved in CO_2RR can be indirectly influenced by adjusting the distribution and intensity of the interface electric field, which has a reciprocal effect on the dipole moment of carbonaceous intermediates. This modification leads to a change in the intermediates and products produced.[194] Furthermore, the significance of proton *H as an essential component for carbonaceous intermediates to complete PCET, which is critical for activating and converting intermediates, is often overlooked. This section will show how this chapter will show how the indirect mediating effects of intermediate regulation, including the interface electric field and water management, can optimize and enhance of the CO_2RR process.

Referring to the interfacial electric field, the cation effect is an indispensable part, which can be distinctly untangled by virtue of the Gouy-Chapman-Stern model in classical electric double layer theory.[198] Under actual operation conditions, the working electrode with a negative bias will cause hydrated cations to adsorb

on the outer Helmholtz plane, which shields the electric field in the diffusion layer and effectively restrains the migration of hydronium ions to the electrode surface and the consequent HER adverse reaction. Concurrently, the dense hydrated cation layer on the outer Helmholtz plane will exert a positive electric field toward the electrode on the Stern layer, stabilizing intermediates in the CO_2RR with a electric dipole moment. As an example, Hu et al. levered the cation effect in a strong acid electrolyte to startlingly steered 88.0% selectivity of Sn_2O/C for formate at a current density of 314 mA cm^{-2}, 91.0% selectivity of Au/C for CO at a current density of 227 mA cm^{-2}, and 25.0% selectivity of Cu/C for ethylene at a current density of 136 mA cm^{-2}, for which the CO_2 conversion efficiency is comparable to that of contrast in alkaline media.[199] The impact of cations was found to be related to the hydrated metal cation radii, which exhibit an inverted trend compared to ion radii. As metal ions increase from Li+ to K+ and finally to Cs+, the radii of hydrated ions decrease, leading to the formation of a denser cationic hydrated layer in the outer Helmholtz plane, resulting in a stronger interfacial electric field that supports the conversion of CO_2 in the unfavorable hydrogen-rich environment (**Figure 8a**).

Distinguished from the ideal planar structure in the model electrode, due to the fluctuating catalytic surface morphology and electrostatic repulsion, the charges tend to accumulate in the high curvature area with sharp edges, resulting in the interfacial electric field induced by the morphology.[200] The electric double layer at the electrode/electrolyte interface is a highly complex system, and the varied distribution of electric fields at the electrode interface can lead to changes in the distribution of cations. Eliminating the interference of the cation effect in the assessment of morphology-induced interfacial electric field is challenging, making the investigation of the underlying mechanism for CO_2RR enhancement from an integrated perspective a prerequisite.. In a seminal study by Sargent et al. finite element simulations uncovered the intensified electric field on high-curvature Au nanoneedles.[201] This locally enhanced electrostatic field enriched the concentration of surface-adsorbed K^+, which stabilized key carbonaceous intermediates toward CO production

(Figure 8b-c). Liu et al. further elucidated the crucial impact of structural arrangement in field-enhanced electrocatalysis.[202] They observed a stronger local electric field and higher K^+ adsorption capacity on ordered Cu nanoneedle arrays compared to Cu nanoneedle electrodes with random orientation (Figure 8d-e). Importantly, the reaction energy of C-C coupling was demonstrated to be reduced with a higher local K^+ concentration, providing a possible explanation for the experimentally obtained superior C_2 product FE of 59% on the orderly arranged Cu catalyst. In contrast, the corresponding selectivity on the poorly arranged Cu catalyst was merely 20%. The localized electron density induced by high-curvature metallic nanostructures increases the probability of collective collision among charges, resulting in an increase in local temperature. This acts synergistically with the enhanced spatial electric field to lower the electrochemical reaction energetics and boost the reaction rate. Noticeably, surface modification of the dielectric polymer could further enhance the tip-induced electric−thermal field effect. This hypothesis was confirmed in a proof-of-concept study using polytetrafluoroethylene (PTFE)-coated Cu nanoneedles, and the promotional role of PTFE in electric-thermal generation was evaluated using K^+ adsorption capacity as a surrogate descriptor. The effect was further visualized using infrared thermal imaging techniques.[203] Upon optimized PTFE modification, a remarkable C_2 FE of 85.4% at 300 mA cm^{-2} was achieved, which was attributed to both thermodynamically and kinetically accelerated *CO dimerization processes (Figure 8f).

The surface modification of organic species can also expedite the conversion efficiency of CO_2 by strengthening the interfacial electric field. Wang et al. demonstrated that modifying a Cu catalyst with organosuperbase molecules, which have strong proton trapping ability, led to a positive charge layer that tightly adhered to the negative Cu electrode surface via electrostatic interactions. This compact layer contributed to an enhanced interfacial electric field that reduced the affinity strength and coupling energy barrier of *CO, resulting in a maximal 80.0% selectivity for C^{2+} at a current density of 270 mA cm^{-2}.[204]

A persistent challenge in previous research contributions has been to ensure an adequate supply of proton

*H, as the limited CO_2 mass transfer in H-type cells restricts the consumption rate of *H, which can lead to undesired HER selectivity. As the reaction device is iteratively upgraded to the flow cell configuration, the CO_2 feed flows alongside the GDE, entering the porous gas diffusion medium and finally approaching the catalyst layer.[32, 205] Sufficient CO2 mass transfer is crucial to ensure an adequate supply of *H, which unilaterally originates from the bulk electrolyte and is the rate-determining step in the process of PCET activation towards carbonaceous intermediates; note that it is equally important to balance the local concentrations of gaseous reactant and liquid electrolyte with a moderate *H content.[196, 197, 206-208] Modification of hydrophilic species was proven to enhance the formate pathway due to the formation of surface hydrides. Wang et al. proposed that the S species on the In catalyst surface can interact with the hydrated metal cations in the double layer to promote the adsorption of *H species by activating water molecules, which lowers the Gibbs free energy to form HCOO* and HCOOH* and dramatically refines the catalytic performance for the CO_2RR toward formate (**Figure 9a**).[209]

The proton-assisted boosting strategy has a wide range of universality, with remarkable achievements in CO, CH_4 and even C_{2+} products except formic acid. The *CHO intermediate (*CO + *H + e^- → *CHO is hindered by a limited rate of proton delivery, which is a challenging issue that restricts the selectivity of CH4 and C_{2+} products from achieving further improvement. Chen et al. decorated Cu_3N/Cu_2O hybrid materials with single atom Ir to form a tandem multifunctional catalyst, in which Ir sites fed *H to vicinal Cu sites, promoting hydrolytic dissociation to realize the facile generation of *CHO, finally enabling a 75.0% FE of CH_4 with a current density of 320 mA cm^{-2} (Figure 9b-c).[210] Nørskov's group has shown that, upon appropriate coverage of *CHO, the dimerization energy barrier of *CHO is more favorable than that of the *CO coupling pathway. Building on this insight, Wang and colleagues proposed that F modification could improve water dissociation and proton *H feeding, leading to an optimized energy barrier for *CHO that enables it to replace *CO in the C-C coupling mechanism. The resulting F-modified Cu catalyst exhibited an

excellent current density of 1.6 A cm^{-2} and a C^{2+} FE of approximately 80.0% (Figure 9d-e).[57]

4. Reactor configuration upgrade for CO_2RR

Thus far, CO_2RR electrocatalysts have been considerably enhanced in terms of catalytic activity and product selectivity through the implementation of various advanced material design strategies. Nevertheless, in the CO_2RR system, the reaction device plays an equally important role as the electrocatalysts, and the optimization of the device configuration can significantly enhance the overall catalytic performance. The development of CO_2RR reaction devices has undergone iterative upgrades along with the refinement of research objectives and the pursuit of higher performance metrics. These devices can be broadly divided into three periods of development.

The H-type electrolyzer, being the earliest and most widely employed experimental setup, remains a popular choice for rapid catalyst screening owing to its straightforwardness and ease of use in experimentation. During this time, studies primarily centered around the catalyst and fundamental principles of CO_2RR, with little emphasis on the reaction device itself. Despite significant progress in investigating CO_2 dissolved in water as a reactant, the low reaction rate owing to limited CO_2 solubility has hindered the advancement of CO_2RR. Later, the emergence of the liquid phase flow cell inspired an alternative way to supply CO_2. The introduction of the GDE enables direct contact between the gaseous CO2 and catalyst layer, which can greatly promote the mass transfer rate of CO_2. The current density thus broke the 50 mA^{-2} limitation and even reached 1 A cm^{-2}. Anion exchange membranes enable the use of highly concentrated basic electrolytes, which greatly promotes catalytic activity by inhibiting hydrogen evolution and reducing overpotential but also brings some negative effects such as (bi)carbonation. More recently, acidic electrolytes have been restudied aiming to reduce carbon loss, where metal cation action is closely related to catalytic performance and will be described in detail in the following sections. During this period, researchers paid attention to the reaction electrolyzer and the consequent difficulties, such as the mass transfer of CO_2, the matching between the

diffusion layer and the catalyst layer, and the hydrophilic and hydrophobic properties of the GDE. To alleviate the problem of (bi)carbonation and electroinfiltration of GDE, another reaction device, a gas phase flow cell, is designed for CO_2RR. The gas phase flow cell fundamentally differs from the liquid phase flow cell in that the cathode liquid is eliminated between the cathode GDE and the ion exchange membrane. This reaction configuration offers several advantages. For example, it can reduce ohmic resistance and cell potential. The electrolyte-free system has a more stable microenvironment and avoids impurities in the product. During this period, people began to pay attention to product separation, electrolyte consumption, and ultralong stability.

Starting from the most basic H-type electrolyzer, this chapter will progressively introduce the liquid phase electrolyzer, gas phase electrolyzer and solid state electrolyzer to tackle the limitations and challenges faced in practical applications and discuss the intersection and integration, inheritance and breakthrough between devices from the perspective of iterative upgrading logic. In addition, the mechanism and influence of specific components in the device configuration, such as the electrolyte, ion exchange membrane and GDE, and also the temperature and pressure in the operating conditions on the CO_2RR are also discussed.

4.1. H-type electrolyzer

The schematic of the H-type electrolyzer is shown in **Figure 10a**, in which the working electrode, reference electrode, and counter electrode are placed in two reaction chambers (cathode and anode). The two chambers are separated by an ion-exchange membrane, and the catalyst is deposited on a carbon substrate (i.e., carbon paper or glassy carbon electrode).[211] During the operation, the reacting gas (e.g., CO_2) is purged and dissolved in the electrolyte, forming a liquid–solid two-phase reaction interface between the electrolyte solution and the electrode.

An H-type electrolyzer, given its simplicity, accommodates almost all types of electrodes, as simple as metal foil or blocks: different kinds of metal catalysts have been studied in detail by Hori in the 1980s,[77-80] and the results show that Cd, Sn, Pb and In metals have the characteristics of formic acid production, Zn, Ag

and Au can produce CO, and the main products of Ni and Fe are H_2, while only Cu catalysts can produce hydrocarbon products. These conclusions are still proven to be correct for nanostructured catalysts. In short, the H-type cell is suitable for rapid catalyst screening for CO_2RR at a laboratory scale and works like a standard "benchmark" reactor for catalyst screening research. However, the reaction rate of the CO_2RR is usually limited by the mass transport rate of CO_2 due to its low solubility in the electrolyte (34 mM at room temperature).[212] As a related limitation, the low diffusion coefficient of CO_2 molecules in the aqueous electrolyte causes concentration polarization in the bulk electrolyte.[213] The limitation becomes even worse when a porous electrode is used due to the thin diffusion layer.[214]

Some researchers have proposed methods to solve this inherent defect. For instance, Burdine et al. designed nanostructured electrodes to enhance long-range CO_2 transport via their influence on gas evolution, effectively extending the accessibility of nanostructures into solution.[215] Pang et al. reported enhanced ethylene production rates and current densities by pushing favorable local electrolyte conditions to occur at lower relative overpotentials on oxide-derived Cu.[214] By creating electrodes with varying surface areas and mass transport properties, the ethylene partial current was able to increase to 35.6 mA cm^{-2}. Efforts have also been made to increase the gas reagent solubility in the electrolyte. For example, ionic liquids can be added to electrolytes for the CO_2 capture process. However, it is not practical because of its high cost and high viscosity.[216-219] An estimation shows that in aqueous electrolytes, the CO_2RR-specific reaction current is limited to 100 mA cm^{-2}, basically dictated by the slow CO_2 mass transport rate.[220] Obviously, this is insufficient to reach industrial demand.

4.2. Flow-type electrolyzer

The game-changing solution to the reagent transport problem in the CO_2RR was provided by the flow-type electrolyzer adopting GDE as the working electrode. Compared to H-type electrolyzers with a two-phase interface, flow-type electrolyzers can substantially increase the concentration of CO_2 gas at the gas–solid-

liquid three-phase interface created by the GDE, allowing for efficient conversion to products at the active site (Figure 10b).[37, 221] Yuan et al. made a model to show the relationship of gaseous feed concentration versus current density and the distance from the catalyst for the H-type electrolyzer and flow-type electrolyzer.[39] It was discovered that the diffusion distance from gaseous CO_2 to the liquid surrounding the catalyst surface is only approximately 50 nm compared to 50 μm in the H-type electrolyzer, indicating a 3-order-of-magnitude faster mass transport (Figure 10c-d).[222] Benefitting from the better mass transfer characteristics and shorter diffusion path, the current density can reach over 1.0 A cm^{-2}.[223] Flow-type electrolyzers can be divided into three categories according to the electrolyte at the cathode for the CO_2RR, namely, liquid phase flow cells, gas phase flow cells, and solid state flow cells.

4.2.1. Liquid phase electrolyzer

The microfluidic electrolyzer is the earliest type of liquid phase electrolyzer and is similar to microfluidic fuel cells, which do not have an ion-exchange membrane and only rely on laminar electrolyte flow to separate the cathode and anode and avoid or mitigate the crossover of products (**Figure 11a**). Inspired by the fuel cell design, Kenis and coworkers first applied a microfluidic electrolyzer to the CO_2RR.[224] Although removing the ion-exchange membrane reduces the ohmic loss of the system and alleviates salting-out issues, this system still has several drawbacks. For example, the protons formed in the anode are easily washed away by the flowing electrolyte rather than reaching the cathode electrode interface to meet the required C_{2+} formation reaction.[225] To solve this problem, an ion-exchange membrane is needed to separate the anolyte and catholyte and transport ionic charges between the electrodes, enabling the upgrading of the microfluidic electrolyzer to a liquid phase electrolyzer.[226] The most common liquid phase electrolyzer is the three-chamber-configuration cell. As shown in Figure 11b, the channels are used for the reactant gas, catholyte, and anolyte in both electrodes. The catalyst of the liquid phase electrolyzer directly contacts the catholyte, whereby the reaction gas is continuously transported to the catalyst through the GDE.

The most straightforward benefit of a liquid phase flow cell is the increase in the production rate (as measured by the partial current density of target compounds) due to the orders-of-magnitude increase in the CO_2 replenishment rate. For C_1 products, for example, the nickel phthalocyanine molecules deposited on a GDE-based liquid phase flow cell are able to increase the current density from 22.3 mA cm^{-2} to 150 mA cm^{-2} with a high CO_2 to CO conversion selectivity with 99% FE compared to the same type of catalyst in an H-cell. The Bi_2O_3@C catalyst, another example, was synthesized to convert CO_2 into formate, and the current density was over 150 mA cm^{-2} in the flow-type electrolyzer, but only 7.5 mA cm^{-2} current density was achieved in the H-type electrolyzer.[23] For C_{2+} production, the reaction rate is also greatly boosted. For instance, two types of oxide-derived Cu catalysts have a larger CO-to-C_2H_4 current density (> 150 mA cm^{-2}). However, the performance was evaluated at low current densities (< 50 mA cm^{-2}) in the H-type system, which is difficult to scale up for commercialization.[227]

A second but equally important benefit of the liquid phase flow cell comes from the use of the strong alkaline electrolyte. Generally, H-type electrolytic cells fail to operate with alkaline solutions as electrolytes, which react rapidly with CO_2 to form carbonates, further reducing the amount of dissolved CO_2 in solution that can participate in the reaction. In contrast, in the liquid phase flow cell, CO_2 gas is diffused in the gaseous form directly through the GDE to the catalytic interface to participate in the reaction, so the catalytic performance is relatively less disturbed by the carbonate side products. Sargent et al. pursued experimental and theoretical insights into the direct influence of OH^-. They found that alkaline electrolytes can suppress the reaction rate of the competing HER and promote C-C coupling by lowering the binding energy of CO on the Cu surface, delivering a 70% ethylene FE.[228] Zhuang et al. achieved a C_{2+} alcohol production rate of 126 ± 5 mA cm^{-2} with a selectivity of 32 ± 1% by increasing the C-C coupling step on a Cu-based catalyst.[229] Subsequently, Wang et al. obtained an ethanol FE of 52 ± 1% and a cathodic energy efficiency of 31% with Cu catalysts with N-doped carbon.[230] These results illustrated that the liquid phase flow cell combined with

alkaline electrolytes is efficient in achieving high performance for the CO_2RR and should have the potential to meet industrial applications.

Nevertheless, the liquid phase reactor faces two major challenges, namely, flooding and (bi)carbonation. Flooding occurs when the electrolyte penetrates through the GDE, leading to obstruction of gas permeable pores by the electrolyte and stopping the gas CO_2 from diffusing to the catalyst (Figure 11c). Consequently, only hydrogen evolution becomes the dominant feature, leading to an essential failure of the liquid phase reactor. Several hypotheses of flooding have been proposed, including the wetting characteristics of the catalytic surface under high potentials, water pumping due to ion concentration gradients, salt precipitation and the pressure difference between gas and liquid sides.[54, 231] Efforts have been made to alleviate flooding by modifying the surface of GDE to increase hydrophobicity and developing GDE of noncarbon materials. For instance, a loading of 20 wt.% PTFE in the microporous layer of GDE resulted in the best performance for the electrochemical reduction of CO_2 to CO with a Ag catalyst.[232] Wang et al. added PTFE into the catalyst layer with Sn catalyst for an improved CO_2RR to formate, and the optimal content of PTFE was 11.1 wt.%.[233] Moreover, some researchers directly adopted the PTFE membrane as the GDE because PTFE membranes have a better resistance for flooding than traditional carbon-based GDE, but how to solve the poor conductivity of PTFE membranes is an accompanying problem.[234] Usually, a conductive layer, such as carbon black, carbon nanofibers, graphene, and CNTs, is used to cover the active catalyst.

The second challenge stems from the reaction of CO_2 with an alkaline catholyte, resulting in a change in the microenvironment, as well as the waste of CO_2 reagent and the electrolyte. This challenge is usually termed (bi)carbonation depending on which salt is produced under the interface condition, but they have generally the same effects. For instance, blocking the transport channel of CO_2, impurity deposition on the catalyst, and crossover of liquid products. (Bi)carbonation can also lead to the formation of crystalline salts, giving rise to the instability of the reaction system (Figure 11d). From the industrial perspective, carbonate formation brings

a dramatic rise in the energy consumption of CO_2 reduction of up to 60%-70%.[235] Some studies have been performed to alleviate the (bi)carbonation problem. Jeanty et al. controlled the partial pressure at the GDE to monitor the electrolyte penetration and took measures of minor flooding of the GDE to clean off impurity salt deposition, which allowed the system to produce CO for over 600 h on the Ag catalyst. [259] Sinton et al. proposed a novel cascade CO_2RR system, which first reduced CO_2 to CO by a solid oxide electrolytic cell, followed by direct reduction of CO to C_{2+} products in a secondary device, completely avoiding the interference of CO_2 (bi)carbonation to the system.[236-238]

The research on CORR was only a branch of the study of CO_2RR to investigate the key intermediate *CO and related C-C coupling pathways, and its application potential was in great question because of the extremely limited solubility in aqueous electrolytes. After the liquid phase flow cell was applied to the CORR and increased the reaction rate to above 100 mA cm^{-2}, the CORR gained substantial application interest.[54, 239, 240] For example, CO reduction has achieved 68% FE for ethylene, 40% FE for ethanol, or 70% FE for acetates, all with current densities above 270 mA cm^{-2}.[241] CO reduction is found to be especially efficient in producing C_3 products. Recently, Wang et al. achieved a high n-propanol Faradaic efficiency of 36% ± 3% in the CORR at 300 mA cm−2.[242] In addition, CORR can circumvent (bi)carbonation formation in alkaline electrolytes, which brings several benefits, such as improving system stability, reducing carbon loss, and increasing single-pass conversion efficiency and energy efficiency. Jiao et al presented an exhaustive techno-economic analysis (TEA) illustrating that the production of high-volume acetic acid and ethylene through CORR can be commercially competitive compared to CO_2RR.[241] They took CO_2-to-ethylene as an example. The regeneration cost due to (bi)carbonation accounts for one-third of the total energy requirement. Finally, CORR opens a broader range of C_{2+} products through coelectrolysis, and the production of some special chemicals through CORR is an attractive strategy for reaching the market much sooner.

4.2.2. Gas phase electrolyzer

In the liquid phase flow cell, flooding occurs when the catholyte crosses the electrowet GDE over to the gas chamber, blocking the gas diffusion to the catalyst layer. The gas phase flow cell tackles this issue by removing the catholyte layer. As shown in **Figure 12a**, different from the liquid phase flow cell, the catalyst on the cathode is in close contact with the ion-exchange membrane to form a zero-gap configuration.[243] To keep the ion-exchange membrane hydrated and allow CO_2RR to take place on the cathode catalyst, the humidity must be continuously provided by the humidified reaction gas and/or water through the ion exchange membrane. Eliminating the catholyte flow channel alleviates the flooding problem to a large extent, leading to an order-of-magnitude elongation of stability. Gabardo et al. showed that the gas phase flow cell presents stable and continuous production for over 100 h at more than 100 mA cm^{-2}.[244]

The distinctive zero-gap configuration of the gas phase electrolyzer brings more advantages than stability. First, removing the cathode electrolyte channel means cutting off half of the electrolyte ohmic loss, leading to a low full-cell voltage and therefore desirable energy efficiency.[245-247] Second, the back-to-back placement between the GDE and the ion exchange membrane offers the possibility to pressurize CO_2 in a gas phase flow cell system, where the GDE would be damaged in the liquid phase flow cell when faced with pressurized CO_2 due to the lack of effective mechanical support.[248, 249]

However, the gas phase flow cell still suffers from technical shortcomings that constrain the expansion of its application scenarios. The prime concern is the discrepancies in catalytic activity with the liquid phase flow cell. To date, the maximum current density has been up to 1.6 A cm^{-2} in the liquid phase electrolyzer,[57] far greater than 300 mA cm^{-2} in the gas phase flow cell,[242] for which the absence of alkaline electrolyte is mainly responsible. [cite] Gaining from the revamping of CO_2 transport methods, liquid phase flow cells generally feature alkaline electrolytes for the purpose of inhibiting HER and accelerating CO_2 activation, while attendant GDE flooding and CO_2 (bi)carbonation issues fuel the evolution of zero-gap configuration gas phase flow cells and the prevalence of CEMs as ion exchange membranes. In the gas phase CEM electrolyzer, H^+

generated from the anodic oxygen evolution reaction crosses the CEM at the cathode to be involved in the sophisticated PCET steps of the CO_2RR.[250, 251] With the gradual accumulation of proton H^+, acidification occurs at the cathode end, which consequently promotes the HER and inhibits the CO_2RR (Figure 12b), revealing the essential factor that makes the catalytic activity of the gas phase flow cell inferior to that of the liquid phase flow cell.

In contrast, gas phase AEM electrolyzers can effectively counteract the cathodic acidification that accompanies the employment of CEM, in which water dissociation occurs at the cathode, providing protons H^+ for CO_2RR and consequential OH^- passage from the cathode to the anode via AEM (Figure 12c).[250, 252-254] Therefore, the competitiveness of the HER is dramatically weakened in gas phase AEM electrolysers, and the catalytic capacity of the CO_2RR is significantly boosted compared to that of gas phase CEM electrolysers, which can be further demonstrated by the contrasting catalytic performance of AEM-based and CEM-based gas phase electrolysers under the same experimental conditions. Aeshala et al. found that electroplated Cu catalysts in gas phase AEM electrolyzers can efficiently produce CH_4, C_2H_4 and CH_3OH, corresponding to maximum FEs of ~ 32%, 15% and 19%, respectively, at suitable cell voltages, while the FE of any product in CEM-based electrolyzers does not exceed 6%.[255]

Frustratingly, the gas phase AEM electrolyzer still has drawbacks, and the application of AEM brings some problems encountered in the liquid phase flow cell, for instance, CO_2 (bi)carbonation and liquid product crossover. In a gas phase AEM electrolyzer, rapid proton H^+ depletion enables the localized high pH environment across the catalytic interface and the inevitable (bi)carbonation of the CO_2 gas passing through the GDE. On the other hand, when OH^- is conveyed from the cathode to the anode through the AEM to complete electron conduction, it is parallelly accompanied by partial penetration of the liquid product, which will be reoxidized at the anode (Figure 12d). Volatile products, such as C_3H_7OH, C_2H_5OH, CH_3OH, acetone (C_3H_6O) and acetaldehyde (C_2H_4O), prefer evaporation through the GDE into the CO_2 off-gas, while

nonvolatile products, such as HCOOH and CH_3COOH, prefer to cross the AEM into the anolyte through electromigration.[256] The results showed that more than 40% of the alcohols produced can cross the GDE and ~ 20% of the acids produced can cross the AEM under specific experimental conditions.

The elimination of the cathode electrolyte similarly alters the electrode system of the device from a three-electrode in a liquid phase flow cell to a two-electrode system in a gas phase flow cell, where the absence of the reference electrode renders the device operable only by means of controlled voltage or current. The two-electrode system is very unfavorable for maintaining a stable cathode potential over a long period of time, which is highly recommended because the catalyst chemistry as well as the product selectivity may vary with potential. In addition, the collection and removal of liquid products is still a challenge, and the accumulation of liquid products could prevent gas diffusion. Therefore, there is still significant room in the design and operation of gas phase flow cells.

Similar to the liquid phase flow cell, the gas phase flow cell for CO_2RR can also be directly used in CORR studies. Kanan and coworkers demonstrated CO to C_{2+} products in a gas phase flow cell.[239] They optimized gas and ion transport to maximize the flux of CO through a carbon-based GDE to a Cu catalyst layer, and the CORR demonstrated a direct production of 1.1 M acetate at a cell potential of 2.4 V and a current density of >100 mA cm^{-2} over 24 h. The results showed that the CORR can attain high single-pass conversions compared with the CO_2RR in GDE cells. The CORR in the gas phase flow cell can avoid (bi)carbonation, which often occurs in the CO_2RR flow cell. Therefore, the system stability and the energy efficiency can be greatly improved.

4.2.3. Solid state electrolyzer

To address the incompatibility of liquid products with the gas phase electrolyzer, porous cation exchange resin was introduced as a solid state electrolyte component in the gas phase electrolyzer inspired by solid state batteries to form a new solid state electrolyzer that can be directly used to reduce CO_2 to generate liquid

products, whose device schematic is shown in **Figure 13a**. [257-260] Wang and coworkers adopted this solid state electrolyzer to produce a pure formic acid product.[261] In the solid state electrolyzer, both sides of the SSE are covered with AEM and CEM, and the formate anion produced by the cathode will diffuse through the AEM into the SSE and subsequently combine with the protons H^+ passing from the CEM to form formic acid and finally be carried out by the pure water flowing slowly in the SSE to obtain the formic acid solution. The selectivity of formic acid exceeded 90%, and the system could carry out a continuous experiment over 100 h to stably generate 0.1 M HCOOH with negligible degradation in selectivity and activity. Subsequently, the same team improved the method of removing the product from the reactor; that is, using inert gas instead of deionized water, pure formic acid solutions with high concentrations (up to nearly 100 wt.%) were obtained when the generated vapors were condensed (Figure 13b).[262] In addition, the solid state electrolytic cell is universal for liquid products and can be used equally well for the production of CH_3COOH, C_2H_5OH, and C_3H_7OH.

The success of the solid state electrolyzer system is primarily attributed to the accurate control of the local reaction environment, whereby the reaction products can timely cross the ion exchange membrane and be carried out of the electrolyzer by deionized water, thus maintaining the local reaction environment (i.e., pH, ion concentration) stable. The system further allows for the collection of pure liquid products, cutting out the requirement for downstream product separation and the ability to stabilize the operating potential by incorporating a reference electrode in the SSE assembly to further enhance the stability of the solid state electrolyzer. It is worth mentioning that the solid state electrolytic cell can also be used to improve the single-pass conversion efficiency of the overall system, in which the carbonate generated by the side reaction of CO_2 and OH^- will be neutralized by proton H^+ in the SSE and rerelease CO_2 to participate in the reduction reaction (Figure 13c), effectively avoiding the carbonate being oxidized to CO_2 and mixed with O_2 at the anode, which not only reduces the carbon utilization rate of the system but also increases the energy loss due to product

separation (Figure 13d).[263, 264] However, high solution ohmic resistance due to ionic conductivity still prevents the deployment of this technique, and the complex interfacial interaction between polymer electrolytes and ion exchange membranes requires long-term attention.[265-267]

4.3. Electrolyte

The electrolyte enables ionic transport and provides the reaction environment in the CO_2RR flow cell. Three different types of electrolytes have been developed: aqueous electrolytes, organic electrolytes, and ionic liquids. Here, the aqueous electrolyte will be discussed in detail, as it is the most widely used in CO_2RR research. For aqueous electrolytes, the pH and types of anions and cations are the most important factors, which mainly determine product selectivity, overpotentials, and current density in the CO_2RR system.

4.3.1 pH effects

The pH value of electrolytes is one of the most important parameters in the reaction mechanism of the CO_2RR. Many studies have shown that pH can directly affect product selectivity and reaction overpotentials.[268, 269] Only acidic and neutral electrolytes can be used in the H-type electrolyzer, as CO_2 will react with alkaline electrolytes and change the electrolyte content. Although locally high-pH conditions can be generated by rapid proton consumption, they do not essentially break through the bottleneck of low current density.

The use of a bulk alkaline electrolyte was made possible thanks to the flow-type electrolyzer. The primary remarkable advantage of an alkaline pH is the suppression of the HER, and therefore, the selectivity can be significantly improved.[270] In addition, alkaline pH has been favored for a long period mainly because of the promotion of C-C coupling. Many investigations show that the presence of OH^- lowers the energy barrier for CO dimerization, which is conducive to the formation of C_{2+} products.[271] The representative C_{2+} products of the CO_2RR are obtained under alkaline conditions, such as ethanol and ethylene.[129, 272, 273] Schouten et al. investigated the influence of pH on the CO_2RR and CORR to methane and ethylene on Cu(111) and Cu(100)

single-crystal electrodes, respectively.[274] These results proved the following reaction mechanism: pH independence for the formation of ethylene on Cu (100) via CO dimerization on this crystal facet and a pH-dependent pathway where methane and ethylene have a common intermediate (presumably CHO). They also observed that the onset potentials for the formation of ethylene on Cu (111) are closer to the onset potentials of methane, supporting a pH-dependent pathway where methane and ethylene have a common intermediate.

However, in the alkaline electrolyzer, (bi)carbonate formation imposes the main energy and carbon losses. In the reaction of CO_2 to CO, the energy efficiency (power-to-product) is only 43%, and the carbon efficiency (CO_2-to-product) is 50%, even with a high current density (200 mA cm^{-2}). It is even worse when we look at C_{2+} production. For example, there is only ~2% carbon efficiency and ~15% energy efficiency in a CO_2-to-C_2H_4 reaction.[275] Even with the gas phase electrolyte, the reaction between CO_2 and the alkaline electrolyte is not entirely eliminated. [288] HCO_3^- or CO_3^{2-} will further react with the metal cations in the electrolyte (such as Na^+ and K^+) to form crystalline salts, blocking the CO_2 transport channel, which will greatly destabilize the system. Therefore, people have revisited neutral/acidic electrolytes.[199, 276-278] Sargent and coworkers made a comprehensive TEA to assess the energy penalty and associated cost induced by CO_2 crossover.[279] Rather surprisingly, the cost of (bi)carbonate regeneration accounts for 54.5% of the alkaline flow cell. If neutral or acidic electrolytes could be used in the CO_2RR, there would be significant room for cost reduction, even if the C_{2+} FE is not as high as in the alkaline solution. As a proof-of-concept, a 50 um Cu layer on the gas diffusion substrate was deposited as the model catalyst and 1 M phosphoric acid as the electrolyte with potassium cation additives for the acidic CO_2RR.[278] Despite the continuous consumption of protons for CO_2 hydrogenation, the local surface pH remains nearly consistent with the bulk value (1.05) for a current density below 200 mA cm^{-2}. Consequently, an optimal input CO_2 utilization of 77% was obtained at a high current density of 1.2 A cm^{-2}. The use of acidic electrolytes sacrifices little catalytic performance but eliminates (bi)carbonation and improves CO_2 utilization efficiency, making it more competitive in the energy market.

Here, we also note that CORR does not have the (bi)carbonation issue with alkaline electrolytes because CO does not directly react with base. Several recent articles show that CO can be transformed to C_{2+} production at high reaction rates, high C_{2+} selectivity, and inherently improved electrolyte stability. Jiao et al. achieved a C_{2+} Faraday efficiency of 91% with a C_{2+} partial current density over 630 mA cm^{-2} with a CO flow-type electrolyzer by controlling the electrode-electrolyte interface.[240] More recently, Wang et al achieved, at 300 mA cm^{-2}, a high n-propanol Faradaic efficiency of 36% ± 3%, a C_{2+} Faradaic efficiency of 93%, and a single-pass CO conversion of 85%. This system stability, up to 100 hours, makes the CORR very valuable for commercialization.[242]

4.3.2 Anions

The common aqueous solution-involved anions are (bi)carbonate in the H-cell and hydroxide in the flow cell. The concentration of both kinds of anions determines the pH value of the solution, and the pH effects have been discussed above in detail. Nevertheless, the influence of some additive anions of sulfate and halides on the CO_2RR is also demonstrated. For example, the activity and selectivity of Cu catalysts for the CO_2RR can be tuned by introducing halides (i.e., Cl^-, Br^-, and I^-) into the electrolyte.[280] The addition of Cl^- and Br^- improves the selectivity toward CO, while the presence of I^- reduces the CO selectivity but enhances methane selectivity up to 6 times compared with halide-free conditions. The performance difference over the same Cu catalyst is mainly attributed to halide adsorption on the catalyst. It will bring an increased negative charge on the catalyst surface, which hinders side reactions (mostly HER) at low overpotentials and promotes CO protonation at higher overpotentials. Since the I^- species show the largest negative charge, the addition of I^- will promote processes predominantly taking place at higher overpotential (e.g., hydrocarbon production) to form methane.

4.3.3 Cations

The electrical double-layer model is the basis of the electrochemical CO_2 reduction reaction at the

electrolyte-electrode interface. The working electrode is negatively biased, and the catalyst layer is enriched with cations relative to the concentrations of anions. Various hypotheses for cationic effects have been proposed. By affecting the thickness of the electrical double layer, the cation is negatively correlated with the intensity of the electromagnetic field.[281] Cations also affect the local concentration and stability of CO_2 and reaction intermediates, which is important for the selectivity of products.[282] Note that under different voltages or different cations, the effects on the hydrolysis reaction and HER reaction cannot be generalized.[198, 283, 284]

Compared to anion studies, cation effects have received more attention in the field of CO_2RR, specifically the influence of alkali metals.[285, 286] Resasco et al. presented experimental and theoretical studies to elucidate the effects of alkali metal cations (e.g., Na^+, K^+, and Cs^+) on the intrinsic activity of metal catalysts for the CO_2RR.[287] Very interestingly, the current density for the CO_2RR increased with the cation size. In addition, the pKa for cation hydrolysis decreases with increasing cation size, and larger alkaline metal cations (e.g., K^+, Rb^+, and Cs^+) can serve as buffering agents to reduce the pH near the interface of the cathode, thereby increasing the local concentration of CO_2 at the interfacial region.[213] Consequently, the FEs for H_2 and methane formation decrease, and the FEs for ethanol and ethylene formation over Cu cathodes increase with increasing cation size of alkaline metals. Moreover, a higher concentration of K^+ ions was proven to stabilize the $*CO_2^{\bullet-}$ radical intermediate, the usual rate-limiting step, by reducing the resistances of charge transfer.[288] Therefore, K^+ ions are widely used as the cation of electrolytes (e.g., KCl, KOH, and $KHCO_3$) in CO_2RR research. The effects of multivalent cations (Li^+, Cs^+, Be^{2+}, Mg^{2+}, Ca^{2+}, Ba^{2+}, Al^{3+}, Nd^{3+}, and Ce^{3+}) were also systematically studied in mildly acidic electrolytes. The acidic cations only favor the CO_2RR at low overpotentials and in acidic media. The CO_2-to-CO activity shows an interplay between concentration at the outer Helmholtz plane, with specific cation-promoting effects on water dissociation and cation stabilization of $*CO_2^{-}$, determining the CO_2RR vs H_2O reduction competition.[284]

4.4. Temperature

The effects of temperature on the CO_2RR are multisided. Under different temperatures, such as pH (local and overall), CO_2 solubility and diffusion, electrolyte resistance, and adsorbed intermediates can change, which in turn affects the reaction process of the CO_2RR. Additionally, the physical structure of the catalytic layer, ion exchange membrane, and other system components are also affected by temperature and affect the stability of the catalytic system.

Many temperature studies have been conducted in H-cell reactors. Hashiba et al. investigated the effects of CO_2 reaction temperature on the reaction products of the CO_2RR over a Cu catalyst.[289] Lowering the temperature suppresses H_2 production and increases methane production over a wide range of current densities. These behaviors are mainly due to the decrease in CO_2 solubility at higher temperatures, and the interfacial interaction between adsorbed hydrogen is more kinetically facile, which causes an increased HER.[290] Attention is drawn to the fact that in the H-cell, although a moderate increase in temperature can reduce the ohmic resistance of the electrolyte, accelerate the reactant mass transfer rate and reduce the reaction energy barrier, it is still the CO_2 solubility that plays a decisive role in the catalytic efficiency of the CO_2RR.

Compared to the H-cell system, the decrease in CO_2 solubility with increasing temperature is less concerning for the flow cell system, which is attributed to the unique CO_2 mass transfer mode brought by GDE that properly mitigates the dominance of CO_2 solubility on the catalytic reaction, while the increase in temperature improves the reaction kinetics, thus affecting the current density, energy efficiency and product selectivity. Löwe et al. found that the CO_2RR performance of the Sn catalyst in the flow cell could be incrementally improved with a moderate increase in temperature and rendered an optimum when the operating temperature was 50 °C, which originated from the accelerated mass transfer rate.[291] However, the solubility of CO_2 shows an exponential decline at temperatures above 50 °C and will again dominate the catalytic performance in the flow-type electrolyzer, and the consumption of CO_2 will lead to higher HERs. Note that, especially in flow cells, the effect of current density on the temperature of the reaction device may be amplified,

and in reaction devices operating at industrial-grade current densities, the internal temperature may be much higher than the operating temperature, so further study of the mechanism of temperature effects on CO_2RR activity, selectivity and system stability is thus essential and meaningful.

4.5. Pressure

High-pressure conditions can increase the concentration of CO_2 reactants on the electrode interface, which allows for higher current densities and reduces the overpotential of the CO_2RR.[292] Most pressure studies have been performed in H-cell reactors in pursuit of higher CO_2 concentrations, which was highly demanded in the era of H-cells.[293-295] Moreover, high-pressure conditions suppress the side reaction of the HER and improve the product selectivity of the CO_2RR.[158, 296] For instance, Hara et al. studied the product distribution of different metal catalysts (such as Fe, Co, Rh, Ni, Pd, and Pt) under different pressure conditions in an aqueous $KHCO_3$ solution using an H-cell reactor.[294] The main reduction product of those metals was only H_2 under 1 atm CO_2, whereas CO was formed under high pressure. It is hypothesized that the high pressure of CO_2 on the catalyst surface can help the desorption of CO molecules from the catalyst surface that is otherwise tightly bound under ambient conditions.

Flow-cell techniques have been widely adopted, and the CO_2 replenishment issue has been solved in theory. However, some researchers are still willing to explore high-pressure studies on the flow cell system.[249, 297] High-pressure conditions can adjust the CO_2 reactant coverage on the catalyst surface by changing the pressure, which allows for higher current densities and reduces the overpotential of the CO_2RR.[298] Moreover, the pressure effect on product selectivity was also observed in the flow cell system. Gabardo et al. designed a high-pressure flow cell system with a Ag catalyst for the efficient conversion of CO_2 to CO.[299] The FE of CO increases with increasing pressure, while the FE of formate changes in the opposite direction. There are two possible hypotheses. One is that the CO_2 surface coverage increases with increasing pressure, which will lead to a reduction in protons adsorbed on the catalyst surface, but the adsorbed hydrogen on the surface favors

formate production. Another hypothesis is that the increased concentration of CO_2 could lead to the reaction switching to another reaction pathway, which utilizes two CO_2 molecules in the rate-determining step and favors CO over formate production. Overall, pressure management is critical to the design of CO_2 electrolyzers, and future work will focus on understanding the relationship between pressure variation, catalytic performance and product selectivity.

5. Perspectives

The transition from the traditional petrochemical supply chain to carbon-neutral manufacturing is rapidly gaining momentum worldwide. To this end, coupling CO_2RR with renewable electricity to yield value-added fuels and storable feedstocks that are foundations of the modern chemical industries is becoming a pressing priority. This review provides a detailed examination of the recent developments in electrochemical CO_2 conversion. Our scope not only includes the fundamental disciplines of the CO_2RR technique but also emphasizes the rational design of electrocatalysts with insights into their structure-property correlation for targeted products. More importantly, laborious propositions regarding device engineering and upscaling from benchtop exploitation to industrial relevance are also recognized herein. Despite the great endeavors made by contemporary research communities in this area, there are several pressing challenges tht must be addressed to facilitate the exploration of electrocatalysts and bring the CO_2RR technology closer to practical and commercial implementation. To overcome the existing challenges and enhance the efficiency of CO_2RR technology, we recommend exploring several research directions that could significantly advance the field.

(i) The carefully designed CO_2RR electrocatalysts satisfy the performance metrics required for practical applications but are still full of thorns and challenges to achieve real commercial scale. The primary issue to be addressed is the selectivity for multi-carbon products. To date, most CO_2RR studies have been limited to small molecule products such as one- and two-carbon products, and the selective and efficient conversion of CO_2 into carbon-based long-chain molecules still faces serious challenges. In view of this, coupling CO_2

electrolysis with biofermentation and thermocatalytic conversion technologies is a feasible pathway. In addition, exploring external field-assisted CO_2RR systems is also expected to open up new research fields at this stage. The introduction of external effects such as light, magnetism, electricity and heat will bring additional driving force to the electrocatalytic reaction, providing an important opportunity to break the bottleneck of electrocatalytic activity and selectivity. The second priority is the large-scale preparation of electrocatalysts. The elaborate construction of electrocatalysts necessitates complex and iterative preparation processes, with low yields and excessive costs, completely unable to fulfill the gram or even kilogram levels required for industrial applications. Integrating the feasibility, energy consumption and economic burden of synthesis protocols to obtain superior catalysts in a facile and economical way is a need and a challenge.

(ii) Another bottleneck of the CO_2RR is the kinetically sluggish anode water oxidation reaction. Its reaction process not only produces low value-added O_2 but also forms reactive oxygen species that can lead to ion exchange membrane failure, reducing CO_2 electrolysis efficiency and operating life. Choosing a thermodynamically more favorable oxidation reaction at the anode as an alternative upgrade can not only realize the value addition of the anode product but also significantly improve the energy efficiency of the whole electrolytic system. However, the current exploration of anodic reactions is mainly limited to simple organic small molecules, and the substrate selection for anodic oxidation reactions needs to be further broadened. Take the degradation of waste plastics, such as polyethylene terephthalate and polyethylene naphthalene dicarboxylate, for example, which are rich in glycol monomers and can selectively prepare high value-added chemicals such as hydroxyacetic acid and terephthalic acid through electrocatalytic oxidation. Therefore, the development of simultaneous conversion of CO_2 and waste plastics to value-added molecules will significantly enhance the environmental friendliness and economic feasibility of CO_2RR.

(iii) Most current CO_2RR studies have been carried out in strongly alkaline electrolytes, whose high pH is conducive to suppressing hydrogen precipitation side reactions and promoting the C-C coupling process.

However, in the actual electrolysis process, the majority of CO_2 reacts with the electrolyte to form carbonate, which significantly reduces the efficiency of CO_2 utilization and brings about the problems of cathode salt precipitation and anode cross-contamination, which affects the reaction efficiency and stability of the electrolysis device and requires regular replacement of the electrolyte to maintain the operation of the system. The regeneration of CO_2 from carbonate solution requires a considerable amount of energy, which seriously affects the economic feasibility of the CO_2 electrolysis technology. In addition, the organic acids produced under alkaline and neutral conditions exist as salts, which need to be further acidified to obtain high-value chemicals such as organic acids, resulting in additional cost consumption. The development of an acidic CO_2 conversion system not only avoids the problems of salt precipitation and cross-contamination caused by carbonates but also enables the direct acquisition of organic acid chemicals with high purity. However, the design of electrocatalysts that are stable under acidic conditions and the suppression of hydrogen precipitation side reactions in acidic media to obtain high selectivity for CO_2 reduction need to be further explored.

(iv) The assessment of stability in electrocatalysis is a critical aspect of achieving efficient and sustainable performance in electrochemical energy technologies. Stability not only refers to the physicochemical stability of the catalytic material, but also includes the stability of solid-liquid-gas three-phase interfaces at the electrode level, and the system level. The study of electrochemical stability under service conditions is crucial to evaluate the durability of the electrocatalyst. Additionally, understanding the stability of interfaces between the electrode and reactants/products, and the stability of ion exchange membranes and external accessories, is necessary for long-term performance. It is essential to evaluate stability under actual service conditions and operating conditions to obtain valuable information. A systematic and comprehensive approach is required to address the stability concerns in electrocatalysis. A key challenge in electrocatalysis is the degradation of the catalyst, membrane, interface, and other components over time, which can lead to a decline in activity and selectivity, and ultimately, failure of the system. Therefore, the stability assessment should be prioritized, with

a focus on the design and optimization of the catalyst, the electrode, and the system as a whole. The development of stable and durable electrocatalysts requires a deep understanding of the mechanism of degradation and reconstruction, and the development of strategies to mitigate these processes. Furthermore, the innovation in electrocatalysis must involve a whole life cycle economic value analysis, including a TEA assessment of CO_2RR technology. TEA needs to consider all aspects of the product life cycle at the design stage, including material production, product manufacturing, use phase, and end-of-life management. By considering all these aspects, the economic and environmental benefits of the technology can be better evaluated and optimized, leading to the development of more sustainable and efficient electrochemical energy technologies.

(v) The traditional stationary characterizations are ambiguous to timely reveal the authentic catalytic centers during electrocatalysis. Given this shortage, direct vision into the dynamic evolution of catalysts and preferential reaction pathways at practical operation through theoretical simulation and operando techniques is well qualified and isolated out as a subproject under the CO_2RR framework. Additionally, the design of in situ electrochemical reaction cells and accurate computational models should be highlighted to lay the foundation of this field. Catalyst evolution can be readily monitored throughout catalysis, penetrating the transformation of morphology, crystal phase, and valence state. The real-time detection of the local coordination environment around the active sites can also be observed at atomic resolution. Combining the operando probing roadmap with advanced algorithms provides the theoretical basis for unveiling the reaction mechanism, visualizing the transient states of intermediates and giving their formation energy predictions. Developing mechanistic understanding using these valuable instruments is highly recommended, departing from complicated trial-and-error investigations and moving forward, accelerating the innovation of electrocatalysts.

(vi) One would anticipate that fundamental data with high quality and quantity adopted from in situ

observations and computational results can also feed into the machine-learning-aided framework in a reciprocal manner. This automated workflow can efficaciously screen and prioritize potential candidates for next-generation electrocatalysts through intermediate binding optimization and electrode-electrolyte optimization. By doing so, redundant workload in theoretical calculations can be avoided, and the research scope for experimental validation can be reduced to a manageable size in this endeavor. In addition, for the case when in situ analysis is infeasible to conduct, automating machine learning can still provide a mechanistic viewpoint of the CO_2RR process under harsh conditions. Furthermore, combining different simulation methods, such as molecular dynamics simulations, computational fluid dynamics simulations or finite-element method simulations, is another nascent mechanistic tool that can be viewed as inspiration, illuminating the underexplored ground encompassing the possibilities of catalytic behavior under different environmental conditions.

6. Conclusion

We have provided a comprehensive overview of the state-of-the-art CO_2RR technology, stretching from its foundational concepts to advanced strategies aimed at facilitating its industrialization and commercialization. Moving this field forward requires not only the assessment of target performance metrics based on full cells but also the integration of interdisciplinary developments such as fundamental science, integration engineering, profound technologies, and social-technical-economic evaluation to enable the market-ready implementation of CO_2RR technologies for a carbon-neutral society. Moreover, The principles elucidated here in the context of CO2RR have far-reaching implications for the broader field of catalysis. Specifically, these principles may be transposed to other electrocatalytic systems, such as photocatalysis and beyond, thereby advancing sustainable development of human society.

Acknowledgment

This work was supported by the National Key Research and Development Program of China (2021YFA1600800), the National Natural Science Foundation of China (22075092), the Program for HUST

Academic Frontier Youth Team (2018QYTD15), EU-Horizon 2020 and BEIS (ACT, 299668), and the Huazhong University of Science and Technology- Queen Mary University of London Strategic Partnership Research Funding (2022-HUST-QMUL-SPRF-03).

Conflict of Interest

The authors declare no conflict of interest.

References

[1] M. Rahimi, A. Khurram, T. A. Hatton, B. Gallant, *Chem. Soc. Rev.* **2022**, *51*, 8676.
[2] J. Tollefson, K. R. Weiss, *Nature* **2015**, *528*, 315.
[3] N. Kittner, F. Lill, D. M. Kammen, *Nat. Energy* **2017**, *2*, 17125.
[4] E. S. Sanz-Perez, C. R. Murdock, S. A. Didas, C. W. Jones, *Chem. Rev.* **2016**, *116*, 11840.
[5] D. W. Keith, G. Holmes, D. St. Angelo, K. Heidel, *Joule* **2018**, *2*, 1573.
[6] T. Alerte, J. P. Edwards, C. M. Gabardo, C. P. O'Brien, A. Gaona, J. Wicks, A. Obradović, A. Sarkar, S. A. Jaffer, H. L. MacLean, D. Sinton, E. H. Sargent, *ACS Energy Lett.* **2021**, *6*, 4405.
[7] S. Overa, B. H. Ko, Y. Zhao, F. Jiao, *Acc. Chem. Res.* **2022**, *55*, 638.
[8] W. Zhang, Y. Hu, L. Ma, G. Zhu, Y. Wang, X. Xue, R. Chen, S. Yang, Z. Jin, *Adv. Sci.* **2018**, *5*, 1700275.
[9] Z. Sun, N. Talreja, H. Tao, J. Texter, M. Muhler, J. Strunk, J. Chen, *Angew. Chem. Int. Ed.* **2018**, *57*, 7610.
[10] R. M. Rodrigues, X. Guan, J. A. Iñiguez, D. A. Estabrook, J. O. Chapman, S. Huang, E. M. Sletten, C. Liu, *Nat. Catal.* **2019**, *2*, 407.
[11] B. M. Tackett, E. Gomez, J. G. Chen, *Nat. Catal.* **2019**, *2*, 381.
[12] E. V. Kondratenko, G. Mul, J. Baltrusaitis, G. O. Larrazábal, J. Pérez-Ramírez, *Energy Environ. Sci.* **2013**, *6*, 3112.
[13] G. H. Han, J. Bang, G. Park, S. Choe, Y. J. Jang, H. W. Jang, S. Y. Kim, S. H. Ahn, *Small* **2023**, e2205765.
[14] Z. Zhang, Y. Zheng, L. Qian, D. Luo, H. Dou, G. Wen, A. Yu, Z. Chen, *Adv. Mater.* **2022**, *34*, e2201547.
[15] L. Li, X. Li, Y. Sun, Y. Xie, *Chem. Soc. Rev.* **2022**, *51*, 1234.
[16] T. N. Do, C. You, J. Kim, *Energy Environ. Sci.* **2022**, *15*, 169.
[17] P. Izadi, F. Harnisch, *Joule* **2022**, *6*, 935.
[18] D. Pei-lin, H. You-Jia, J. Pan, X. Bao-yu, Y. Fan, *Journal of Electrochemistry* **2019**, *25*, 426.
[19] G. Wang, J. Chen, Y. Ding, P. Cai, L. Yi, Y. Li, C. Tu, Y. Hou, Z. Wen, L. Dai, *Chem. Soc. Rev.* **2021**, *50*, 4993.
[20] R. I. Masel, Z. Liu, H. Yang, J. J. Kaczur, D. Carrillo, S. Ren, D. Salvatore, C. P. Berlinguette, *Nat Nanotechnol* **2021**, *16*, 118.
[21] F. Yang, A. L. Chen, P. L. Deng, Y. Z. Zhou, Z. Shahid, H. F. Liu, B. Y. Xia, *Chem. Sci.* **2019**, *10*, 7975.
[22] S. Chen, Y. Su, P. Deng, R. Qi, J. Zhu, J. Chen, Z. Wang, L. Zhou, X. Guo, B. Y. Xia, *ACS Catal.* **2020**, *10*, 4640.
[23] P. L. Deng, F. Yang, Z. T. Wang, S. H. Chen, Y. Z. Zhou, S. Zaman, B. Y. Xia, *Angew. Chem. Int. Ed.* **2020**, *59*, 10807.
[24] P. L. Deng, H. M. Wang, R. J. Qi, J. X. Zhu, S. H. Chen, F. Yang, L. Zhou, K. Qi, H. F. Liu, B. Y. Xia, *ACS Catal.* **2019**, *10*, 743.
[25] F. Yang, P. Deng, Q. Wang, J. Zhu, Y. Yan, L. Zhou, K. Qi, H. Liu, H. S. Park, B. Y. Xia, *J. Mater. Chem. A* **2020**, *8*, 12418.
[26] H. Xie, Z. Zhao, T. Liu, Y. Wu, C. Lan, W. Jiang, L. Zhu, Y. Wang, D. Yang, Z. Shao, *Nature* **2022**, *612*, 673.

[27] Y. Cheng, P. Hou, X. Wang, P. Kang, *Acc. Chem. Res.* **2022**, *55*, 231.
[28] H. Chen, Y. Zhou, W. Guo, B. Y. Xia, *Chinese Chem. Lett.* **2022**, *33*, 1831.
[29] B. Seger, M. Robert, F. Jiao, *Nat. Sustain.* **2023**, *6*, 236.
[30] P. Kamat, P. Christopher, *ACS Energy Lett.* **2022**, *7*, 1469.
[31] S. Overa, B. H. Ko, Y. Zhao, F. Jiao, *Acc. Chem. Res.* **2022**, *55*, 638.
[32] D. Wu, F. Jiao, Q. Lu, *ACS Catal.* **2022**, *12*, 12993.
[33] G. B. Wen, B. H. Ren, X. Wang, D. Luo, H. Z. Dou, Y. Zheng, R. Gao, J. Gostick, A. P. Yu, Z. W. Chen, *Nat. Energy* **2022**, *7*, 978.
[34] D. Wakerley, S. Lamaison, J. Wicks, A. Clemens, J. Feaster, D. Corral, S. A. Jaffer, A. Sarkar, M. Fontecave, E. B. Duoss, S. Baker, E. H. Sargent, T. F. Jaramillo, C. Hahn, *Nat. Energy* **2022**, *7*, 130.
[35] S. Zhu, E. P. Delmo, T. Li, X. Qin, J. Tian, L. Zhang, M. Shao, *Adv. Mater.* **2021**, *33*, e2005484.
[36] Y. Xue, Y. Guo, H. Cui, Z. Zhou, *Small Methods* **2021**, *5*, e2100736.
[37] E. W. Lees, B. A. W. Mowbray, F. G. L. Parlane, C. P. Berlinguette, *Nat. Rev. Mater.* **2021**, *7*, 55.
[38] D. Ma, T. Jin, K. Xie, H. Huang, *J. Mater. Chem. A* **2021**, *9*, 20897.
[39] H. Rabiee, L. Ge, X. Zhang, S. Hu, M. Li, Z. Yuan, *Energy Environ. Sci.* **2021**, *14*, 1959.
[40] M. Melchionna, P. Fornasiero, M. Prato, M. Bonchio, *Energy Environ. Sci.* **2021**, *14*, 5816.
[41] T. M. Tang, Z. L. Wang, J. Q. Guan, *Adv. Funct. Mater.* **2022**, *32*, 2111504.
[42] W. Lai, Z. Ma, J. Zhang, Y. Yuan, Y. Qiao, H. Huang, *Adv. Funct. Mater.* **2022**, *32*, 2111193.
[43] Y. Zheng, A. Vasileff, X. Zhou, Y. Jiao, M. Jaroniec, S. Z. Qiao, *J. Am. Chem. Soc.* **2019**, *141*, 7646.
[44] M. G. Kibria, J. P. Edwards, C. M. Gabardo, C. T. Dinh, A. Seifitokaldani, D. Sinton, E. H. Sargent, *Adv. Mater.* **2019**, *31*, 1807166.
[45] H. J. Peng, M. T. Tang, J. Halldin Stenlid, X. Liu, F. Abild-Pedersen, *Nat. Commun.* **2022**, *13*, 1399.
[46] S. Nitopi, E. Bertheussen, S. B. Scott, X. Liu, A. K. Engstfeld, S. Horch, B. Seger, I. E. L. Stephens, K. Chan, C. Hahn, J. K. Norskov, T. F. Jaramillo, I. Chorkendorff, *Chem. Rev.* **2019**, *119*, 7610.
[47] N. Han, P. Ding, L. He, Y. Li, Y. Li, *Adv. Energy Mater.* **2019**, *10*, 1902338.
[48] S. Vijay, W. Ju, S. Brückner, S.-C. Tsang, P. Strasser, K. Chan, *Nat. Catal.* **2021**, *4*, 1024.
[49] X. Nie, M. R. Esopi, M. J. Janik, A. Asthagiri, *Angew. Chem. Int. Ed.* **2013**, *52*, 2459.
[50] G. Zhang, T. Wang, M. Zhang, L. Li, D. Cheng, S. Zhen, Y. Wang, J. Qin, Z. J. Zhao, J. Gong, *Nat. Commun.* **2022**, *13*, 7768.
[51] Y. Zhang, L. Z. Dong, S. Li, X. Huang, J. N. Chang, J. H. Wang, J. Zhou, S. L. Li, Y. Q. Lan, *Nat. Commun.* **2021**, *12*, 6390.
[52] A. J. Garza, A. T. Bell, M. Head-Gordon, *ACS Catal.* **2018**, *8*, 1490.
[53] J. Yu, J. Wang, Y. Ma, J. Zhou, Y. Wang, P. Lu, J. Yin, R. Ye, Z. Zhu, Z. Fan, *Adv. Funct. Mater.* **2021**, *31*, 2102151.
[54] W. Ma, X. He, W. Wang, S. Xie, Q. Zhang, Y. Wang, *Chem. Soc. Rev.* **2021**, *50*, 12897.
[55] H. H. Heenen, H. Shin, G. Kastlunger, S. Overa, J. A. Gauthier, F. Jiao, K. Chan, *Energy Environ. Sci.* **2022**, *15*, 3978.
[56] K. Yao, J. Li, H. Wang, R. Lu, X. Yang, M. Luo, N. Wang, Z. Wang, C. Liu, T. Jing, S. Chen, E. Cortes, S. A. Maier, S. Zhang, T. Li, Y. Yu, Y. Liu, X. Kang, H. Liang, *J. Am. Chem. Soc.* **2022**, *144*, 14005.
[57] W. Ma, S. Xie, T. Liu, Q. Fan, J. Ye, F. Sun, Z. Jiang, Q. Zhang, J. Cheng, Y. Wang, *Nat. Catal.* **2020**, *3*, 478.
[58] S. Liu, B. Zhang, L. Zhang, J. Sun, *J. Energy Chem.* **2022**, *71*, 63.
[59] Q. Fan, M. Zhang, M. Jia, S. Liu, J. Qiu, Z. Sun, *Mater. Today Energy* **2018**, *10*, 280.
[60] Y. Ji, Z. Chen, R. Wei, C. Yang, Y. Wang, J. Xu, H. Zhang, A. Guan, J. Chen, T.-K. Sham, J. Luo, Y. Yang, X. Xu, G. Zheng, *Nat. Catal.* **2022**, *5*, 251.
[61] M. Luo, A. Ozden, Z. Wang, F. Li, J. Erick Huang, S. F. Hung, Y. Wang, J. Li, D. H. Nam, Y. C. Li, Y. Xu,

R. Lu, S. Zhang, Y. Lum, Y. Ren, L. Fan, F. Wang, H. H. Li, D. Appadoo, C. T. Dinh, Y. Liu, B. Chen, J. Wicks, H. Chen, D. Sinton, E. H. Sargent, *Adv. Mater.* **2022**, *35*, e2209567.
[62] E. L. Clark, A. T. Bell, *J. Am. Chem. Soc.* **2018**, *140*, 7012.
[63] Y. Hori, R. Takahashi, Y. Yoshinami, A. Murata, *J. Phys. Chem. B* **1997**, *101*, 7075.
[64] W. Zhou, K. Cheng, J. Kang, C. Zhou, V. Subramanian, Q. Zhang, Y. Wang, *Chem. Soc. Rev.* **2019**, *48*, 3193.
[65] Z. Mu, N. Han, D. Xu, B. Tian, F. Wang, Y. Wang, Y. Sun, C. Liu, P. Zhang, X. Wu, Y. Li, M. Ding, *Nat. Commun.* **2022**, *13*, 6911.
[66] E. L. Clark, J. Resasco, A. Landers, J. Lin, L.-T. Chung, A. Walton, C. Hahn, T. F. Jaramillo, A. T. Bell, *ACS Catal.* **2018**, *8*, 6560.
[67] Z.-Z. Niu, L.-P. Chi, R. Liu, Z. Chen, M.-R. Gao, *Energ. Environ. Sci.* **2021**, *14*, 4169.
[68] G. O. Larrazabal, P. Strom-Hansen, J. P. Heli, K. Zeiter, K. T. Therkildsen, I. Chorkendorff, B. Seger, *ACS Appl. Mater. Inter.* **2019**, *11*, 41281.
[69] X. C. Jing, F. W. Li, Y. H. Wang, *Catal. Sci. Technol.* **2022**, *12*, 2912.
[70] K. Xie, R. K. Miao, A. Ozden, S. Liu, Z. Chen, C. T. Dinh, J. E. Huang, Q. Xu, C. M. Gabardo, G. Lee, J. P. Edwards, C. P. O'Brien, S. W. Boettcher, D. Sinton, E. H. Sargent, *Nat. Commun.* **2022**, *13*, 3609.
[71] K. Xie, A. Ozden, R. K. Miao, Y. Li, D. Sinton, E. H. Sargent, *Nat. Commun.* **2022**, *13*, 3070.
[72] N. Govindarajan, G. Kastlunger, H. H. Heenen, K. Chan, *Chem. Sci.* **2021**, *13*, 14.
[73] B. Chen, B. Li, Z. Tian, W. Liu, W. Liu, W. Sun, K. Wang, L. Chen, J. Jiang, *Adv. Energy Mater.* **2021**, *11*, 2102152.
[74] T. E. Teeter, P. Van Rysselberghe, *J. Chem. Phys.* **1954**, *22*, 759.
[75] S. Meshitsuka, M. Ichikawa, K. Tamaru, *J.C.S. Chem. Commun.* **1974**, *15*, 897.
[76] K. Lei, B. Yu Xia, *Chemistry* **2022**, *28*, e202200141.
[77] Y. Hori, K. Kikuchi, A. Murata, S. Suzuki, *Chem. Lett.* **1986**, *15*, 897.
[78] Y. Hori, H. Wakebe, T. Tsukamoto, O. Koga, *Electrochim. Acta* **1994**, *39*, 1833.
[79] Y. Hori, A. Murata, *Electrochim. Acta* **1990**, *35*, 1777.
[80] Y. Hori, K. Kikuchi, S. Suzuki, *Chem. Lett.* **1985**, *14*, 1695.
[81] D. Yang, B. Ni, X. Wang, *Adv. Energy Mater.* **2020**, *10*, 2001142.
[82] S. Zhang, Q. Fan, R. Xia, T. J. Meyer, *Acc. Chem. Res.* **2020**, *53*, 255.
[83] Z. Wang, R. Qi, D. Liu, X. Zhao, L. Huang, S. Chen, Z. Chen, M. Li, B. You, Y. Pang, B. Y. Xia, *ChemSusChem* **2021**, *14*, 852.
[84] Z. Wang, Y. Zhou, D. Liu, R. Qi, C. Xia, M. Li, B. You, B. Y. Xia, *Angew. Chem. Int. Ed.* **2022**, *61*, e202200552.
[85] Z. Wang, Y. Zhou, C. Xia, W. Guo, B. You, B. Y. Xia, *Angew. Chem. Int. Ed.* **2021**, *60*, 19107.
[86] Y. Han, Z. Wang, X. Han, W. Fang, Y. Zhou, K. Lei, B. You, H. S. Park, B. Y. Xia, *ACS Sustain. Chem. Eng.* **2021**, *9*, 2609.
[87] Y. Zhou, Z. Wang, W. Fang, R. Qi, Z. Wang, C. Xia, K. Lei, B. You, X. Yang, Y. Liu, W. Guo, Y. Su, S. Ding, B. Y. Xia, *ACS Catal.* **2023**, *13*, 2039.
[88] Z. Sun, Y. Hu, D. Zhou, M. Sun, S. Wang, W. Chen, *ACS Energy Lett.* **2021**, *6*, 3992.
[89] F. Pan, X. Yang, T. O'Carroll, H. Li, K. J. Chen, G. Wu, *Adv. Energy Mater.* **2022**, *12*, 2200586.
[90] G. Wen, B. Ren, Y. Zheng, M. Li, C. Silva, S. Song, Z. Zhang, H. Dou, L. Zhao, D. Luo, A. Yu, Z. Chen, *Adv. Energy Mater.* **2021**, *12*, 2103289.
[91] H. Niu, C. Xia, L. Huang, S. Zaman, T. Maiyalagan, W. Guo, B. You, B. Y. Xia, *Chin. J. Catal.* **2022**, *43*, 1459.
[92] C. Liu, X. R. Shi, K. Yue, P. Wang, K. Zhan, X. Wang, B. Y. Xia, Y. Yan, *Adv. Mater.* **2023**, *35*, e2211177.
[93] J. Greeley, M. Mavrikakis, *Nat. Mater.* **2004**, *3*, 810.

[94] M. Li, S. Garg, X. Chang, L. Ge, L. Li, M. Konarova, T. E. Rufford, V. Rudolph, G. Wang, *Small Methods* **2020**, *4*, 2000033.
[95] Z. Zhao, G. Lu, *J. Phys. Chem. C* **2019**, *123*, 4380.
[96] B. Zhang, B. Zhang, Y. Jiang, T. Ma, H. Pan, W. Sun, *Small* **2021**, *17*, e2101443.
[97] K. Maiti, S. Maiti, M. T. Curnan, H. J. Kim, J. W. Han, *Adv. Energy Mater.* **2021**, *11*, 2101670.
[98] T. N. Nguyen, M. Salehi, Q. V. Le, A. Seifitokaldani, C. T. Dinh, *ACS Catal.* **2020**, *10*, 10068.
[99] Y. Cheng, S. Yang, S. P. Jiang, S. Wang, *Small Methods* **2019**, *3*, 1800440.
[100] M. Li, H. Wang, W. Luo, P. C. Sherrell, J. Chen, J. Yang, *Adv. Mater.* **2020**, *32*, e2001848.
[101] X. Su, X. F. Yang, Y. Huang, B. Liu, T. Zhang, *Acc. Chem. Res.* **2019**, *52*, 656.
[102] Y. Chen, S. Ji, C. Chen, Q. Peng, D. Wang, Y. Li, *Joule* **2018**, *2*, 1242.
[103] Y. Li, X. F. Lu, S. Xi, D. Luan, X. Wang, X. W. D. Lou, *Angew. Chem. Int. Ed.* **2022**, *61*, e202201491.
[104] Y. Li, N. M. Adli, W. Shan, M. Wang, M. J. Zachman, S. Hwang, H. Tabassum, S. Karakalos, Z. Feng, G. Wang, Y. C. Li, G. Wu, *Energy Environ. Sci.* **2022**, *15*, 2108.
[105] J. R. Huang, X. F. Qiu, Z. H. Zhao, H. L. Zhu, Y. C. Liu, W. Shi, P. Q. Liao, X. M. Chen, *Angew. Chem. Int. Ed.* **2022**, *61*, e202210985.
[106] Y. Zhang, L. Jiao, W. Yang, C. Xie, H. L. Jiang, *Angew. Chem. Int. Ed.* **2021**, *60*, 7607.
[107] X. Yang, J. Cheng, X. Yang, Y. Xu, W. Sun, N. Liu, J. Zhou, *Nanoscale* **2022**, *14*, 6846.
[108] Z. Zeng, L. Y. Gan, H. Bin Yang, X. Su, J. Gao, W. Liu, H. Matsumoto, J. Gong, J. Zhang, W. Cai, Z. Zhang, Y. Yan, B. Liu, P. Chen, *Nat. Commun.* **2021**, *12*, 4088.
[109] L. Jiao, J. Zhu, Y. Zhang, W. Yang, S. Zhou, A. Li, C. Xie, X. Zheng, W. Zhou, S. H. Yu, H. L. Jiang, *J. Am. Chem. Soc.* **2021**, *143*, 19417.
[110] Y. Li, W. Shan, M. J. Zachman, M. Wang, S. Hwang, H. Tabassum, J. Yang, X. Yang, S. Karakalos, Z. Feng, G. Wang, G. Wu, *Angew. Chem. Int. Ed.* **2022**, *61*, e202205632.
[111] W. Rong, H. Zou, W. Zang, S. Xi, S. Wei, B. Long, J. Hu, Y. Ji, L. Duan, *Angew. Chem., Int. Ed.* **2021**, *60*, 466.
[112] M. Bernal, A. Bagger, F. Scholten, I. Sinev, A. Bergmann, M. Ahmadi, J. Rossmeisl, B. R. Cuenya, *Nano Energy* **2018**, *53*, 27.
[113] Z. Chen, T. Wang, B. Liu, D. Cheng, C. Hu, G. Zhang, W. Zhu, H. Wang, Z. J. Zhao, J. Gong, *J. Am. Chem. Soc.* **2020**, *142*, 6878.
[114] Z. Li, D. He, X. Yan, S. Dai, S. Younan, Z. Ke, X. Pan, X. Xiao, H. Wu, J. Gu, *Angew. Chem., Int. Ed.* **2020**, *59*, 18572.
[115] Y. Huang, X. Mao, G. Yuan, D. Zhang, B. Pan, J. Deng, Y. Shi, N. Han, C. Li, L. Zhang, L. Wang, L. He, Y. Li, Y. Li, *Angew. Chem., Int. Ed.* **2021**, *60*, 15844.
[116] Y. J. Ko, J. Y. Kim, W. H. Lee, M. G. Kim, T. Y. Seong, J. Park, Y. Jeong, B. K. Min, W. S. Lee, D. K. Lee, H. S. Oh, *Nat. Commun.* **2022**, *13*, 2205.
[117] Y. Zhou, F. Che, M. Liu, C. Zou, Z. Liang, P. De Luna, H. Yuan, J. Li, Z. Wang, H. Xie, H. Li, P. Chen, E. Bladt, R. Quintero-Bermudez, T. K. Sham, S. Bals, J. Hofkens, D. Sinton, G. Chen, E. H. Sargent, *Nat. Chem.* **2018**, *10*, 974.
[118] J. He, N. J. J. Johnson, A. Huang, C. P. Berlinguette, *ChemSusChem* **2018**, *11*, 48.
[119] C. Kim, F. Dionigi, V. Beermann, X. Wang, T. Moller, P. Strasser, *Adv. Mater.* **2019**, *31*, e1805617.
[120] S. Chatterjee, C. Griego, J. L. Hart, Y. Li, M. L. Taheri, J. Keith, J. D. Snyder, *ACS Catal.* **2019**, *9*, 5290.
[121] L. Jia, M. Sun, J. Xu, X. Zhao, R. Zhou, B. Pan, L. Wang, N. Han, B. Huang, Y. Li, *Angew. Chem. Int. Ed.* **2021**, *60*, 21741.
[122] C. Han, V. Kundi, Z. Ma, C. Y. Toe, P. Kumar, C. Tsounis, J. Jiang, S. Xi, Z. Han, X. Lu, R. Amal, J. Pan, *Adv. Funct. Mater.* **2023**, *33*, 2210938.

[123] S. Jeong, M. H. Choi, G. S. Jagdale, Y. Zhong, N. P. Siepser, Y. Wang, X. Zhan, L. A. Baker, X. Ye, *J. Am. Chem. Soc.* **2022**, *144*, 12673.
[124] H. Li, P. Yu, R. Lei, F. Yang, P. Wen, X. Ma, G. Zeng, J. Guo, F. M. Toma, Y. Qiu, S. M. Geyer, X. Wang, T. Cheng, W. S. Drisdell, *Angew. Chem. Int. Ed.* **2021**, *60*, 24838.
[125] W. Luo, X. Nie, M. J. Janik, A. Asthagiri, *ACS Catal.* **2016**, *6*, 219.
[126] G. Zhang, Z. J. Zhao, D. Cheng, H. Li, J. Yu, Q. Wang, H. Gao, J. Guo, H. Wang, G. A. Ozin, T. Wang, J. Gong, *Nat. Commun.* **2021**, *12*, 5745.
[127] Y. Gao, Q. Wu, X. Liang, Z. Wang, Z. Zheng, P. Wang, Y. Liu, Y. Dai, M.-H. Whangbo, B. Huang, *Adv. Sci.* **2020**, *7*, 1902820.
[128] Z. Z. Wu, X. L. Zhang, Z. Z. Niu, F. Y. Gao, P. P. Yang, L. P. Chi, L. Shi, W. S. Wei, R. Liu, Z. Chen, S. Hu, X. Zheng, M. R. Gao, *J. Am. Chem. Soc.* **2022**, *144*, 259.
[129] A. N. Xu, S. F. Hung, A. Cao, Z. B. Wang, N. Karmodak, J. E. Huang, Y. Yan, A. S. Rasouli, A. Ozden, F. Y. Wu, Z. Y. Lin, H. J. Tsai, T. J. Lee, F. W. Li, M. C. Luo, Y. H. Wang, X. Wang, J. Abed, Z. Y. Wang, D. H. Nam, Y. C. Li, A. H. Ip, D. Sinton, C. F. Dong, E. H. Sargent, *Nat. Catal.* **2022**, *5*, 1081.
[130] D. Gao, Y. Zhang, Z. Zhou, F. Cai, X. Zhao, W. Huang, Y. Li, J. Zhu, P. Liu, F. Yang, G. Wang, X. Bao, *J. Am. Chem. Soc.* **2017**, *139*, 5652.
[131] X.-C. Sun, K. Yuan, J.-H. Zhou, C.-Y. Yuan, H.-C. Liu, Y.-W. Zhang, *ACS Catal.* **2021**, *12*, 923.
[132] Z. Zhang, G. Wen, D. Luo, B. Ren, Y. Zhu, R. Gao, H. Dou, G. Sun, M. Feng, Z. Bai, A. Yu, Z. Chen, *J. Am. Chem. Soc.* **2021**, *143*, 6855.
[133] Q. Li, J. Fu, W. Zhu, Z. Chen, B. Shen, L. Wu, Z. Xi, T. Wang, G. Lu, J. J. Zhu, S. Sun, *J. Am. Chem. Soc.* **2017**, *139*, 4290.
[134] Y. Lai, N. B. Watkins, A. Rosas-Hernandez, A. Thevenon, G. P. Heim, L. Zhou, Y. Wu, J. C. Peters, J. M. Gregoire, T. Agapie, *ACS Central Sci.* **2021**, *7*, 1756.
[135] W. Xu, Y. Qiu, T. Zhang, X. Li, H. Zhang, *ChemSusChem* **2018**, *11*, 2904.
[136] Z. Chen, X. Zhang, W. Liu, M. Jiao, K. Mou, X. Zhang, L. Liu, *Energ. Environ. Sci.* **2021**, *14*, 2349.
[137] Q. Wang, K. Liu, K. Hu, C. Cai, H. Li, H. Li, M. Herran, Y. R. Lu, T. S. Chan, C. Ma, J. Fu, S. Zhang, Y. Liang, E. Cortes, M. Liu, *Nat. Commun.* **2022**, *13*, 6082.
[138] S. H. Lee, J. C. Lin, M. Farmand, A. T. Landers, J. T. Feaster, J. E. Aviles Acosta, J. W. Beeman, Y. Ye, J. Yano, A. Mehta, R. C. Davis, T. F. Jaramillo, C. Hahn, W. S. Drisdell, *J. Am. Chem. Soc.* **2021**, *143*, 588.
[139] J. Wang, H. Y. Tan, Y. Zhu, H. Chu, H. M. Chen, *Angew. Chem. Int. Ed.* **2021**, *60*, 17254.
[140] Z.-Z. Wu, F.-Y. Gao, M.-R. Gao, *Energy Environ. Sci.* **2021**, *14*, 1121.
[141] F. M. Li, L. Huang, S. Zaman, W. Guo, H. Liu, X. Guo, B. Y. Xia, *Adv. Mater.* **2022**, *34*, e2200840.
[142] F. Yang, W. Fang, Q. Wang, P. Deng, B. Y. Xia, *ACS Sustain. Chem. Eng.* **2022**, *10*, 4677.
[143] H. Shen, Y. Wang, T. Chakraborty, G. Zhou, C. Wang, X. Fu, Y. Wang, J. Zhang, C. Li, F. Xu, L. Cao, T. Mueller, C. Wang, *ACS Catal.* **2022**, *12*, 5275.
[144] S. Jin, W. Shao, S. Chen, L. Li, S. Shang, Y. Zhao, X. Zhang, Y. Xie, *Angew. Chem. Int. Ed.* **2022**, *61*, e202113411.
[145] X.-C. Liu, C. Wei, Y. Wu, Y. Fang, W.-Q. Li, R.-R. Ding, G. Wang, Y. Mu, *ACS Catal.* **2021**, *11*, 14986.
[146] A. Vasileff, C. Xu, Y. Jiao, Y. Zheng, S.-Z. Qiao, *Chem* **2018**, *4*, 1809.
[147] J. Greeley, T. F. Jaramillo, J. Bonde, I. B. Chorkendorff, J. K. Norskov, *Nat. Mater.* **2006**, *5*, 909.
[148] J. K. Norskov, F. Abild-Pedersen, F. Studt, T. Bligaard, *Proc. Natl. Acad. Sci.* **2011**, *108*, 937.
[149] J. T. Feaster, C. Shi, E. R. Cave, T. Hatsukade, D. N. Abram, K. P. Kuhl, C. Hahn, J. K. Nørskov, T. F. Jaramillo, *ACS Catal.* **2017**, *7*, 4822.
[150] D. Gao, H. Zhou, F. Cai, D. Wang, Y. Hu, B. Jiang, W.-B. Cai, X. Chen, R. Si, F. Yang, S. Miao, J. Wang, G. Wang, X. Bao, *Nano Res.* **2017**, *10*, 2181.

[151] M. Y. Zu, L. Zhang, C. Wang, L. R. Zheng, H. G. Yang, *J. Mater. Chem. A* **2018**, *6*, 16804.
[152] J. Sang, P. Wei, T. Liu, H. Lv, X. Ni, D. Gao, J. Zhang, H. Li, Y. Zang, F. Yang, Z. Liu, G. Wang, X. Bao, *Angew. Chem. Int. Ed.* **2022**, *61*, e202114238.
[153] T. C. Chou, C. C. Chang, H. L. Yu, W. Y. Yu, C. L. Dong, J. J. Velasco-Velez, C. H. Chuang, L. C. Chen, J. F. Lee, J. M. Chen, H. L. Wu, *J. Am. Chem. Soc.* **2020**, *142*, 2857.
[154] P. Wang, H. Yang, C. Tang, Y. Wu, Y. Zheng, T. Cheng, K. Davey, X. Huang, S. Z. Qiao, *Nat. Commun.* **2022**, *13*, 3754.
[155] T. Cheng, H. Xiao, W. A. Goddard, 3rd, *Proc. Natl. Acad. Sci.* **2017**, *114*, 1795.
[156] Y. Lum, T. Cheng, W. A. Goddard, J. W. Ager, *J. Am. Chem. Soc.* **2018**, *140*, 9337.
[157] C. Hahn, T. Hatsukade, Y.-G. Kim, A. Vailionis, J. H. Baricuatro, D. C. Higgins, S. A. Nitopi, M. P. Soriaga, T. F. Jaramillo, *Proc. Natl. Acad. Sci.* **2017**, *114*, 5918.
[158] L. Wang, S. A. Nitopi, E. Bertheussen, M. Orazov, C. G. Morales-Guio, X. Liu, D. C. Higgins, K. Chan, J. K. Nørskov, C. Hahn, T. F. Jaramillo, *ACS Catal.* **2018**, *8*, 7445.
[159] Y. C. Li, Z. Wang, T. Yuan, D. H. Nam, M. Luo, J. Wicks, B. Chen, J. Li, F. Li, F. P. G. de Arquer, Y. Wang, C. T. Dinh, O. Voznyy, D. Sinton, E. H. Sargent, *J. Am. Chem. Soc.* **2019**, *141*, 8584.
[160] Z. Zhao, G. Lu, *Adv. Energy Mater.* **2022**.
[161] L. Song, Z. Liang, M. Sun, B. Huang, Y. Du, *Energy Environ. Sci.* **2022**, *15*, 3494.
[162] J. Yin, Z. Gao, F. Wei, C. Liu, J. Gong, J. Li, W. Li, L. Xiao, G. Wang, J. Lu, L. Zhuang, *ACS Catal.* **2022**, *12*, 1004.
[163] J. Li, A. Ozden, M. Wan, Y. Hu, F. Li, Y. Wang, R. R. Zamani, D. Ren, Z. Wang, Y. Xu, D. H. Nam, J. Wicks, B. Chen, X. Wang, M. Luo, M. Graetzel, F. Che, E. H. Sargent, D. Sinton, *Nat. Commun.* **2021**, *12*, 2808.
[164] T. Li, H. Wei, T. Liu, G. Zheng, S. Liu, J. L. Luo, *ACS Appl. Mater. Inter.* **2019**, *11*, 22346.
[165] H. Pan, C. J. Barile, *Energy Environ. Sci.* **2020**, *13*, 3567.
[166] H. Wu, J. Li, K. Qi, Y. Zhang, E. Petit, W. Wang, V. Flaud, N. Onofrio, B. Rebiere, L. Huang, C. Salameh, L. Lajaunie, P. Miele, D. Voiry, *Nat. Commun.* **2021**, *12*, 7210.
[167] W. Ge, Y. Chen, Y. Fan, Y. Zhu, H. Liu, L. Song, Z. Liu, C. Lian, H. Jiang, C. Li, *J. Am. Chem. Soc.* **2022**, *144*, 6613.
[168] T. Zhang, W. Li, K. Huang, H. Guo, Z. Li, Y. Fang, R. M. Yadav, V. Shanov, P. M. Ajayan, L. Wang, C. Lian, J. Wu, *Nat. Commun.* **2021**, *12*, 5265.
[169] Y. Zhong, Y. Xu, J. Ma, C. Wang, S. Sheng, C. Cheng, M. Li, L. Han, L. Zhou, Z. Cai, Y. Kuang, Z. Liang, X. Sun, *Angew. Chem. Int. Ed.* **2020**, *59*, 19095.
[170] W. Deng, L. Zhang, L. Li, S. Chen, C. Hu, Z. J. Zhao, T. Wang, J. Gong, *J. Am. Chem. Soc.* **2019**, *141*, 2911.
[171] Y. Zhong, X. Kong, Z. Song, Y. Liu, L. Peng, L. Zhang, X. Luo, J. Zeng, Z. Geng, *Nano. Lett.* **2022**, *22*, 2554.
[172] H. Zhang, X. Chang, J. G. Chen, W. A. Goddard, 3rd, B. Xu, M. J. Cheng, Q. Lu, *Nat. Commun.* **2019**, *10*, 3340.
[173] Q. Liu, R. Liu, C. He, C. Xia, W. Guo, Z. L. Xu, B. Y. Xia, *eScience* **2022**, *2*, 453-466.
[174] J. Chen, D. Wang, X. Yang, W. Cui, X. Sang, Z. Zhao, L. Wang, Z. Li, B. Yang, L. Lei, J. Zheng, L. Dai, Y. Hou, *Angew. Chem. Int. Ed.* **2023**, *62*, e202215406.
[175] D. L. Meng, M. D. Zhang, D. H. Si, M. J. Mao, Y. Hou, Y. B. Huang, R. Cao, *Angew. Chem. Int. Ed.* **2021**, *60*, 25485.
[176] Y. Ma, J. Yu, M. Sun, B. Chen, X. Zhou, C. Ye, Z. Guan, W. Guo, G. Wang, S. Lu, D. Xia, Y. Wang, Z. He, L. Zheng, Q. Yun, L. Wang, J. Zhou, P. Lu, J. Yin, Y. Zhao, Z. Luo, L. Zhai, L. Liao, Z. Zhu, R. Ye, Y. Chen, Y. Lu, S. Xi, B. Huang, C. S. Lee, Z. Fan, *Adv. Mater.* **2022**, *34*, e2110607.

[177] J. Li, Z. Y. Wang, C. McCallum, Y. Xu, F. W. Li, Y. H. Wang, C. M. Gabardo, C. T. Dinh, T. T. Zhuang, L. Wang, J. Y. Howe, Y. Ren, E. H. Sargent, D. Sinton, *Nat. Catal.* **2019**, *2*, 1124.
[178] C. Zhu, L. Zhou, Z. Zhang, C. Yang, G. Shi, S. Zhao, H. Gu, J. Wu, X. Gao, Y. Li, K. Liu, S. Dai, L. Zhang, *Chem* **2022**, *8*, 3288.
[179] Y. C. Tan, K. B. Lee, H. Song, J. Oh, *Joule* **2020**, *4*, 1104.
[180] J. Gao, H. Zhang, X. Guo, J. Luo, S. M. Zakeeruddin, D. Ren, M. Gratzel, *J. Am. Chem. Soc.* **2019**, *141*, 18704.
[181] J. Wordsworth, T. M. Benedetti, S. V. Somerville, W. Schuhmann, R. D. Tilley, J. J. Gooding, *Angew. Chem. Int. Ed.* **2022**, *61*, e202200755.
[182] C. Liu, M. Zhang, J. Li, W. Xue, T. Zheng, C. Xia, J. Zeng, *Angew. Chem. Int. Ed.* **2022**, *61*, e202113498.
[183] T.-T. Zhuang, Y. Pang, Z.-Q. Liang, Z. Wang, Y. Li, C.-S. Tan, J. Li, C. T. Dinh, P. De Luna, P.-L. Hsieh, T. Burdyny, H.-H. Li, M. Liu, Y. Wang, F. Li, A. Proppe, A. Johnston, D.-H. Nam, Z.-Y. Wu, Y.-R. Zheng, A. H. Ip, H. Tan, L.-J. Chen, S.-H. Yu, S. O. Kelley, D. Sinton, E. H. Sargent, *Nat. Catal.* **2018**, *1*, 946.
[184] F. Li, Y. C. Li, Z. Wang, J. Li, D.-H. Nam, Y. Lum, M. Luo, X. Wang, A. Ozden, S.-F. Hung, B. Chen, Y. Wang, J. Wicks, Y. Xu, Y. Li, C. M. Gabardo, C.-T. Dinh, Y. Wang, T.-T. Zhuang, D. Sinton, E. H. Sargent, *Nat. Catal.* **2019**, *3*, 75.
[185] Z. Tao, Z. Wu, Y. Wu, H. Wang, *ACS Catal.* **2020**, *10*, 9271.
[186] Y. Guo, X. He, Y. Su, Y. Dai, M. Xie, S. Yang, J. Chen, K. Wang, D. Zhou, C. Wang, *J. Am. Chem. Soc.* **2021**, *143*, 5755.
[187] M. S. Xie, B. Y. Xia, Y. Li, Y. Yan, Y. Yang, Q. Sun, S. H. Chan, A. Fisher, X. Wang, *Energy Environ. Sci.* **2016**, *9*, 1687.
[188] X. Wei, Z. L. Yin, K. J. Lyu, Z. Li, J. Gong, G. W. Wang, L. Xiao, J. T. Lu, L. Zhuang, *ACS Catal.* **2020**, *10*, 4103.
[189] C. Chen, X. Yan, Y. Wu, S. Liu, X. Zhang, X. Sun, Q. Zhu, H. Wu, B. Han, *Angew. Chem., Int. Ed.* **2022**, *61*, e202202607.
[190] R. Chen, H. Y. Su, D. Liu, R. Huang, X. Meng, X. Cui, Z. Q. Tian, D. H. Zhang, D. Deng, *Angew. Chem. Int. Ed.* **2020**, *59*, 154.
[191] C. W. Li, J. Ciston, M. W. Kanan, *Nature* **2014**, *508*, 504.
[192] G. L. Wu, Y. R. Song, Q. Zheng, C. Long, T. Fan, Z. J. Yang, X. W. Huang, Q. Li, Y. L. Sun, L. L. Zuo, S. B. Lei, Z. Y. Tang, *Adv. Energy Mater.* **2022**, *12*, 2202054.
[193] T. Zhang, J. C. Bui, Z. Li, A. T. Bell, A. Z. Weber, J. Wu, *Nat. Catal.* **2022**, *5*, 202.
[194] J. Yu, J. Yin, R. Li, Y. Ma, Z. Fan, *Chem Catal.* **2022**, *2*, 2229.
[195] F. Shao, Z. Xia, F. You, J. K. Wong, Q. H. Low, H. Xiao, B. S. Yeo, *Angew. Chem. Int. Ed.* **2023**, *62*, e202214210.
[196] S. Chen, X. Li, C. W. Kao, T. Luo, K. Chen, J. Fu, C. Ma, H. Li, M. Li, T. S. Chan, M. Liu, *Angew. Chem. Int. Ed.* **2022**, *61*, e202206233.
[197] J. Chen, Z. Li, X. Wang, X. Sang, S. Zheng, S. Liu, B. Yang, Q. Zhang, L. Lei, L. Dai, Y. Hou, *Angew. Chem. Int. Ed.* **2022**, *61*, e202111683.
[198] B. Pan, Y. Wang, Y. Li, *Chem Catal.* **2022**, *2*, 1267.
[199] J. Gu, S. Liu, W. Ni, W. Ren, S. Haussener, X. Hu, *Nat. Catal.* **2022**, *5*, 268.
[200] H. Jiang, Z. Hou, Y. Luo, *Angew. Chem. Int. Ed.* **2017**, *56*, 15617.
[201] M. Liu, Y. Pang, B. Zhang, P. De Luna, O. Voznyy, J. Xu, X. Zheng, C. T. Dinh, F. Fan, C. Cao, F. P. de Arquer, T. S. Safaei, A. Mepham, A. Klinkova, E. Kumacheva, T. Filleter, D. Sinton, S. O. Kelley, E. H. Sargent, *Nature* **2016**, *537*, 382.
[202] Y. Zhou, Y. Liang, J. Fu, K. Liu, Q. Chen, X. Wang, H. Li, L. Zhu, J. Hu, H. Pan, M. Miyauchi, L.

Jiang, E. Cortes, M. Liu, *Nano. Lett.* **2022**, *22*, 1963.
[203] B. Yang, K. Liu, H. Li, C. Liu, J. Fu, H. Li, J. E. Huang, P. Ou, T. Alkayyali, C. Cai, Y. Duan, H. Liu, P. An, N. Zhang, W. Li, X. Qiu, C. Jia, J. Hu, L. Chai, Z. Lin, Y. Gao, M. Miyauchi, E. Cortes, S. A. Maier, M. Liu, *J. Am. Chem. Soc.* **2022**, *144*, 3039.
[204] L. Fan, C.-Y. Liu, P. Zhu, C. Xia, X. Zhang, Z.-Y. Wu, Y. Lu, T. P. Senftle, H. Wang, *Joule* **2022**, *6*, 205.
[205] C. Zhu, Y. F. Song, X. Dong, G. H. Li, A. H. Chen, W. Chen, G. F. Wu, S. J. Li, W. Wei, Y. H. Sun, *Energy Environ. Sci.* **2022**, *15*, 5391.
[206] Q. Fan, G. Bao, X. Chen, Y. Meng, S. Zhang, X. Ma, *ACS Catal.* **2022**, *12*, 7517.
[207] X. Kong, C. Wang, Z. Xu, Y. Zhong, Y. Liu, L. Qin, J. Zeng, Z. Geng, *Nano. Lett.* **2022**, *22*, 8000.
[208] X. Guo, S.-M. Xu, H. Zhou, Y. Ren, R. Ge, M. Xu, L. Zheng, X. Kong, M. Shao, Z. Li, H. Duan, *ACS Catal.* **2022**, *12*, 10551.
[209] W. Ma, S. Xie, X. G. Zhang, F. Sun, J. Kang, Z. Jiang, Q. Zhang, D. Y. Wu, Y. Wang, *Nat. Commun.* **2019**, *10*, 892.
[210] S. Chen, Z. Zhang, W. Jiang, S. Zhang, J. Zhu, L. Wang, H. Ou, S. Zaman, L. Tan, P. Zhu, E. Zhang, P. Jiang, Y. Su, D. Wang, Y. Li, *J. Am. Chem. Soc.* **2022**, *144*, 12807.
[211] C. Zhao, J. Wang, *Chem. Eng. J.* **2016**, *293*, 161.
[212] J. J. Carroll, J. D. Slupsky, A. E. Mather, *J. Phys. Chem. Ref. Data* **1991**, *20*, 1201.
[213] M. R. Singh, Y. Kwon, Y. Lum, J. W. Ager, 3rd, A. T. Bell, *J. Am. Chem. Soc.* **2016**, *138*, 13006.
[214] Y. Pang, T. Burdyny, C.-T. Dinh, M. G. Kibria, J. Z. Fan, M. Liu, E. H. Sargent, D. Sinton, *Green Chem.* **2017**, *19*, 4023.
[215] T. Burdyny, P. J. Graham, Y. Pang, C.-T. Dinh, M. Liu, E. H. Sargent, D. Sinton, *ACS Sustain. Chem. Eng.* **2017**, *5*, 4031.
[216] E. Sargeant, P. Rodríguez, *Electrochemical Science Advances* **2022**, *1*, e2100178.
[217] M. V. Fedorov, A. A. Kornyshev, *Chem. Rev.* **2014**, *114*, 2978.
[218] D. R. MacFarlane, N. Tachikawa, M. Forsyth, J. M. Pringle, P. C. Howlett, G. D. Elliott, J. H. Davis, M. Watanabe, P. Simon, C. A. Angell, *Energy Environ. Sci.* **2014**, *7*, 232.
[219] J. F. Brennecke, B. E. Gurkan, *J. Phys. Chem. Lett.* **2010**, *1*, 3459.
[220] D. M. Weekes, D. A. Salvatore, A. Reyes, A. Huang, C. P. Berlinguette, *Acc. Chem. Res.* **2018**, *51*, 910.
[221] J. Li, G. Chen, Y. Zhu, Z. Liang, A. Pei, C.-L. Wu, H. Wang, H. R. Lee, K. Liu, S. Chu, Y. Cui, *Nat. Catal.* **2018**, *1*, 592.
[222] T. Burdyny, W. A. Smith, *Energy Environ. Sci.* **2019**, *12*, 1442.
[223] W. Wang, X. Wang, Z. Ma, Y. Wang, Z. Yang, J. Zhu, L. Lv, H. Ning, N. Tsubaki, M. Wu, *ACS Catal.* **2022**, *13*, 796.
[224] D. T. Whipple, E. C. Finke, P. J. A. Kenis, *Electrochem. Solid S. T.* **2010**, *13*, D109.
[225] L. Fan, C. Xia, F. Yang, J. Wang, H. Wang, Y. Lu, *Sci. Adv.* **2020**, *6*, eaay3111.
[226] S. Liang, N. Altaf, L. Huang, Y. Gao, Q. Wang, *J. CO_2 Util.* **2020**, *35*, 90.
[227] J. Zhang, W. Luo, A. Züttel, *J. Mater. Chem. A* **2019**, *7*, 26285.
[228] C. T. Dinh, T. Burdyny, M. G. Kibria, A. Seifitokaldani, C. M. Gabardo, F. P. G. de Arquer, A. Kiani, J. P. Edwards, P. De Luna, O. S. Bushuyev, C. Q. Zou, R. Quintero-Bermudez, Y. J. Pang, D. Sinton, E. H. Sargent, *Science* **2018**, *360*, 783.
[229] T.-T. Zhuang, Z.-Q. Liang, A. Seifitokaldani, Y. Li, P. De Luna, T. Burdyny, F. Che, F. Meng, Y. Min, R. Quintero-Bermudez, C. T. Dinh, Y. Pang, M. Zhong, B. Zhang, J. Li, P.-N. Chen, X.-L. Zheng, H. Liang, W.-N. Ge, B.-J. Ye, D. Sinton, S.-H. Yu, E. H. Sargent, *Nat. Catal.* **2018**, *1*, 421.
[230] X. Wang, Z. Y. Wang, F. P. G. de Arquer, C. T. Dinh, A. Ozden, Y. G. C. Li, D. H. Nam, J. Li, Y. S.

Liu, J. Wicks, Z. T. Chen, M. F. Chi, B. Chen, Y. Wang, J. Tam, J. Y. Howe, A. Proppe, P. Todorovic, F. W. Li, T. T. Zhuang, C. M. Gabardo, A. R. Kirmani, C. McCallum, S. F. Hung, Y. W. Lum, M. C. Luo, Y. M. Min, A. N. Xu, C. P. O'Brien, B. Stephen, B. Sun, A. H. Ip, L. J. Richter, S. O. Kelley, D. Sinton, E. H. Sargent, *Nat. Energy* **2020**, *5*, 478.
[231] K. Yang, R. Kas, W. A. Smith, T. Burdyny, *ACS Energy Lett.* **2020**, *6*, 33.
[232] B. Kim, F. Hillman, M. Ariyoshi, S. Fujikawa, P. J. A. Kenis, *J. Power Sources* **2016**, *312*, 192.
[233] Q. Wang, H. Dong, H. Yu, H. Yu, *J. Power Sources* **2015**, *279*, 1.
[234] F. P. Garcia de Arquer, C. T. Dinh, A. Ozden, J. Wicks, C. McCallum, A. R. Kirmani, D. H. Nam, C. Gabardo, A. Seifitokaldani, X. Wang, Y. C. Li, F. Li, J. Edwards, L. J. Richter, S. J. Thorpe, D. Sinton, E. H. Sargent, *Science* **2020**, *367*, 661.
[235] N. Wang, K. Yao, A. Vomiero, Y. Wang, H. Liang, *SmartMat* **2021**, *2*, 423.
[236] A. Ozden, Y. Wang, F. Li, M. Luo, J. Sisler, A. Thevenon, A. Rosas-Hernández, T. Burdyny, Y. Lum, H. Yadegari, T. Agapie, J. C. Peters, E. H. Sargent, D. Sinton, *Joule* **2021**, *5*, 706.
[237] S. Zhai, H. Xie, P. Cui, D. Guan, J. Wang, S. Zhao, B. Chen, Y. Song, Z. Shao, M. Ni, *Nat. Energy* **2022**, *7*, 866.
[238] Y. Song, X. Zhang, K. Xie, G. Wang, X. Bao, *Adv. Mater.* **2019**, *31*, e1902033.
[239] D. S. Ripatti, T. R. Veltman, M. W. Kanan, *Joule* **2019**, *3*, 240.
[240] M. Jouny, W. Luc, F. Jiao, *Nat. Catal.* **2018**, *1*, 748.
[241] M. Jouny, G. S. Hutchings, F. Jiao, *Nat. Catal.* **2019**, *2*, 1062.
[242] X. Wang, P. Ou, A. Ozden, S.-F. Hung, J. Tam, C. M. Gabardo, J. Y. Howe, J. Sisler, K. Bertens, F. P. García de Arquer, R. K. Miao, C. P. O'Brien, Z. Wang, J. Abed, A. S. Rasouli, M. Sun, A. H. Ip, D. Sinton, E. H. Sargent, *Nat. Energy* **2022**, *7*, 170.
[243] S. X. Ren, D. Joulie, D. Salvatore, K. Torbensen, M. Wang, M. Robert, C. P. Berlinguette, *Science* **2019**, *365*, 367.
[244] C. M. Gabardo, C. P. O'Brien, J. P. Edwards, C. McCallum, Y. Xu, C.-T. Dinh, J. Li, E. H. Sargent, D. Sinton, *Joule* **2019**, *3*, 2777.
[245] Z. Yin, H. Peng, X. Wei, H. Zhou, J. Gong, M. Huai, L. Xiao, G. Wang, J. Lu, L. Zhuang, *Energy Environ. Sci.* **2019**, *12*, 2455.
[246] L.-C. Weng, A. T. Bell, A. Z. Weber, *Energy Environ. Sci.* **2019**, *12*, 1950.
[247] D. Salvatore, C. P. Berlinguette, *ACS Energy Lett.* **2019**, *5*, 215.
[248] L. Ge, H. Rabiee, M. Li, S. Subramanian, Y. Zheng, J. H. Lee, T. Burdyny, H. Wang, *Chem* **2022**, *8*, 663.
[249] B. Endrodi, E. Kecsenovity, A. Samu, F. Darvas, R. V. Jones, V. Torok, A. Danyi, C. Janaky, *ACS Energy Lett.* **2019**, *4*, 1770.
[250] J. Park, Y.-j. Ko, C. Lim, H. Kim, B. K. Min, K.-Y. Lee, J. H. Koh, H.-S. Oh, W. H. Lee, *Chem. Eng. J.* **2023**, *453*.
[251] C. P. O'Brien, R. K. Miao, S. Liu, Y. Xu, G. Lee, A. Robb, J. E. Huang, K. Xie, K. Bertens, C. M. Gabardo, J. P. Edwards, C.-T. Dinh, E. H. Sargent, D. Sinton, *ACS Energy Lett.* **2021**, *6*, 2952.
[252] B. Pan, J. Fan, J. Zhang, Y. Luo, C. Shen, C. Wang, Y. Wang, Y. Li, *ACS Energy Lett.* **2022**, *7*, 4224.
[253] J. Xu, G. Zhong, M. Li, D. Zhao, Y. Sun, X. Hu, J. Sun, X. Li, W. Zhu, M. Li, Z. Zhang, Y. Zhang, L. Zhao, C. Zheng, X. Sun, *Chinese Chem. Lett.* **2022**, *1*, 108075.
[254] X. Tan, C. Yu, Y. Ren, S. Cui, W. Li, J. Qiu, *Energy Environ. Sci.* **2021**, *14*, 765.
[255] L. M. Aeshala, R. G. Uppaluri, A. Verma, *J. CO_2 Util.* **2013**, *3-4*, 49.
[256] J. Zhang, W. Luo, A. Züttel, *J. Catal.* **2020**, *385*, 140.
[257] H. Yang, J. J. Kaczur, S. D. Sajjad, R. I. Masel, *J. CO_2 Util.* **2017**, *20*, 208.
[258] H. Yang, J. J. Kaczur, S. D. Sajjad, R. I. Masel, *ECS Trans.* **2017**, *77*, 1425.

[259] C. Guo, Y. Shen, P. Mao, K. Liao, M. Du, R. Ran, W. Zhou, Z. Shao, *Adv. Funct. Mater.* **2022**, *33*, 2213443.
[260] M. Du, Y. Sun, B. Liu, B. Chen, K. Liao, R. Ran, R. Cai, W. Zhou, Z. Shao, *Adv. Funct. Mater.* **2021**, *31*, 2101556.
[261] C. Xia, P. Zhu, Q. Jiang, Y. Pan, W. Liang, E. Stavitsk, H. N. Alshareef, H. Wang, *Nat. Energy* **2019**, *4*, 776.
[262] L. Fan, C. Xia, P. Zhu, Y. Lu, H. Wang, *Nat. Commun.* **2020**, *11*, 3633.
[263] J. Y. T. Kim, P. Zhu, F.-Y. Chen, Z.-Y. Wu, D. A. Cullen, H. Wang, *Nat. Catal.* **2022**, *5*, 288.
[264] Y. Xu, R. K. Miao, J. P. Edwards, S. Liu, C. P. O'Brien, C. M. Gabardo, M. Fan, J. E. Huang, A. Robb, E. H. Sargent, D. Sinton, *Joule* **2022**, *6*, 1333.
[265] P. Zhu, H. Wang, *Nat. Catal.* **2021**, *4*, 943.
[266] G. Li, Y. Liu, Q. Zhang, Q. Hu, W. Guo, X. Cao, Y. Dou, L. Cheng, Y. Song, J. Su, L. Huang, R. Ye, *J. Mater. Chem. A* **2022**, *10*, 19254.
[267] R. Buonsanti, *Nat. Energy* **2019**, *4*, 728.
[268] Z. S. Zhang, L. Melo, R. P. Jansonius, F. Habibzadeh, E. R. Grant, C. P. Berlinguette, *ACS Energy Lett.* **2020**, *5*, 3101.
[269] A. S. Varela, *Curr. Opin. Green Sust.* **2020**, *26*, 100371.
[270] S. Ma, M. Sadakiyo, R. Luo, M. Heima, M. Yamauchi, P. J. A. Kenis, *J. Power Sources* **2016**, *301*, 219.
[271] J. J. Lv, M. Jouny, W. Luc, W. Zhu, J. J. Zhu, F. Jiao, *Adv. Mater.* **2018**, *30*, e1803111.
[272] W. Sun, P. Wang, Y. Jiang, Z. Jiang, R. Long, Z. Chen, P. Song, T. Sheng, Z. Wu, Y. Xiong, *Adv. Mater.* **2022**, *34*, e2207691.
[273] W. Liu, P. Zhai, A. Li, B. Wei, K. Si, Y. Wei, X. Wang, G. Zhu, Q. Chen, X. Gu, R. Zhang, W. Zhou, Y. Gong, *Nat. Commun.* **2022**, *13*, 1877.
[274] K. J. P. Schouten, E. Pérez Gallent, M. T. M. Koper, *J. Electrochem. Soc.* **2014**, *716*, 53.
[275] J. A. Rabinowitz, M. W. Kanan, *Nat. Commun.* **2020**, *11*, 5231.
[276] M. C. O. Monteiro, M. F. Philips, K. J. P. Schouten, M. T. M. Koper, *Nat. Commun.* **2021**, *12*, 4943.
[277] Y. Qiao, W. Lai, K. Huang, T. Yu, Q. Wang, L. Gao, Z. Yang, Z. Ma, T. Sun, M. Liu, C. Lian, H. Huang, *ACS Catal.* **2022**, *12*, 2357.
[278] J. E. Huang, F. Li, A. Ozden, A. Sedighian Rasouli, F. P. Garcia de Arquer, S. Liu, S. Zhang, M. Luo, X. Wang, Y. Lum, Y. Xu, K. Bertens, R. K. Miao, C. T. Dinh, D. Sinton, E. H. Sargent, *Science* **2021**, *372*, 1074.
[279] D. A. Salvatore, C. M. Gabardo, A. Reyes, C. P. O'Brien, S. Holdcroft, P. Pintauro, B. Bahar, M. Hickner, C. Bae, D. Sinton, E. H. Sargent, C. P. Berlinguette, *Nat. Energy* **2021**, *6*, 339.
[280] A. S. Varela, W. Ju, T. Reier, P. Strasser, *ACS Catal.* **2016**, *6*, 2136.
[281] S. Ringe, E. L. Clark, J. Resasco, A. Walton, B. Seger, A. T. Bell, K. Chan, *Energy Environ. Sci.* **2019**, *12*, 3001.
[282] A. S. Malkani, J. Anibal, B. Xu, *ACS Catal.* **2020**, *10*, 14871.
[283] M. C. O. Monteiro, A. Goyal, P. Moerland, M. T. M. Koper, *ACS Catal.* **2021**, *11*, 14328.
[284] M. C. O. Monteiro, F. Dattila, N. Lopez, M. T. M. Koper, *J. Am. Chem. Soc.* **2022**, *144*, 1589.
[285] S. Banerjee, Z.-Q. Zhang, A. S. Hall, V. S. Thoi, *ACS Catal.* **2020**, *10*, 9907.
[286] L. D. Chen, M. Urushihara, K. Chan, J. K. Nørskov, *ACS Catal.* **2016**, *6*, 7133.
[287] J. Resasco, L. D. Chen, E. Clark, C. Tsai, C. Hahn, T. F. Jaramillo, K. Chan, A. T. Bell, *J. Am. Chem. Soc.* **2017**, *139*, 11277.
[288] S. Verma, X. Lu, S. Ma, R. I. Masel, P. J. Kenis, *Phys. Chem. Chem. Phys.* **2016**, *18*, 7075.
[289] S. T. Ahn, I. Abu-Baker, G. T. R. Palmore, *Catal. Today* **2017**, *288*, 24.

[290] H. Hashiba, S. Yotsuhashi, M. Deguchi, Y. Yamada, *ACS Comb Sci* **2016**, *18*, 203.
[291] A. Löwe, C. Rieg, T. Hierlemann, N. Salas, D. Kopljar, N. Wagner, E. Klemm, *ChemElectroChem* **2019**, *6*, 4497.
[292] A. Kudo, S. Nakagawa, A. Tsuneto, T. Sakata, *J. Electrochem. Soc.* **2019**, *140*, 1541.
[293] S. Kaneco, K. Iiba, H. Katsumata, T. Suzuki, K. Ohta, *Electrochim. Acta* **2006**, *51*, 4880.
[294] K. Hara, A. Kudo, T. Sakata, *J. Electrochem. Soc.* **1995**, *391*, 141.
[295] K. Hara, A. Tsuneto, A. Kudo, T. Sakata, *J. Electrochem. Soc.* **2019**, *141*, 2097.
[296] E. J. Dufek, T. E. Lister, S. G. Stone, M. E. McIlwain, *J. Electrochem. Soc.* **2012**, *159*, F514.
[297] J. P. Edwards, Y. Xu, C. M. Gabardo, C.-T. Dinh, J. Li, Z. Qi, A. Ozden, E. H. Sargent, D. Sinton, *Appl. Energ.* **2020**, *261*, 114305.
[298] R. Krause, D. Reinisch, C. Reller, H. Eckert, D. Hartmann, D. Taroata, K. Wiesner-Fleischer, A. Bulan, A. Lueken, G. Schmid, *Chem. Ing. Tech.* **2020**, *92*, 53.
[299] C. M. Gabardo, A. Seifitokaldani, J. P. Edwards, C.-T. Dinh, T. Burdyny, M. G. Kibria, C. P. O'Brien, E. H. Sargent, D. Sinton, *Energy Environ. Sci.* **2018**, *11*, 2531.
[300] M. Sassenburg, M. Kelly, S. Subramanian, W. A. Smith, T. Burdyny, *ACS Energy Lett.* **2023**, *8*, 321.

Figures

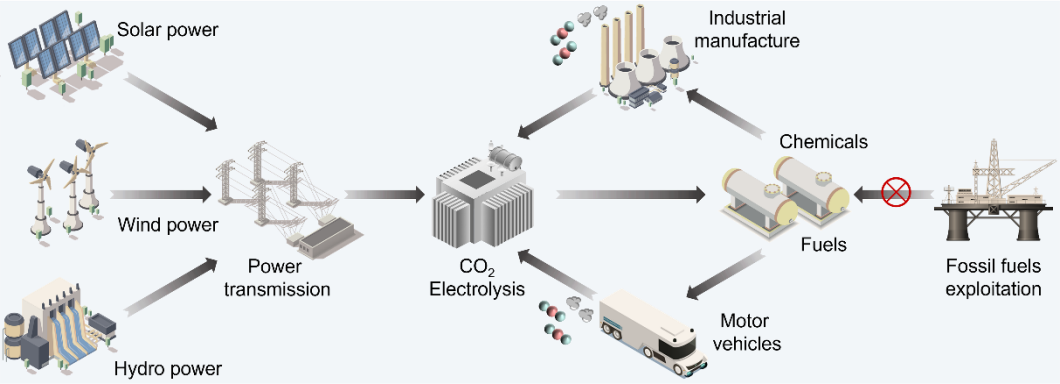

Scheme 1. CO_2RR technology and the sustainable carbon energy cycle.

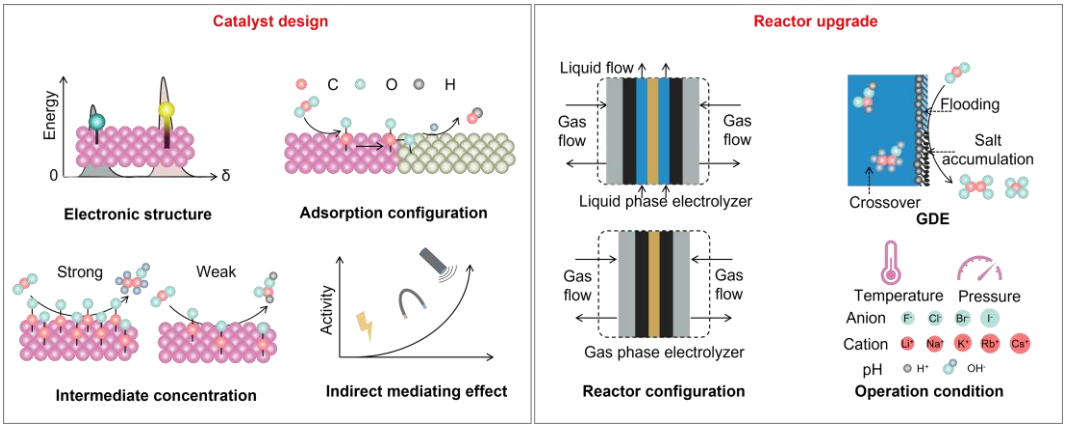

Scheme 2. Schematic overview of catalyst design and reactor upgrade.

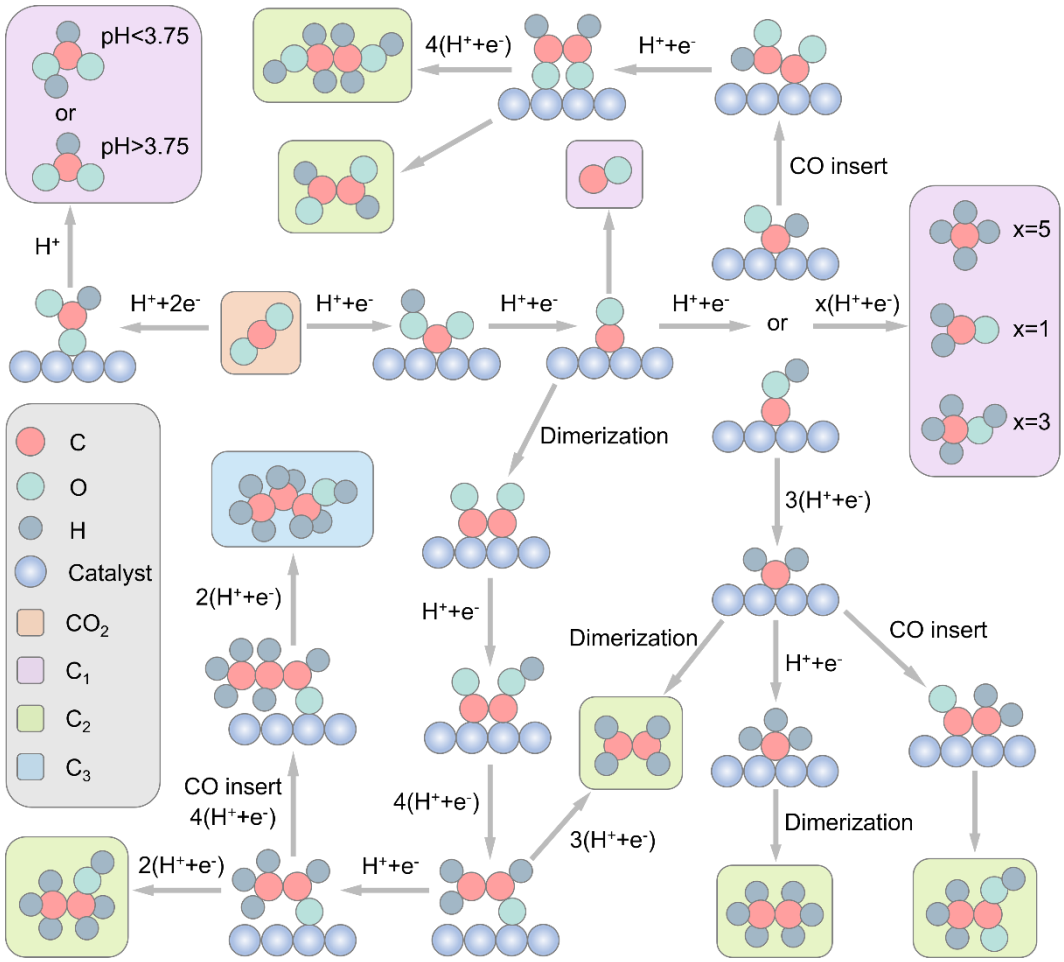

Scheme 3. Possible reaction pathways of CO_2RR to different products.

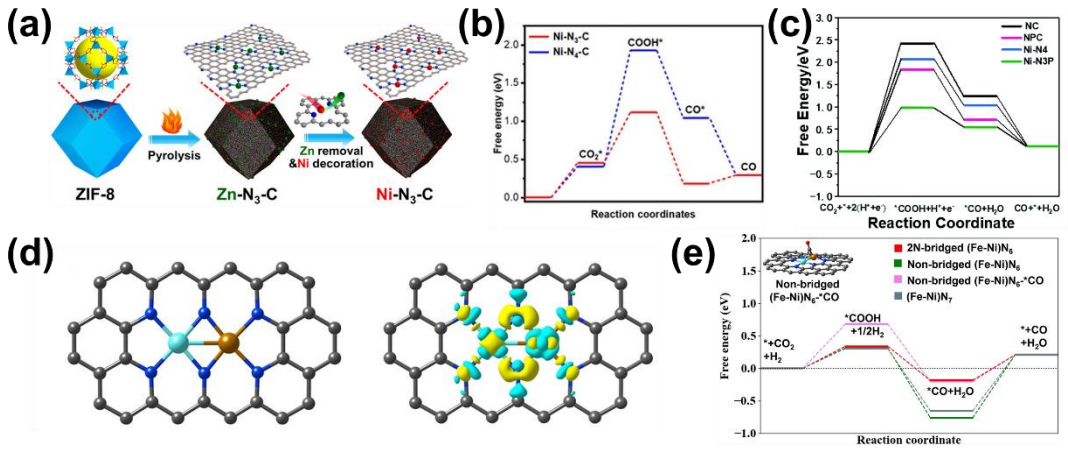

Figure 1. (a) Synthetic process of low-coordination Ni SACs and (b) schematic Gibbs free energy profile for the CO_2RR to CO. Reproduced with permission.[106] Copyright 2021, Wiley-VCH. (c) Gibbs free energy of the intermediates on Ni-N_3P. Reproduced with permission.[107] Copyright 2022, Royal Society of Chemistry (RSC). (d) Atomic structure and electronic structure of NiFe-N_6 DACS and (e) free energy diagrams of various DACS Ni-Fe sites for the CO_2RR to CO. Reproduced with permission.[110] Copyright 2021, Wiley-VCH.

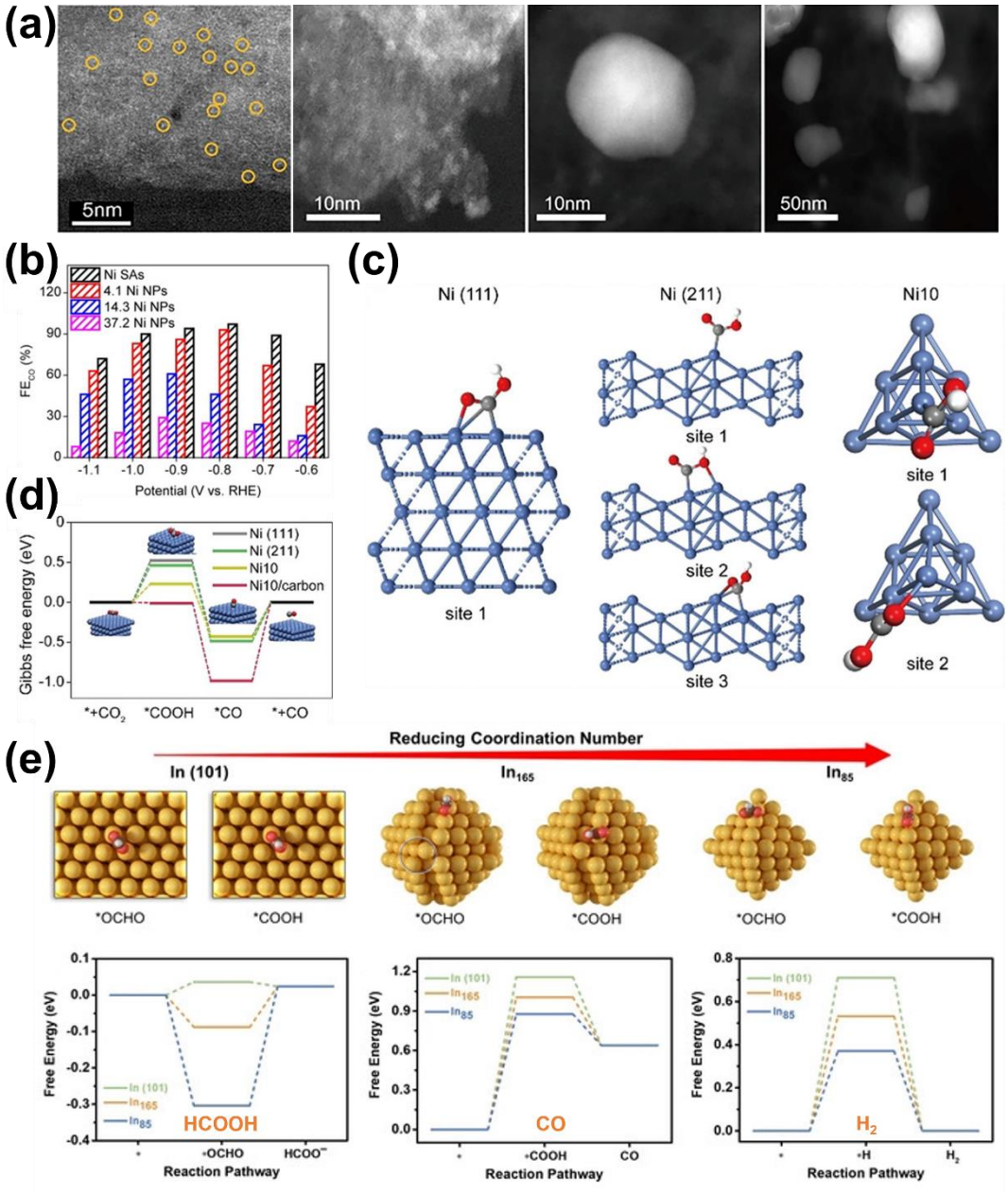

Figure 2. (a) Scanning transmission electron microscopy of Ni SAC, 4.1 nm Ni NPs, 14.3 nm Ni NPs and 37.2 nm Ni NPs and (b) applied potential-dependent CO FE. (c) Calculation adsorption models of *COOH on different-sized Ni NPs (Ni(111) simulated as 37.2 nm Ni NPs, Ni(211) simulated as 14.3 nm Ni NPs, Ni10 clusters simulated as 4.1 nm Ni NPs) and (d) corresponding Gibbs free energy profile of CO2RR to CO. Reproduced with permission.[114] Copyright 2020, Wiley-VCH. (e) Optimized model structures of In clusters with reduced particle size and corresponding free energy diagrams toward HCOOH, CO, and H_2. Reproduced with permission.[115] Copyright 2021, Wiley-VCH.

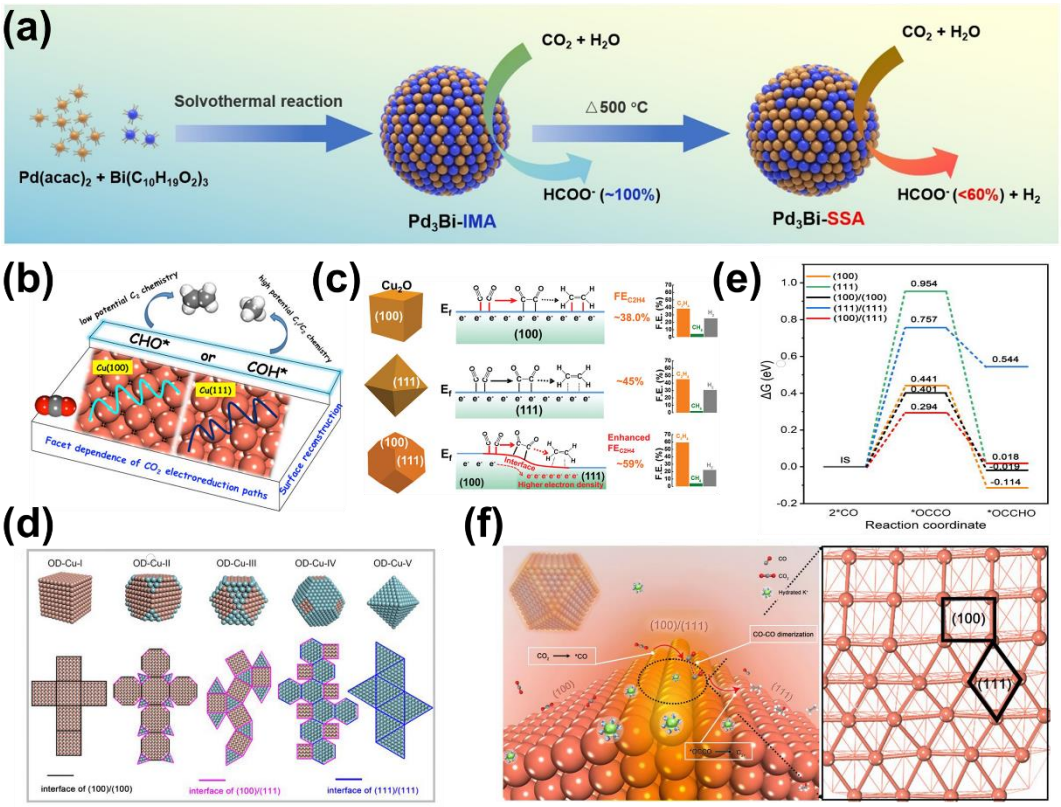

Figure 3. (a) Synthetic procedure and phase transformation of Pd_3Bi. Reproduced with permission.[121] Copyright 2021, Wiley-VCH. (b) Facet-dependent CO2RR pathways of Cu catalyst. Reproduced with permission.[125] Copyright 2016, American Chemical Society (ACS). (c) Facet dependence of C_2H_4 formation on Cu electrodes. Reproduced with permission.[127] Copyright 2020, Wiley-VCH. (d) Structural details and (e) reaction energetics of *CO dimerization of the as-prepared OD-Cu catalysts; (e) catalytic mechanism to form C_{2+} products at the Cu(100)/(111) interface. Reproduced with permission.[128] Copyright 2022, ACS.

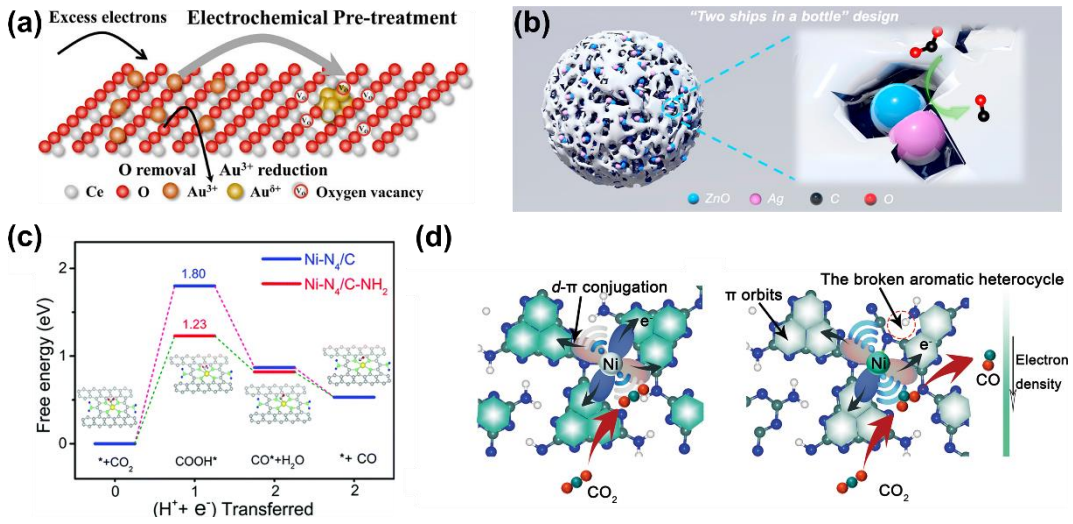

Figure 4. (a) Activation by electrochemical pretreatment at the Au-CeO_2 interface. Reproduced with permission.[131] Copyright 2021, ACS. (b) Illustrative structure of the confined ZnO-Ag catalyst. Reproduced with permission.[132] Copyright 2021, ACS. (c) Free energy diagram of the CO_2RR to CO over Ni-N_4-C-NH_2. Reproduced with permission.[136] Copyright 2021, RSC. (d) The effect of d-π conjugation on CO_2 activation over Ni SAC and cyano organic species decorated Ni SAC. Reproduced with permission.[137] Copyright 2022, Springer Nature.

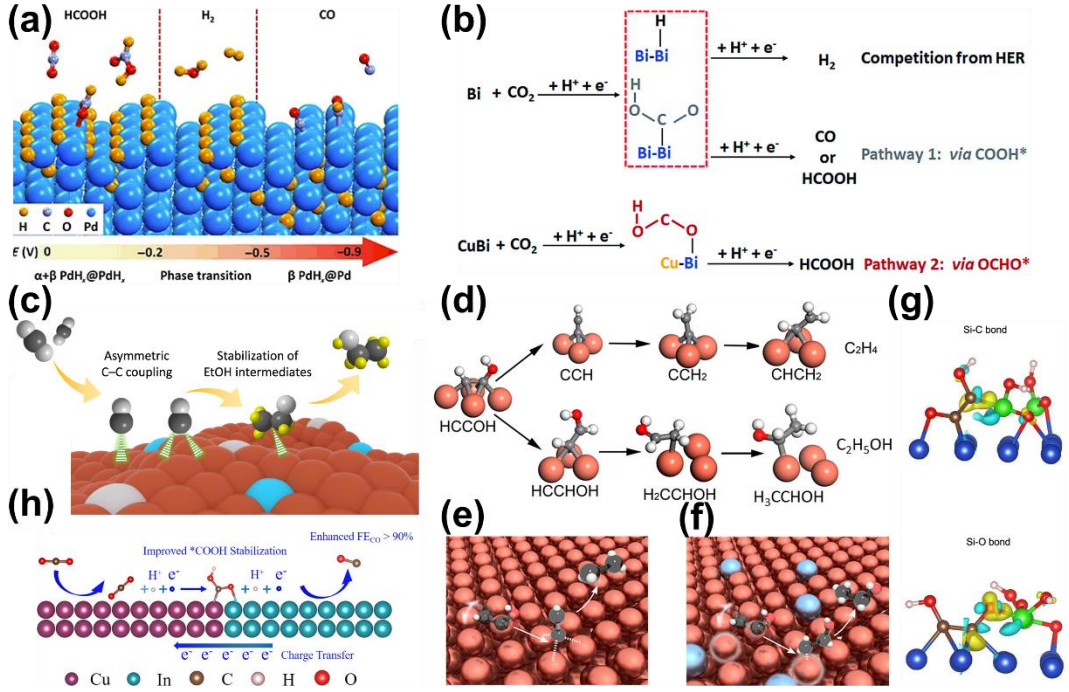

Figure 5. (a) Applied potential-determined active phase transition and product selectivity of Pd NPs. Reproduced with permission.[150] Copyright 2017, Springer Nature. (b) Reduction pathways for HCOOH production on Bi catalysts with and without Cu doping. Reproduced with permission.[151] Copyright 2018, RSC. (c) Schematic for boosted EtOH generation via asymmetric C-C dimerization. Reproduced with permission.[154] Copyright 2022, Springer Nature. (d) Reaction pathways of CO_2 to C_2H_4 and C_2H_5OH on Cu (111) and the binding sites of C_2H_4 and C_2H_5OH key intermediates on (e) Cu and (f) CuAg alloy. Reproduced with permission.[159] Copyright 2019, ACS. (g) Schematic of *OCOH and *OCCOH stabilized via strong Si–O or Si–C bonds. Reproduced with permission.[163] Copyright 2021, Springer Nature. (h) Schematic of $In(OH)_3$-coupled Cu_2O-derived hybrid catalysts with a Cu-In interface for enhanced CO_2 reduction. Reproduced with permission.[164] Copyright 2019, ACS.

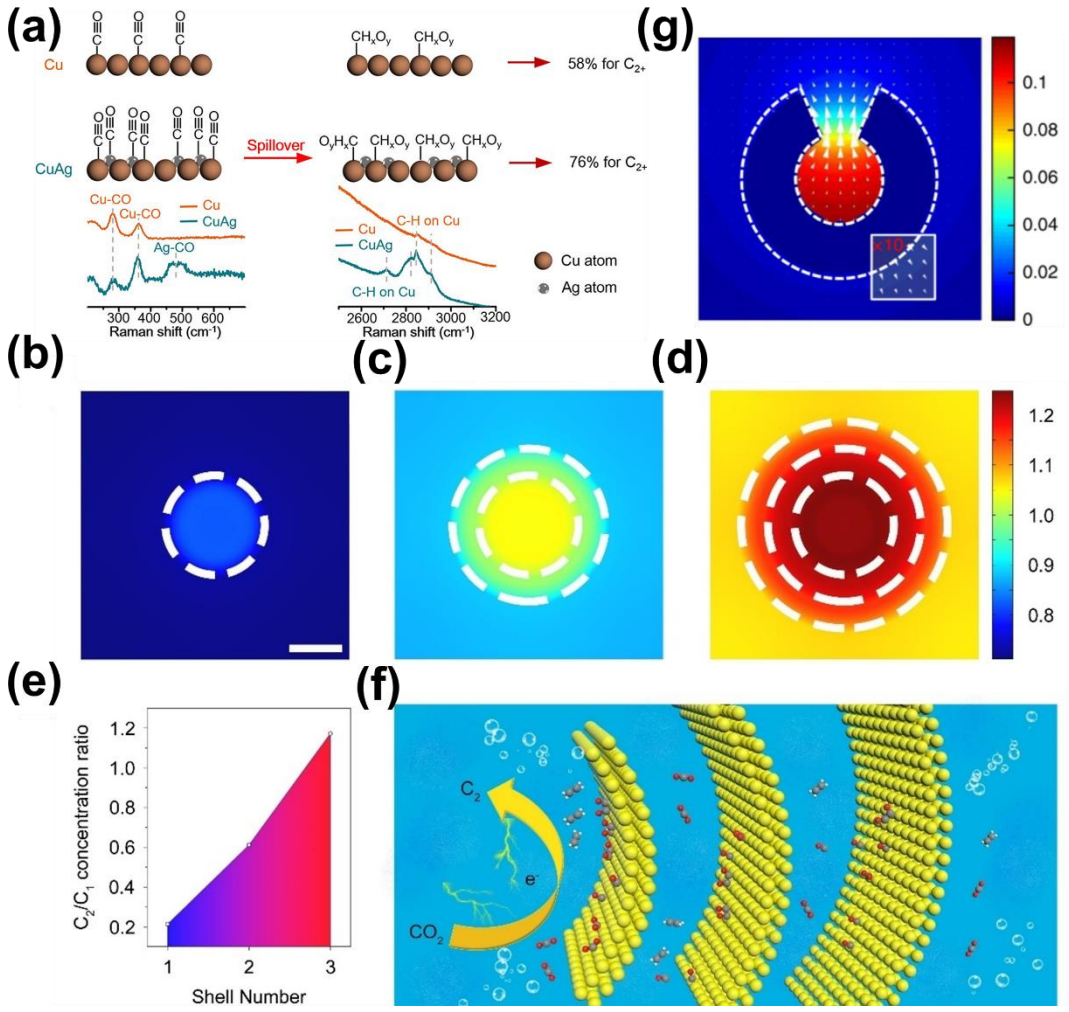

Figure 6. (a) Illustration of *CO spillover for the enhanced C-C couple reaction. Reproduced with permission.[180] Copyright 2019, ACS. (b-e) The finite element simulation simulated species C_2/C_1 concentration ratio distribution within 1-shell Cu nanospheres, 3-shell Cu nanospheres, and 3-shell Cu nanospheres and (f) schematic of the confinement effect boosting C_2 production. Reproduced with permission.[182] Copyright 2022, Wiley-VCH. (g) C_3 product concentration and flux distribution diagram obtained by simulation calculation. Reproduced with permission.[183] Copyright 2018, Springer Nature.

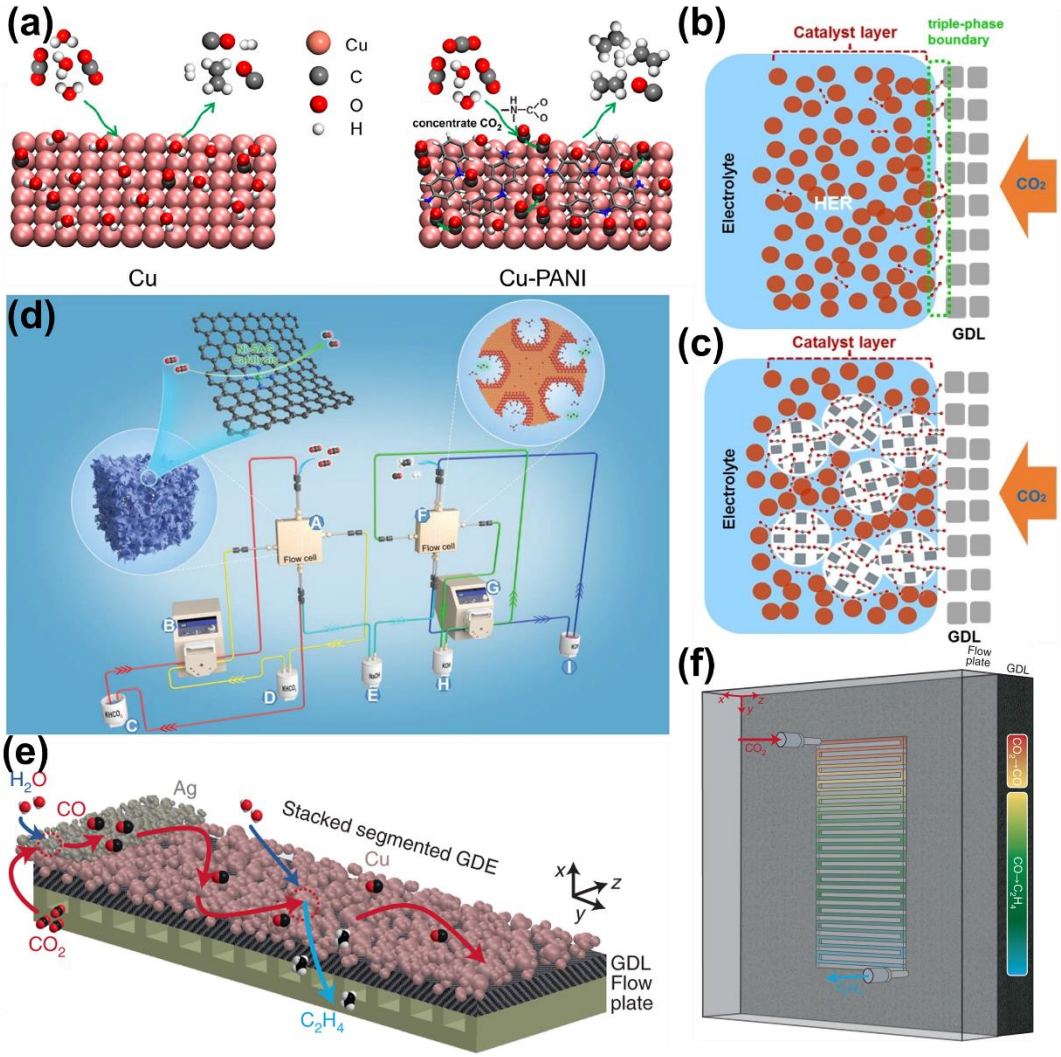

Figure 7. (a) Illustration of the CO_2RR on pure Cu and Cu/PANI. Reproduced with permission.[188] Copyright 2020, ACS. The reaction species distribution in the catalytic interface (b) without and (c) with POCs decorated. Reproduced with permission.[189] Copyright 2022, Wiley-VCH. (d) Schematic illustration of the tandem CO2RR catalytic system. Reproduced with permission.[192] Copyright 2022, Wiley-VCH. (e) Schematic of stacked segmented GDE and (f) flow channel geometry. Reproduced with permission.[193] Copyright 2022, Springer Nature.

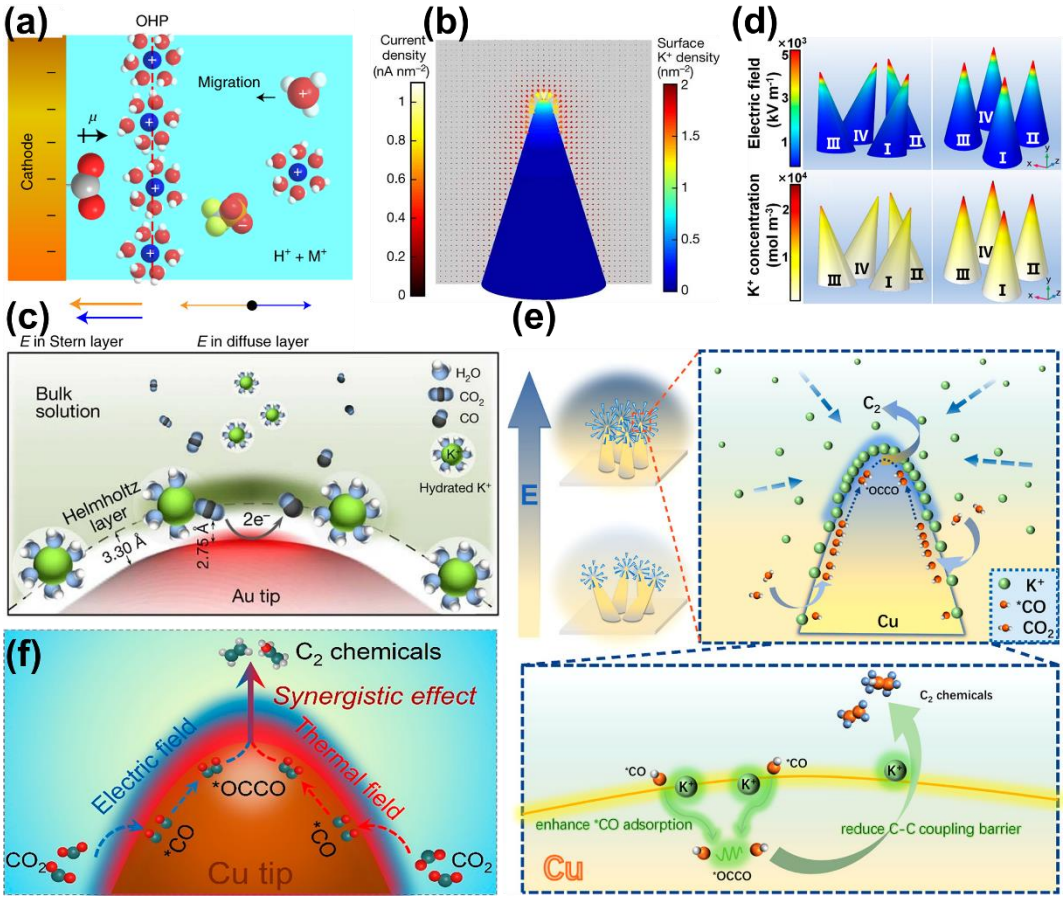

Figure 8. (a) Schematic diagram of cation effects on the interface electric field distribution in acidic media. Reproduced with permission.[199] Copyright 2022, Springer Nature. (b) Computed current density distribution with surface K^+ density and (c) CO_2 to CO conversion on Au nanoneedles. Reproduced with permission.[201] Copyright 2016, Springer Nature. (d) Local electric field with K^+ concentration on the ordered arrangement of Cu nanoneedles; (e) C_2 formation mechanism on an ordered Cu single tip. Reproduced with permission.[202] Copyright 2022, ACS. (f) Illustration of the electric-thermal synergy field on a single Cu tip. Reproduced with permission.[203] Copyright 2021, ACS.

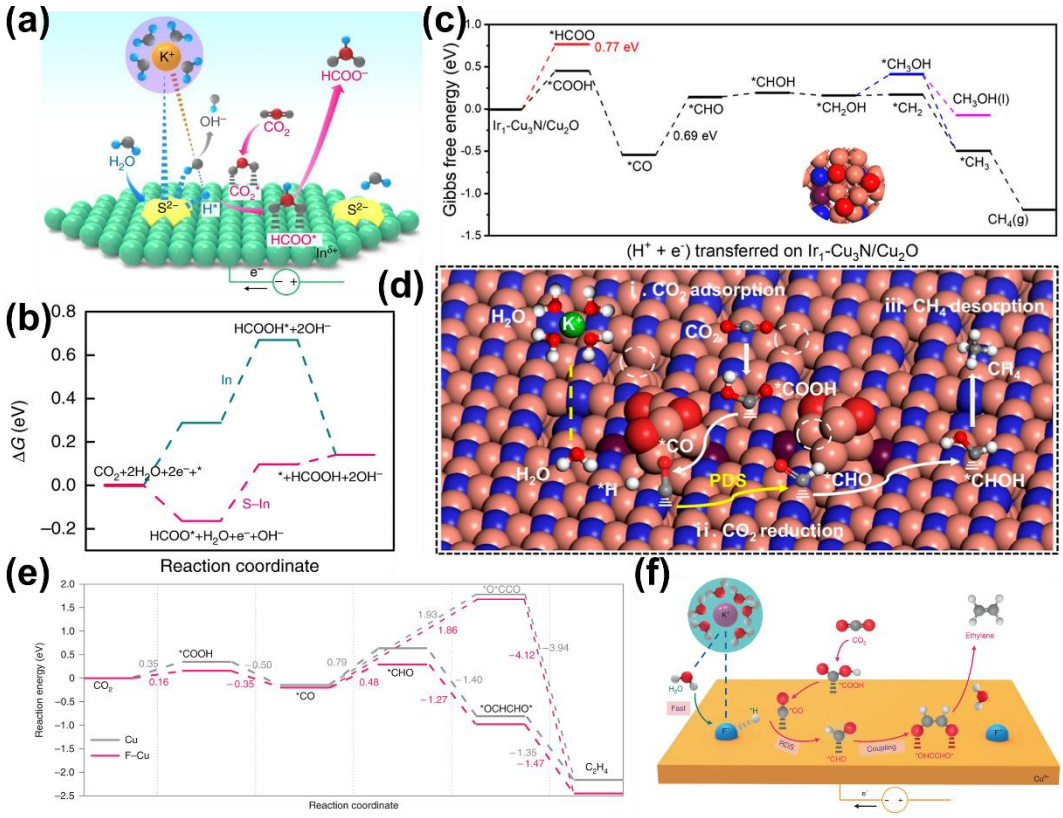

Figure 9. (a) Mechanism illustration of the promoting effect on the CO_2RR caused by sulfur and (b) free energy diagram of the CO_2RR to HCOOH on sulfur-doped indium catalysts. Reproduced with permission.[209] Copyright 2019, Springer Nature. (c) Schematic Gibbs free energy profile for the CO_2RR to CH4 on Ir-Cu_3N/Cu_2O and (d) corresponding reactive mechanism. Reproduced with permission.[210] Copyright 2022, ACS. (e) Reaction energy diagram of CO_2RR to C_2H_4 via the *CO dimerization pathway or *CHO dimerization pathway and (f) proposed reaction mechanism. Reproduced with permission.[57] Copyright 2020, Springer Nature.

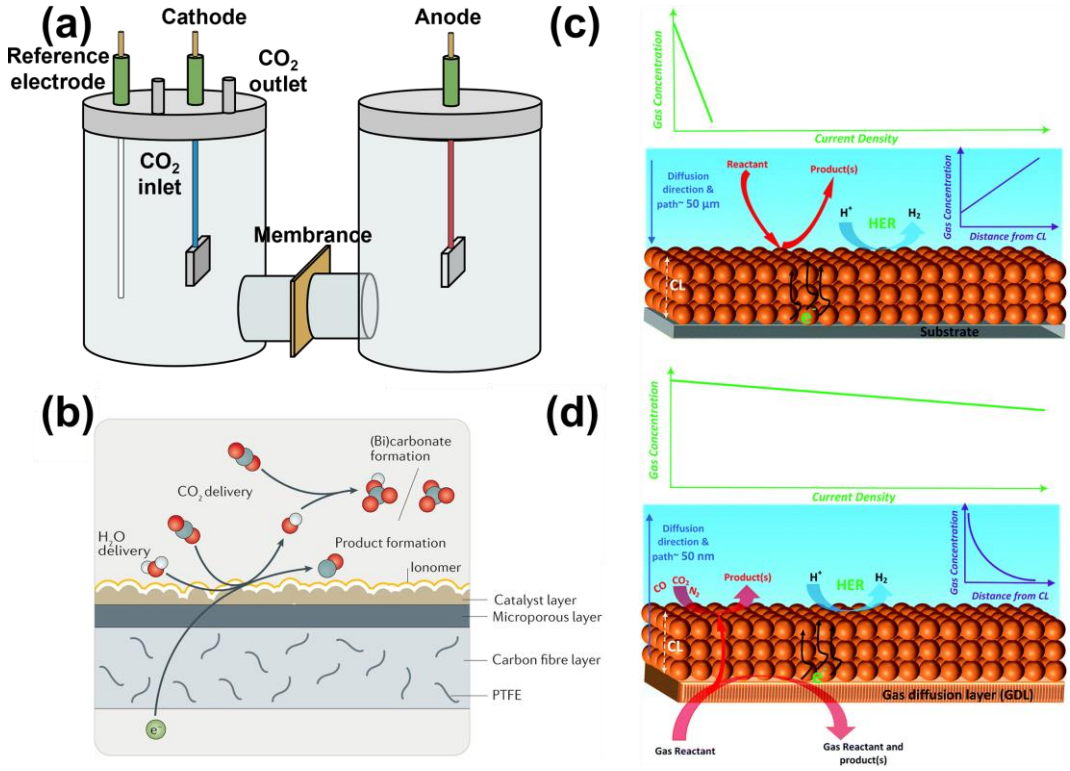

Figure 10. (a) A conventional H-type CO_2RR electrolyzer configuration. (b) Schematic of the GDE and gas–solid-liquid three-phase interface. Reproduced with permission.[37] Copyright 2021, Springer Nature. CO_2 mass transfer distance in the (c) H-type cell and (d) flow-type cell. Reproduced with permission[39]. Copyright 2021, RSC.

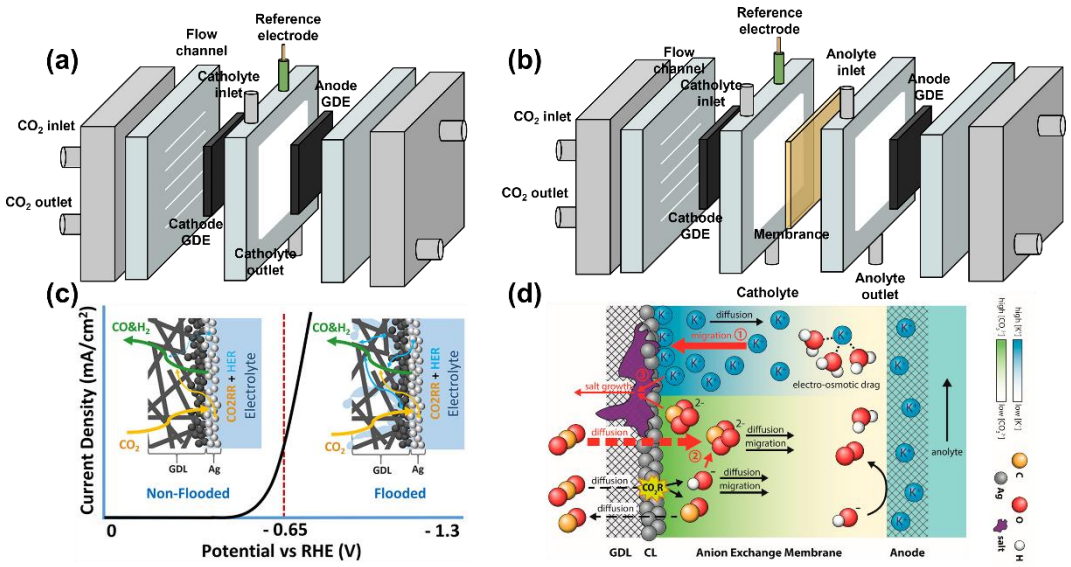

Figure 11. (a) Schematic diagram of the microfluidic electrolyzer. (b) Schematic diagram of the liquid phase electrolyzer. (c) Schematic diagram of GDE flooding. Reproduced with permission.[231] Copyright 2020, ACS. (d) Schematic diagram of (bi)carbonation and salt deposition. Reproduced with permission.[300] Copyright 2022, ACS.

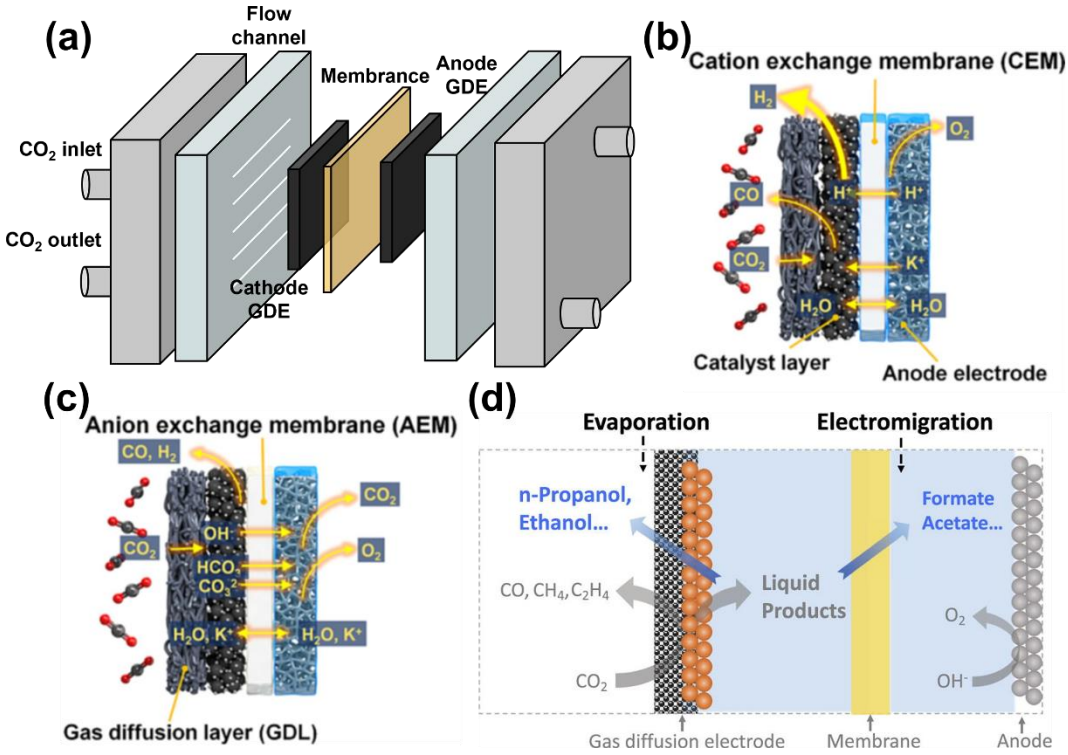

Figure 12. (a) Schematic diagram of the gas phase electrolyzer. (b) Illustrations of mass transfer in the gas phase CEM electrolyzer and (c) gas phase AEM electrolyzer. Reproduced with permission.[250] Copyright 2023, Elsevier. (d) Schematic diagram of liquid product crossover via AEM. Reproduced with permission.[256] Copyright 2020, Elsevier.

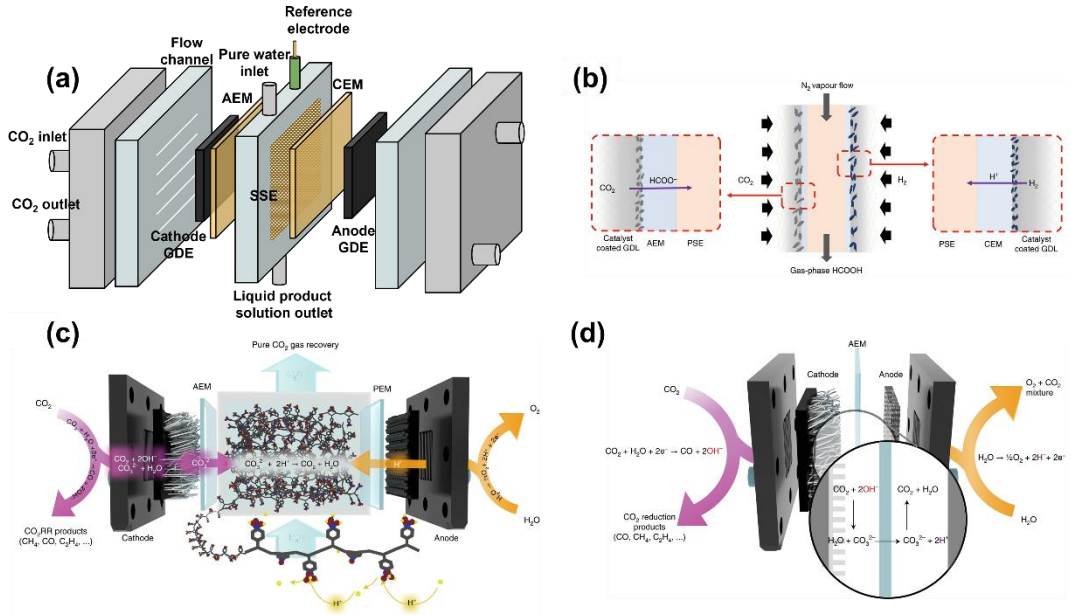

Figure 13. (a) Schematic diagram of the solid state electrolyzer. (b) Schematic illustration of the solid state electrolyzer for collecting high-purity liquid products with inert gas. Reproduced with permission.[262] Copyright 2020, Springer Nature. (c) Solid state electrolyzer for recovering carbon losses and (d) CO_2 crossover phenomenon in a gas phase AEM electrolyzer. Reproduced with permission.[263] Copyright 2022, Springer Nature.

TOC

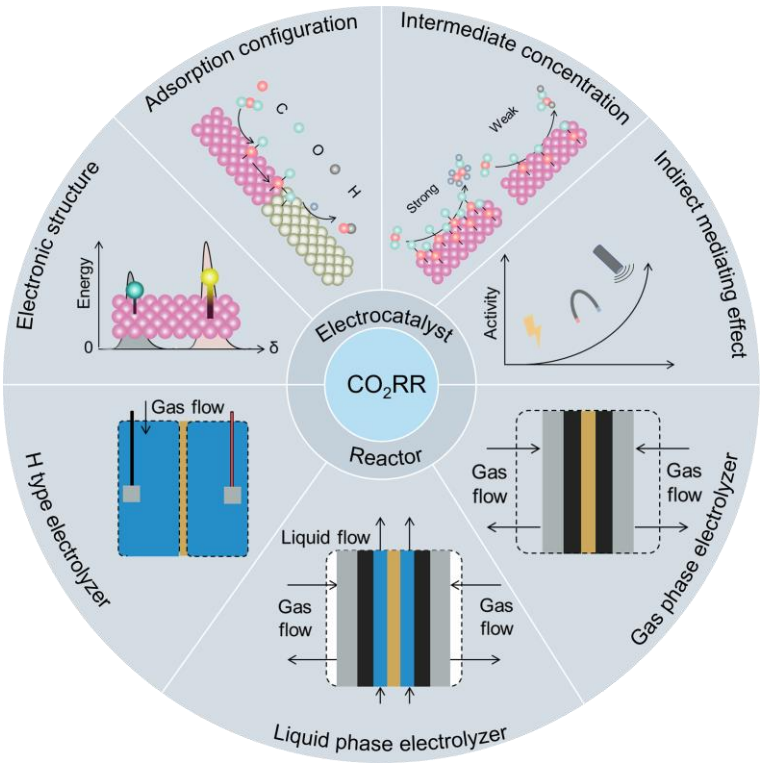
Adsorption configuration
C
O
H
Intermediate concentration
Weak
Strong
Electronic structure
Energy
0
δ
Indirect mediating effect
Activity
Electrocatalyst
CO_2RR
Reactor
H type electrolyzer
Gas flow
Gas phase electrolyzer
Gas flow
Gas flow
Liquid phase electrolyzer
Liquid flow
Gas flow
Gas flow

Biography

Dr. Devis Di Tommaso is currently a senior lecturer in Computational Chemistry at Queen Mary University of London. He obtained his doctoral degree in Chemistry from the University of Trieste in 2016. Devis joined University College London (UCL) as part of a Marie-Curie research and training network in 2007. He was was awarded a Royal Society Industry Fellowship between UCL and AstraZeneca in 2012. He leads a research group focusing on theoretical catalysis, CO2 conversion, and aqueous thermodynamic modeling.

Dr. Yuanjie Pang received his B. Eng degree and Ph.D. degree at the Department of Electrical and Computer Engineering at University of Victoria in 2008 and 2012. He joined the School of Pharmacy, University of Michigan, to perform his first postdoctoral research in 2012. Afterwards, he joined Profs. David Sinton (Department of Mechanical and Industrial Engineering) and Edward H. Sargent's (Department of Electrical and Computer Engineering) research groups and the University of Toronto as a coappointed Postdoctoral Fellow. Pang has become a Professor at Huazhong University of Science and Technology since 2018, where he leads a research group in electrocatalysis and nanophotonics.

Dr. Shujiang Ding is currently a full professor in the School of Chemistry at Xi'an Jiaotong University. He received his Bachelor Degree (2001) and Master Degree (2004) in Polymer Science and Engineering from Xi′an Jiaotong University, and Ph.D. in Polymer Physics and Chemistry (2007) from ICCAS. Prior to joining Xi′an Jiaotong University in 2011, Dr. Ding worked as a Postdoctoral Fellow in ICCAS (2007-2009), UCF (2009-2010) and NTU (2010-2011). His researches focus on multidimensional nanostructured materials for renewable energy conversion and storage, sensors, actuators, and electrocatalysis.

Dr. Bao Yu Xia is currently a full professor in the School of Chemistry and Chemical Engineering at Huazhong University of Science and Technology. He received his Ph.D. degree in Materials Science and Engineering from Shanghai Jiao Tong University in 2010. He worked at Nanyang Technological University from 2011 to 2016. His research interests focus on functional nanomaterials in sustainable energy and environmental technologies, including fuel cells, batteries and carbon dioxide conversion.